Title
Vector AC Stark shift in ^{133}Cs atomic magnetometers with antirelaraxion coated cells

Author
Zhivun, Elena

Publication Date
2016

Peer reviewed|Thesis/dissertation

Vector AC Stark shift in ^{133}Cs atomic magnetometers with antirelaraxion coated cells

by

Elena Zhivun

A dissertation submitted in partial satisfaction of the

requirements for the degree of

Doctor of Philosophy

in

Physics

in the

Graduate Division

of the

University of California, Berkeley

Committee in charge:

Professor Dmitry Budker, Chair
Professor Jonathan Wurtele
Professor Masayoshi Tomizuka

Spring 2016

Vector AC Stark shift in ^{133}Cs atomic magnetometers with antirelaraxion coated cells

Abstract

Vector AC Stark shift in ^{133}Cs atomic magnetometers with antirelaraxion coated cells

by

Elena Zhivun

Doctor of Philosophy in Physics

University of California, Berkeley

Professor Dmitry Budker, Chair

The main focus of this dissertation is investigation of vector AC Stark shifts (light shifts) in evacuated ^{133}Cs paraffin-coated cells. Although light shifts in alkali atoms have been investigated since 1960s, the effect of laser-induced vector light shifts (VLS) in paraffin-coated cells is little explored in literature. The works considering light shift effects primarily focus on transitions relevant for atomic clocks, or magnetometers using buffer gas cells, or magnetometers using broad-spectrum alkali metal lamps. This work, on the other hand, focuses on light shifts in a setup shared by finite-field optical magnetometers that use paraffin-coated sensor cells, as well as on their impact on sensitivity and accuracy of these devices.

Along with describing the light shifts, this work presents several techniques that take advantage of the VLS to improve atomic magnetometers as a tool. The proposed techniques eliminate the need for oscillating radio-frequency magnetic fields and replace them with well contained laser beams. This can benefit applications where non-magnetic sensors are needed and stray fields are highly undesirable, such as the search for a permanent electric dipole moment of the neutron.

This dissertation includes two such projects, the all-optical vector magnetometer and the rf magnetometer driven by a fictitious magnetic field. In the first project a finite-field optical magnetometer, which is normally a scalar sensor, is augmented with two power-modulated orthogonal laser beams that provide the directional sensitivity. The sensor exhibits a demonstrated rms noise floor of $50\,\mathrm{fT}/\sqrt{\mathrm{Hz}}$ in measurement of the field magnitude and 0.5 mrad/$\sqrt{\mathrm{Hz}}$ in the field direction. Elimination of technical noise would improve these sensitivities to $12\,\mathrm{fT}/\sqrt{\mathrm{Hz}}$ and 5 μrad/$\sqrt{\mathrm{Hz}}$, respectively. In the second project, the atomic precession in a scalar ^{133}Cs magnetometer is driven by an effective oscillating magnetic field provided by the AC Stark shift of an intensity-modulated laser beam. The demonstrated sensitivity of this magnetometer is $40\,\mathrm{fT}/\sqrt{\mathrm{Hz}}$ rms, which is equivalent to the conventional coil-driven scalar magnetometer we built sharing the same setup.

The Appendix includes documentation on the custom-built polarimeter used in the experiments and the frequency response of the magnetic sensor head.

To my mom and dad.

Contents

List of Figures

List of Tables

Acknowledgments

First and foremost, I would like to thank my research adviser Dima Budker. In Fall 2011 he let me join his group and gave me a great opportunity to learn and meet new people. Dima has a great passion for physics both inside and outside his area of research. With his never-ending enthusiasm, Dima can make any project look interesting and inspiring. Thanks to Dima constantly inviting visitors, I had an opportunity to meet people from all over the world, including my soul mate Chris. Working in Dima's lab I have learned what it means to be a scientist. I owe my deepest gratitude to Dima for his support and guidance through my graduate school career.

Dima's group has been a welcoming place with nice colleagues and visitors from all over the world. I would like to express my deep gratitude to my fellow labmates – Brian Patton, Arne Wickenbrock, David Wurm, Szymon Pustelny, Dimitri Dounas-Frazer, Damon English, Chris Hovde, Micah Ledbetter, Rui Zou, Maria Simanovskaia, Andrey Jarmola, Lykourgos Bougas, Derek Kimball, Andrew Park and many others. They made me feel welcome during my stay in Dima's group and helped me out, be it lending equipment and optics, or giving a helpful advice.

I would especially like to thank Arne Wickenbrock who has been a great colleague who I had pleasure to collaborate with on several papers. Arne helped me to accomplish the projects that seemed hopeless before he came over. During the time we worked together, Arne has become not just a valued colleague, but also a good friend.

Another person I absolutely enjoyed working with is David Wurm. David has become an awesome friend and we spend plenty of time together both in the lab and outside it. It is always been a pleasure and a great deal of fun to work with, in physics or otherwise. Having David around boosted my morale a lot.

It has been a privilege to work with Brian Patton, whom I owe most of what I know about experimental methods and research in general. Brian was very patient and always managed to find time for me despite of how many things he had to take care of in the lab, which I am immensely grateful for. This thesis would not be possible without Brian's mentorship and experience I gained from working with him. Brian always stayed very motivated and energetic, and he helped me to stay motivated as well when research did not go so well. He showed me a great example of how high quality research is done. Brian is the single most impressive and unforgettable person I met, and am truly glad I had an opportunity to work with him. He taught me many valuable lessons outside of science as well, and working with him helped me grow as a person.

I would also like to thank my former colleagues and mentors whom I had pleasure to work with back when I was an undergraduate researcher – Vladimir Velichansky, Vitaliy Vassiliev, Alexander Kozlov, Sergey Zibrov, Valeriy Yakovlev, Dmitry Turikov and Gleb Romanov. They introduced me into the field of atomic magnetometry, and taught me many experimental physics techniques. Their help, mentorship and the experience they helped me to gain prepared me well for my future career. I would also like to express my gratitude to

Evgeniy Babadjan, who is one of the best and most memorable physics teachers I had. I owe all these people my groundwork and the ability to become a graduate student in Berkeley.

I would like to express my deepest gratitude to the Physics Department staff and faculty. I want to thank Anne Takizawa and Donna Sakima for helping me out with the administrative side of being a graduate student, and Anthony Vitan for his support in logistics and maintenance. I also want to say thank you to Joseph Kant, who taught me how to work in the machine shop. I used plenty of custom parts to build my experiments, which I would not be able to machine without his helpful advice. I want to show my gratefulness to professor Holger Müller for his invaluable help in electronics, as well as his support and advising. I would like to thank professors Jonathan Wurtele and Masayoshi Tomizuka who agreed to be on my dissertation committee and professor Naomi Ginsberg for joining my qualification exams committee.

Finally, I want to thank my parents who helped me to develop curiosity and interest in physics and supported me all these years, as well as my friends, who helped me to keep in touch with the world outside of the lab. For that, I owe them a debt of gratitude. I am also grateful to Chris for being kind, supportive, understanding and patient with me, and cheering me up throughout all these years of graduate school. It would be much harder to endure without his support.

With regard to the materials presented in Section 3.2, we thank Douglas Beck, Michael Sturm, David Wurm, and Peter Fierlinger for their helpful input, as well as Mikhail Balabas for preparation of the antirelaxation-coated cesium cell. We also thank Arne Wickenbrock for contributions to the measurement. This work was funded in part by a University of California UC Discovery Proof of Concept grant (award 197073) and NASA SBIR contract NNX13CG20P, and is supported by National Science Foundation Grant No. PHY-1068875. B. Patton is supported by DFG Priority Program SPP1491, “Precision measurements with cold and ultracold neutrons”.

I really appreciate the great help of Dima and Jonathan in proofreading this thesis.

Chapter 1

Introduction

1.1 Atomic magnetometers and applications

Since the introduction of the optical detection and pumping in 1950s [1–3], atomic magnetometers have been widely used for a large variety of applications. At the present, atomic magnetometers hold the record as the world's most sensitive magnetic-field measuring devices, reaching the sensitivity of $0.16\,\mathrm{fT}/\sqrt{\mathrm{Hz}}$ [4] (0.003 parts per billion of Earth's magnetic field). Atomic magnetometers have high precision as well, since the measured frequency is directly related to the magnetic field by physical constants [1,5]. In contrast with other ultra sensitive detectors, such as SQUID [6], which must be cooled by liquid helium or nitrogen to operate, atomic magnetometers can function at room temperature. They can work in both a shielded environment and in Earth's magnetic field; these two factors make them versatile devices that are inexpensive to operate and maintain. Atomic magnetometers find a wide range of uses, varying from fundamental physics research to geological, medical and military applications.

In fundamental physics, atomic magnetometers are employed in search for new spin-dependent fundamental interactions, such as spin-gravity coupling [7], anisotropic spin coupling [8], or detecting axion-like domain walls [9]. Another fundamental research application is the search for permanent electric dipole moment (EDM) [10]. A common technique is to compare the precession frequency of a neutral system in the magnetic field parallel and anti-parallel with the electric field [11,12]. The difference between the two frequencies yields a direct measurement of EDM. These measurements have been proposed and carried out for neutrons [13] and molecules [14–16]. One important source of systematic error are the changes in the magnetic field correlated with the electric field, as they mimic the effect of the EDM. For this reason EDM experiments require careful monitoring of the magnetic field with high precision. Part of the work in this dissertation is devoted to building an all-optical vector magnetometer [17] that does not disturb the magnetic environment around it. This experience will be used to build an array of non-magnetic sensors for the TU München neutron EDM (nEDM) experiment [10] and reconstruct the magnetic field within the neutron chamber of the apparatus.

Measuring electric activity produced by electric currents in human body is a basis of medical diagnosis methods such as electrocardiography (ECG). Similarly, measuring magnetic fields induced by these currents provides complementary diagnosis methods such as magnetocardiaoraphy (MCG) [18, 19]. Magnetic signals have an advantage compared to the electric signals that they are not distorted by conductive tissues of human body. In addition, measuring electric fetal heart activity poses a challenge, which is believed to be due to the low conductivity of *vernix caseosa*, the substance covering a fetus [20]. Detecting biomagnetic fields is challenging, as the signal is at least six orders of magnitude smaller than the background magnetic Earth's field. For this reason, medical magnetometry applications typically employ SQUID sensors operating inside expensive magnetically shielded rooms [21–23] (the experiments with SQUIDs outside the magnetic shielding have been carried out as well [24]). With the advance of atomic magnetometers, they have become a feasible alternative to SQUIDs. Atomic magnetometers have several advantages over SQUIDs, as they do not need to be cooled down to cryogenic temperatures and do not require expensive liquid helium to operate. Successful measurements of heart [18, 25], brain [26, 27] and fetal heart activity [28] have been demonstrated with atomic magnetometers.

Atomic magnetometers are widely used for geological surveying and are commercially manufactured for this purpose. Different mineralogical deposits have distinct magnetic properties, making atomic magnetometers effective in detecting them. Magnetometers installed on aircrafts can rapidly survey large areas, while ground-vehicle-mounted or hand-held magnetometers provide detailed magnetic mapping of the area. Differential measurements performed by arrays of atomic magnetometers are used to find buried objects, such as archaeological artifacts and utility structures [29–31]. Similarly to locating buried objects and mineral deposits on land, atomic magnetometers installed on ships can locate ship wrecks, submarines and unexploded ordinance in the ocean [32,33]. Precise measurement of the magnetic field sheds light on the structure of the Earth and processes taking place in its interior. At depths of 40 to 50 km, subducting ocean crust goes through important metamorphic changes that produce serpentinite, a highly magnetic, low-density rock [34]. Presence of this rock can be detected and used for locating margins of subduction zones [34, 35]. It is predicted that the presence of serpentine in subduction regions is spatially correlated with large earthquakes.

Despite competing technologies, such as fluxgates, SQUIDs, or magnetomets utilizing NV centers, optical atomic magnetometers remain the sensors of choice for many of these applications.

1.2 Principles of operation

Atomic magnetometers operate by measuring the spin precession rate of the macroscopic atomic magnetic moment $\vec{\mu}$ in an external magnetic field $\vec{B}_0$ (Figure 1.1). The atoms precess at the Larmor frequency Ω_L, which is related to $\vec{B}_0$ by the gyromagnetic ratio γ of the atoms:

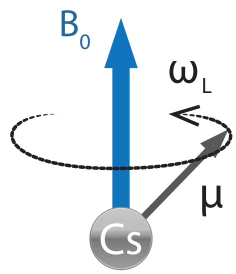

Figure 1.1: Atomic moment precessing in the magnetic field $\vec{B}_0$.

$$\Omega_L = \gamma B_0, \tag{1.1}$$

For small magnetic fields, the magnetic moment of atoms does not depend on the leading field $\vec{B}_0$ [36]. In this case, γ is only determined by the type of atoms and the physical constants, which eliminates the need for calibration.

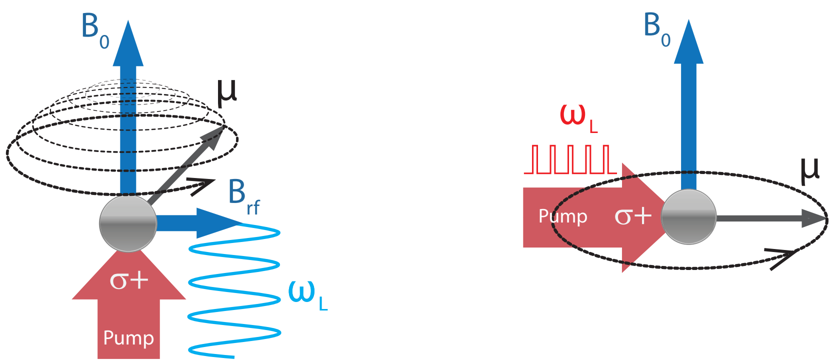

(a) Rf-driven magnetometer

(b) Bell-Bloom type magnetometer

Figure 1.2: Commonly used atomic magnetometer configurations

In optical magnetometers, the atoms are polarized by transferring the angular momentum from polarized light to the atoms in the process called optical pumping [37]. The original method was to orient the atomic spins along the measured magnetic field by placing them into a resonant circularly-polarized light wave [2] (Figure 1.2a). Spin precession is then induced by an additional oscillating magnetic field, which is orthogonal to the light propagation direction and resonant with the precession frequency. Another method, implemented within a few years afterwards, is to create the precessing polarization with an intensity-modulated resonant light propagating orthogonally to the magnetic field [5] (Figure 1.2b). When the light modulation frequency matches the Larmor frequency, the polarization induced by the subsequent pulses add up constructively, and the macroscopic precessing polarization builds up. Although these two methods are most commonly used, it is possible to induce spin precession by synchronously modulating other parameters of a magnetometer [36], such as the optical frequency [38], or polarization [39], or even the atomic spin relaxation rate [40].

An effective way to readout atomic precession is optical detection by polarized light. It provides a high signal-to-noise ratio and allows detecting the population difference between Zeeman energy levels separated by $\ll k_B T$. While there are many configurations that permit optical detection, we used balanced polarimetry with linearly polarized light (see [41] for more detail). In this method, linearly polarized probe light is tuned close to an optical transition, and propagates through the cell filled with polarized atoms (Figure 1.3a). The probe light can be decomposed into two orthogonal circularly polarized components $\sigma+$ and $\sigma-$. These components experience different birefringence and absorption in the atomic media, which depends on the orientation of the atomic magnetic moments (Figure 1.3b). The phase difference between $\sigma+$ and $\sigma-$ components results in rotation of the polarization plane, which can be detected with a balanced polarimeter [42]. A detailed description of the custom-made low-noise polarimeter circuit used in the experiments is presented in Appendix A.

Optical atomic magnetometers are often operated in self-oscillating regime, meaning that the detected signal is used to excite atomic precession in a positive feedback loop. A magnetometer constructed in such way behaves as an oscillator that tracks the magnetic field.

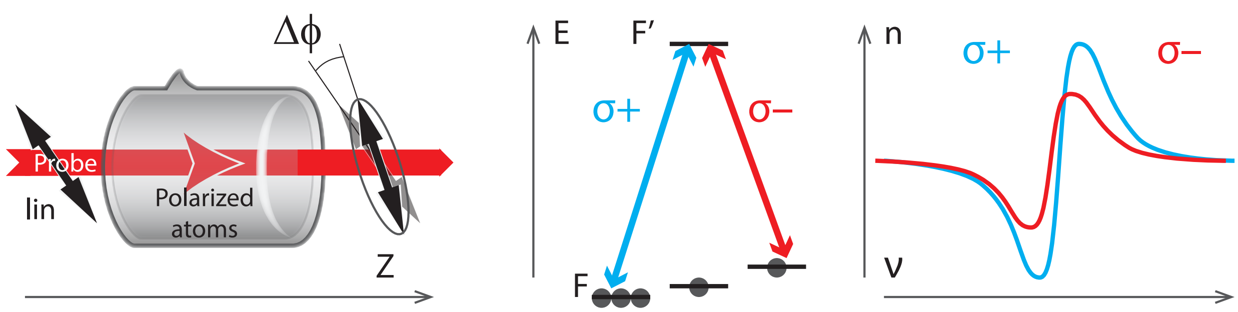

(a) Rotation of probe polarization plane induced by polarized atoms

(b) Sample energy levels of an optical transition with a population difference (left), and difference in refraction experienced by $\sigma+$ and $\sigma-$ components of the probe light.

Figure 1.3: Detection of atomic precession by measuring rotation of the polarization plane. Here the probe beam propagates along $\hat{z}$. In this basis, the linearly polarized light is equivalent to two circularly polarized components of equal intensity. As the atoms precess within the plane of the beam, the relative populations "seen" by the opposite circularly polarized components oscillate at Larmor freqency, which is detected as rotation of the probe polarization plane.

1.3 Signal and sensitivity

The purpose of this section is to provide an order of magnitude estimate of the optical rotation signal one can expect for the magnetometer setup used in this thesis, as well as the noise and sensitivity limits. A rigorous calculation of the magnetometer signal and noise values can be found in Refs. [43, 44].

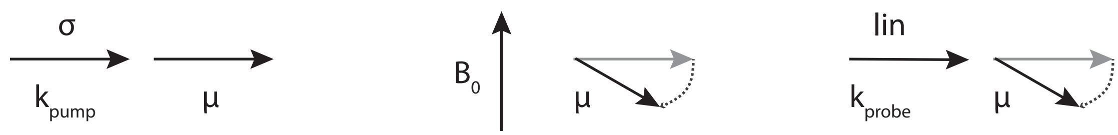

(a) Polarization (b) Precession (c) Probing

Figure 1.4: Simple magnetometer model

In this model the ^{133}Cs atoms are first prepared by a circularly-polarized light (pump) in the absence of the magnetic field (Figure 1.4a). Then the magnetic field $\vec{B_0}$ is switched on non-adiabatically in a direction orthogonal to the atomic magnetization, which then starts precessing at the Larmor frequency (Figure 1.4b). Finally, a linearly-polarized laser beam (probe) reads out the orientation of the magnetic moments at different moments of time (Figure 1.4c). The ^{133}Cs atoms are contained inside a cylindrical 50×50 mm paraffin-coated class cell at the temperature of 20 ℃. The pump beam (D_1 $F_g = 3 \rightarrow F_e = 4$) and the probe beam ($D_2$ $F_g = 4 \rightarrow F_e = 5$) have the same average power of 10 μW. In paraffin-coated cells the atoms bounce off the cell walls without depolarizing and can traverse the cell several thousand times before losing the polarization, so the exact intensity distribution does not matter, only the average (see Section 2.4).

The optical pumping rate for stationary atoms is given by Fermi's golden rule [36]:

$$\Gamma_{pump} = \frac{\Omega_R^2}{\Gamma_0}, \tag{1.2}$$

where Ω_R is the Rabi frequency of the pump beam, and Γ_0 is the spontaneous decay rate. The Rabi frequency of the pump can be found as:

$$\Omega_R = \frac{dE}{\hbar}, \tag{1.3}$$

where d is the relevant electric dipole moment, and E is the electric field amplitude of the pump laser light. In case of an alkali atom the dipole moment can be calculated using Eqs.

7.63 and 7.46 from [43]:

$$\langle \xi' J' I F' m' | d | \xi J I F m \rangle = (-1)^{F'-m'} \begin{pmatrix} F' & 1 & F \\ -m' & q & m \end{pmatrix} \langle \xi' J' I F' || d || \xi J I F \rangle =$$
$$= (-1)^{F'-m'+J'+I+F+1} \sqrt{(2F+1)(2F'+1)} \begin{pmatrix} F' & 1 & F \\ -m' & q & m \end{pmatrix} \begin{Bmatrix} J' & F' & I \\ F & J & 1 \end{Bmatrix} \langle \xi' J' || d || \xi J \rangle \,, \tag{1.4}$$

where I is the nuclear spin, J is the angular momentum of the electron, F, m are the total angular momentum of the atom and its projection on the quantization axis, ξ designates the remaining quantum numbers, q is the projection of the light's angular momentum on the quantization axis, $\begin{pmatrix} F' & 1 & F \\ -m' & q & m \end{pmatrix}$ and $\begin{Bmatrix} J' & F' & I \\ F & J & 1 \end{Bmatrix}$ are a three-J and a six-J symbols, and $\langle \xi' J' I F' || d || \xi J I F \rangle$ is a reduced matrix element of the dipole moment. The variables ξ, J, F, m and ξ', J', F', m' describe the ground and the excited states, correspondingly. For each combination of F and F' there are multiple transitions excited with different m and m'. To find the optical pumping rate, I will average $|d|^2$ over m assuming that the atoms in the ground state are unpolarized, in which case the result does not depend on the pump polarization. The average $|d|^2$ values calculated in Mathematica for every combination of F and F' in ^{133}Cs are presented in the Tables 1.1 and 1.2.

	$F' = 3$	$F' = 4$
$F = 3$	0.39	1.18
$F = 4$	1.18	0.84

Table 1.1: Average $|d|^2$ for ^{133}Cs D_1 line in units of $(ea_0)^2$

	$F' = 2$	$F' = 3$	$F' = 4$	$F' = 5$
$F = 3$	1.11	1.16	0.83	0
$F = 4$	0	0.39	1.16	2.44

Table 1.2: Average $|d|^2$ for ^{133}Cs D_2 line in units of $(ea_0)^2$

When the pump power of $10\,\mu$W is distributed uniformly over the cell area, the light electric field amplitude is:

$$E = \sqrt{\frac{2I}{cn\epsilon_0}} = \sqrt{\frac{2 \cdot 10^{-5}\ [\mathrm{W}] / \left(0.05\ [\mathrm{m}]\right)^2}{3 \cdot 10^8\ [\mathrm{m/s}] \cdot 1 \cdot 8.8 \cdot 10^{-12}\ [\mathrm{F/m}]}} = 1.7\ [\mathrm{V/m}]. \tag{1.5}$$

Then the optical pumping rate for the light addressing D_1 $F_g = 3 \to F_e = 4$ can be found as:

$$\Omega_R^2 = \frac{1.18 \times \left(1.6 \times 10^{-19} \cdot 5.3 \times 10^{-11}\right)^2 [\mathrm{C}^2 \cdot \mathrm{m}^2] \cdot \left(1.7 \times [\mathrm{V/m}]\right)^2}{\left(1.1 \times 10^{-34} [\mathrm{J} \cdot \mathrm{s}]\right)^2} = 2.3 \times 10^{10}\ \mathrm{s}^{-2}, \tag{1.6}$$

$$\Gamma_{pump} = \frac{2.3 \times 10^{10}\ \mathrm{s}^{-2}}{33 \times 10^{6}\ \mathrm{s}^{-1}} \simeq 730\ \mathrm{s}^{-1}. \tag{1.7}$$

In reality the ^{133}Cs atoms are not stationary, and the atomic transition is Doppler-broadened with the width of an order of 300 MHz. The fraction of time the ^{133}Cs atoms are resonant to the pump light can be roughly estimated as the ratio of the natural and broadened line widths $\Gamma/\gamma_{\mathrm{D}} = 5\,\mathrm{MHz}/300\,\mathrm{MHz} \simeq 0.02$. This results in decrease of Γ_{pump} to an order of 12 transitions per atom per second. In a paraffin-coated cell the relaxation rate of the polarization in the ground state is $\Gamma_{\mathrm{rel}} \simeq 7\,\mathrm{s}^{-1} \sim \Gamma_{pump} \simeq 12\,\mathrm{s}^{-1}$, mostly limited by the spin-exchange collisions (MR width of 2 Hz). In this case the polarization degree of the atoms is of an order of one.

The optical rotation magnitude of the probe beam polarization plane can be estimated using a model of an atom as a harmonic oscillator. The absorption and refractive index in proximity of the transition frequency are given by (Griffith [45] Eqs. 9.170 and 9.171):

$$\begin{aligned} n(\omega) &\simeq 1 + \frac{ne^2}{2m\epsilon_0} \sum_j \frac{f_j\left(\omega_j^2 - \omega^2\right)}{\left(\omega_j^2 - \omega^2\right)^2 + \gamma_j^2\omega^2}, \\ \alpha(\omega) &\simeq \frac{ne^2\omega^2}{m\epsilon_0 c} \sum_j \frac{f_j\gamma_j}{\left(\omega_j^2 - \omega^2\right)^2 + \gamma_j^2\omega^2}, \end{aligned} \tag{1.8}$$

where n is the number density of atoms, e is the electron charge, m is the electron mass, ω_j is a transition frequency, f_j is the oscillator strength of the transition, γ_j is the upper state decay rate, and ω is the optical frequency. When the equations are re-written in terms of the resonant absorption length l_0, the refractive index becomes:

$$n(\omega) = 1 + \frac{c\gamma}{l_0} \frac{\omega_0^2 - \omega^2}{\left(\omega_0^2 - \omega^2\right)^2 + \gamma^2\omega^2}, \tag{1.9}$$

where γ is the decay rate of the state addressed by the probe laser. By defining $\omega = \omega_0 + \Delta$ and assuming $\Delta \ll \omega_0$, the expression can be further simplified as

$$n(\omega) = 1 - \frac{c}{l_0} \frac{2\Delta\omega_0\gamma}{(2\Delta\omega_0)^2 + \gamma^2\omega_0^2}. \tag{1.10}$$

The linearly polarized probe beam can be thought of as a superposition of coherent $\sigma+$ and $\sigma-$ components propagating along the probe wave vector. When the quantization axis is chosen to be parallel to the probe wave vector, each of the polarization components acquires a phase shift depending on the population distribution of the ground state. As the atoms precess, the populations of the ground states oscillate, which results in oscillations in the absorption coefficient and the refractive index. The difference in the refractive index for the polarization components causes the polarization plane of the probe light to rotate by the angle $\Delta\varphi$:

$$\Delta\varphi(\omega) = \frac{\omega l}{2c}\left[n_+(\omega) - n_-(\omega)\right], \tag{1.11}$$

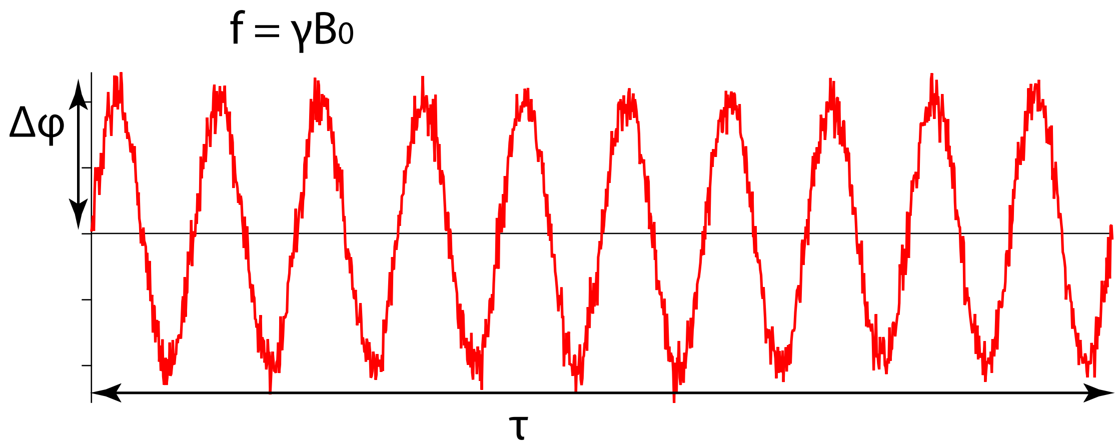

Figure 1.5: Simulated optical rotation signal

where $l = 5$ cm is the length of the magnetometer cell. To estimate the optical rotation signal magnitude, let us consider the case when all atoms are in the state $F_g = 4, m = 4$ and the quantization axis parallel to the probe propagation vector. The $\sigma+$ component can only excite the cycling transition to $F_e = 5,\ m = 5$ state, which has the cross section $\sigma_{0(+)} = 3.5 \times 10^{-9}$ cm^2. The $\sigma-$ component can excite transitions to $F_e = 3, 4, 5$ $m = 3$ states with the total cross-section of $\sigma_{0(-)} = 1.1 \times 10^{-9}$ cm^2. For the stationary atoms, the absorption length for each component is $l_0 = 1/n\sigma_0$. At 20 ℃ the concentration of ^{133}Cs atoms is $n = 3 \times 10^{10}\,\mathrm{cm}^{-3}$ [46], and the resonant absorption lengths are (without taking the Doppler broadening into account):

$$\begin{aligned} l_{0,\sigma+} &= 1/(3.4 \times 10^{-9}\ \mathrm{cm}^2 \cdot 3 \times 10^{10}\ \mathrm{cm}^{-3}) = 9.5 \times 10^{-5}\ \mathrm{m}, \\ l_{0,\sigma-} &= 1/(1.1 \times 10^{-9}\ \mathrm{cm}^2 \cdot 3 \times 10^{10}\ \mathrm{cm}^{-3}) = 3.0 \times 10^{-5}\ \mathrm{m}. \end{aligned} \tag{1.12}$$

When the probe frequency is close to the optical transition and $\Delta \simeq \gamma$:

$$n(\omega) = 1 - \frac{c}{l_0\omega_0} \cdot \frac{2\gamma^2}{(2\gamma)^2 + \gamma^2} = 1 - \frac{2}{5} \cdot \frac{c}{l_0\omega_0}. \tag{1.13}$$

The optical rotation amplitude is then:

$$|\Delta\varphi(\omega)| = \frac{\omega l}{2c}\Delta n(\omega) \simeq \frac{\omega_0 l}{5c}\left[\frac{c}{\omega_0 l_0(\sigma-)} - \frac{c}{\omega_0 l_0(\sigma+)}\right] = \frac{l}{5}\left[\frac{1}{l_0(\sigma-)} - \frac{1}{l_0(\sigma+)}\right] \simeq 70\ [rad]. \tag{1.14}$$

Since the transition is Doppler broadened, the probe rotation signal is a superposition of the signals from each velocity subgroup. In ^{133}Cs the Doppler width (~ 300 MHz) is two orders of magnitude larger than the natural transition line width (~ 5 MHz), so the actual rotation signal on resonance would be $\Delta\varphi \simeq 1$ rad $\simeq 60°$ (as explained in [43] section 10.2.8).

The exact quantum-mechanical solution for ^{133}Cs is cumbersome because of the number of the atomic states is large. The full set of equations needed to solve it exactly can be found in [47], and integrated numerically with the ADM package[1] for Mathematica by Simon Rochester. An analytic solution for the case of $F = 1$ is presented in [43]. A detailed theoretical description of an alignment-based magnetometer with spin precession induced by an rf-field can be found in [44].

A simulated optical rotation signal with (exaggerated) noise is presented in Figure 1.5. The main noise contributions come from the shot noise of the probe, atomic projection noise, and technical noise. Photon shot noise and projection noise set fundamental limits on the magnetometer sensitivity, while the technical noise can be minimized or worked around. In the experiments described in this work, the magnetometer signal was dominated primarily by the technical noise.

Photon shot noise is caused by stochastic fluctuations in the number of photons that reach each polarimeter channel during the time of the measurement. If the measurement time is τ seconds, and the number of photons detected per second is Φ, the uncertainty in the measured polarization angle is (see [43] and problem 8.9 in [48]):

$$\Delta\varphi \simeq \frac{1}{2}\sqrt{\frac{1}{\Phi\tau}}\ [\mathrm{rad}/\sqrt{Hz}]. \tag{1.15}$$

For the setup described in this thesis, the typical photon shot noise was 3.2:

$$\Delta\varphi \simeq \frac{1}{2}\sqrt{\frac{1}{4\times10^{12}\ [\mathrm{ph/s}]\cdot 1\ [\mathrm{s}]}} = 0.25\times10^{-6}\ [\mathrm{rad}/\sqrt{\mathrm{Hz}}]. \tag{1.16}$$

Given that the typical FWHM of the magnetic resonance in the experiment was 3 Hz, and ^{133}Cs gyromagnetic ratio is $g \sim 3.5$ Hz/nT, the typical shot noise limit is of an order of:

$$\delta B \simeq \frac{3\ [\mathrm{Hz}]}{3.5\ [\mathrm{Hz/nT}]}\cdot\frac{\delta\varphi}{\pi/3} = 0.2\times10^{-6}\ [\mathrm{nT}/\sqrt{\mathrm{Hz}}] = 0.2\ [\mathrm{fT}/\sqrt{\mathrm{Hz}}]. \tag{1.17}$$

The spin-projection noise is caused by the statistical uncertainty in the magnetic moment projections measurement of the atomic ensemble. For the measurement times $\tau \gg \Gamma_{\mathrm{rel}}$ [36]:

$$\delta B \simeq \frac{1}{g}\sqrt{\frac{\Gamma_{\mathrm{rel}}}{N\tau}}, \tag{1.18}$$

where N is the total number of atoms the measurement is performed with. For this experiment, the typical value was:

$$\delta B \simeq \frac{1}{3.5\ [\mathrm{Hz/nT}]}\sqrt{\frac{1\ [\mathrm{Hz}]}{3\cdot10^{10}\ [\mathrm{cm}^{-2}]\cdot\pi\cdot(2.5\ [\mathrm{cm}])^2\cdot 5\ [\mathrm{cm}]\cdot 0.05}} \simeq 0.8\ [\mathrm{fT}/\sqrt{\mathrm{Hz}}]. \tag{1.19}$$

In the actual experiments the noise was dominated by the technical sources, primarily the leading field instabilities, as well as the power and frequency fluctuations in the lasers (and

[1] http://rochesterscientific.com/ADM/

their respective light shifts). The best sensitivity level achieved throughout the experiments was $50\,\mathrm{fT}/\sqrt{\mathrm{Hz}}$ at 1 Hz frequency, limited by the leading field noise. In addition to that, more low-frequency magnetic noise was produced by the equipment, elevators in the building and the power lines. Other sources of measurement errors in atomic magnetometers are described in great detail in [36]. The low-frequency noise and electronics noise of the polarimeter are discussed in [49].

1.4 The AC-Stark effect in alkali atoms

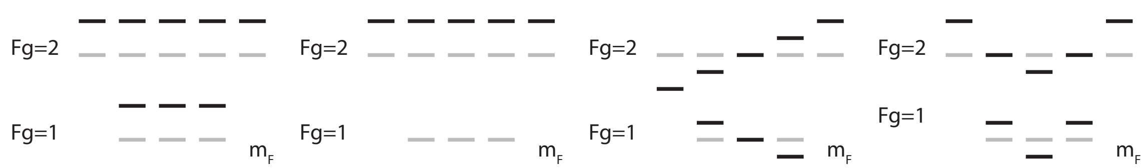

(a) C.m. light shift (b) Hfs light shift (c) Vector light shift (d) Tensor light shift

Figure 1.6: Light shifts in the ground state of an alkali atom

Atomic magnetometers determine the magnetic field value by measuring the precession rate in the ground state of the atoms. When the atoms are placed into an optical field (such as the probe and pump beams of an optical magnetometer), the ground-state magnetic sublevels energy shift due to the perturbations from the light field. When the light optical frequency is sufficiently far from the transition frequency so that the probability of the atoms to absorb the light is small, the changes in the precession rate are primarily caused by the AC Stark effect [50], that can be described by the operator:

$$\delta E = (\delta E)_0 + \delta\mathcal{A}\vec{I}\cdot\vec{S} + \vec{\mu}\cdot\vec{B}_{LS} + (\delta E)_t\,. \tag{1.20}$$

The terms of this operator can be categorized by the effect they have on the ground state. The center-of-mass light shift $(\delta E)_0$ (Figure 1.6a) does not depend on m_F, and causes the ground state to shift as a whole. The hfs light shift $(\delta\mathcal{A}\vec{I}\cdot\vec{S})$ (Figure 1.6b) does not depend on m_F either, and is equivalent to the change in the magnetic-dipole coupling constant causing the hfs transition frequencies to change. The vector light shift $(\vec{\mu}\cdot\vec{B}_{LS})$ (Figure 1.6c) is proportional to m_F, and is equivalent to a magnetic field applied to the atoms in the direction of the light propagation [51]. The tensor light shift $(\delta E)_t$ (Figure 1.6d) is quadratic with m_F, and is equivalent to an electric field applied to the atoms.

The main focus of this dissertation is the vector light shift effect and its applications. The scalar and hfs light shifts are not considered because they do not change the Zeeman splitting in the ground state, and thus do not affect atomic magnetometers reading. While the tensor light shifts do affect the Zeeman splitting, in the experiments with our parameters the effect was much smaller than the magnetic resonance and was not measurable. However, when the magnetic field is sufficiently large, tensor light shifts can be exploited to improve the sensitivity by canceling out the quadratic Zeeman effect and reducing the MR width [52, 53].

The light shift beams in the experiments were circularly polarized, and produced both tensor and vector light shifts. It is equivalent to a combination of electric and magnetic fields in parallel with $\vec{k}$ of the light [51]. A detailed theoretical calculation of the light shifts in ^{133}Cs atoms for an arbitrary light polarization, optical frequency and light power can be found in [54]. Experimental data measured for ^{133}Cs D_1 and D_2 lines with circularly-polarized light are presented in Section 2.2.

Chapter 2

Vector light shift in a magnetometer with coated cell

2.1 Motivation

In this section we experimentally investigate several aspects of the vector light shifts in coated ^{133}Cs cells. Although light shift effect in atomic magnetometers has been extensively studied before [55–60], we were unable to readily apply these results to our setup because our sensor cell has paraffin coating. The goal of this work was to explore the parameter space of our setup and find the optimal conditions for demonstrating the practical light-shift magnetometer applications, such as the all-optical vector magnetometer (Section 3.2). Another goal was to obtain reference data on the dependence of the measured fictitious field on light power and optical frequency for upcoming light-shift spin manipulation experiments. These data also helped to find the origin of unexpected phase shifts we encountered when a dedicated light shift beam was introduced into the setup, which was important for constructing sensors with auxiliary light-shift beams. We subsequently maximized this effect to demonstrate another vector light-shift application and build an all-optical rf-like magnetometer (Section 3.1).

First part of this chapter explores how the measured magnetometer frequency depends on power and optical frequency of the light shift beam. In the second part we investigate whether the vector light shift in our setup can be treated as average over the cell independent of the beam profile.

2.2 Optical frequency and power dependence

Experimental setup

Schematic of the magnetometer used to take the data is presented in Figure 2.1. In the middle of the apparatus, a paraffin-coated ^{133}Cs vapor cell (cylinder 50 mm×50 mm, $T_1 \sim 0.7s$ T=24 ℃) is placed inside in a four-layer μ-metal shield, which attenuates the external

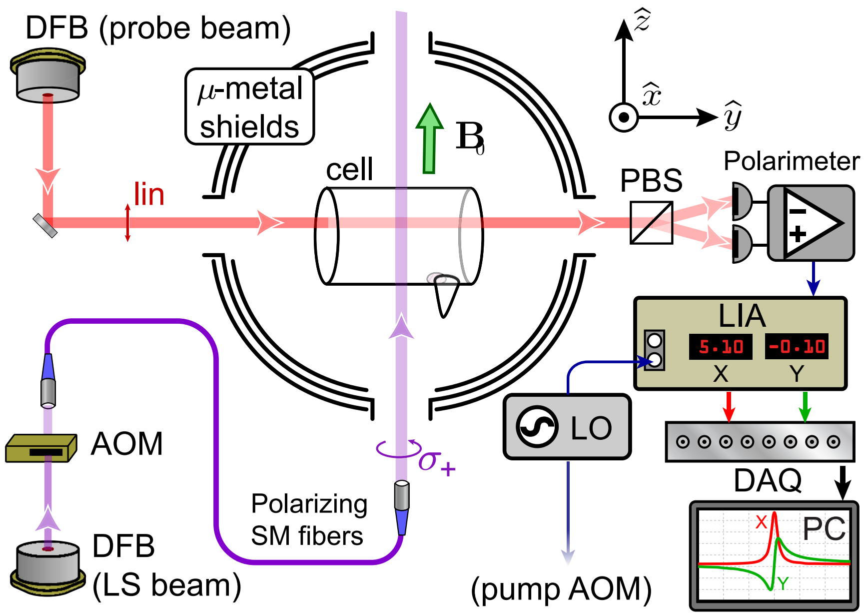

Figure 2.1: Experimental schematic. An amplitude-modulated, circularly polarized pump beam (not shown) propagates in the $\hat{x}$ direction. The local oscillator (LO) controls the pump AOM and serves as a reference to the lock-in amplifier (LIA), whose analog output is recorded by a data acquisition card (DAQ) and read into a computer (PC). A linearly polarized probe beam passes through the cell and is split by the polarizing beamsplitter (PBS) of a balanced polarimeter; the output of this polarimeter is demodulated by the lock-in. Circularly-polarized light-shift beam is parallel to the leading field $\vec{B}_0$.

magnetic field noise of the laboratory environment and allows for a controlled magnetic field environment. A set of orthogonal coils inside the shields serves for producing the leading magnetic field $\vec{B}_0$ and compensating the field gradients.

The main source of noise in the measurement are the technical fluctuations in the leading field as it is parallel to the measured fictitious field induced by the vector light shift. To minimize the impact, the B_z and dB_z/dz fields are produced by an ultra-stable current source exhibiting the drifts of < 50 ppb per 100 seconds (Magnicon 1011-CSE-2, Magnicon GmbH). Fields in other directions have less significant impact on the experiment sensitivity, since they are orthogonal to the leading field so their contribution is attenuated by a factor of $(\delta B/B_0)^2$.

Circularly polarized pump beam (DFB, $0.5\,\mu$W average, D_2) propagates along the x̂. The beam is power modulated by an AOM at Larmor frequency (3345.2 Hz), polarizing the atoms orthogonally to $\vec{B}_0$. The modulation waveform is a square wave with the duty cycle of 2%. The signal was synthesized by a frequency generator (BNC 645). The probe beam (DFB, $16\,\mu$W, D_2) is linearly polarized with $\vec{E} \parallel \hat{z}$ and propagates along ŷ, and is orthogonal to both the pump beam and $\vec{B}_0$. After passing the cell, the probe is detected by a differential photoamplifier (Section A) that measures the probe polarization rotation. The signal is demodulated at the Larmor precession frequency by a lock-in amplifier (SR830) whose output is recorded by a NI DAQ (USB-6353).

Estimated photon shot-noise limited sensitivity of the apparatus was $\sim 2\,\mathrm{fT}/\sqrt{\mathrm{Hz}}$. The actual sensitivity of the setup (without the light shift beam) was largely impacted by the technical noise, and measured $\sim 200\,\mathrm{fT}/\sqrt{\mathrm{Hz}}$. The sources of noise include instability of the current provided by the main coil driver, and instability of the lasers' power and optical frequency. When the light shift beam is turned on, its power fluctuations become the dominant source of noise when it is tuned close to the optical transitions.

The light shift beam (LS beam) is circularly polarized and propagates along $\vec{B}_0$ in order to maximize the measured MR frequency shift due to vector light shift effect. Optical frequency of the LS beam is actively stabilized by a software PID loop referenced to a wave meter (Ångstrom/HighFinesse WS-7). The power of the LS beam is controlled by a PID controller in a feedback loop with an AOM. The reference signal is obtained by sampling the LS beam with a pickoff placed before the polarization cleanup optics in front of magnetic shields entrance. This signal is recorded throughout the experiment and provides a measurement of the average LS beam power. The conversion of the pickoff voltage to the photo current is $175.5\,\mu\mathrm{A/V}$.

The measurement procedure

The precession signal from the polarimeter signal is demodulated by a lock-in amplifier at pump beam pulse frequency. The X and Y channels of the lock-in amplifier are recorded by a data acquisition system, along with the LS beam power pickoff signal. Slow forced-oscillation MR scans are acquired by varying the frequency of the pump pulses in vicinity of magnetic resonance while recording lock-in X and Y channels. The entire MR scan takes approximately 60 seconds to complete. The X and Y data is then fit to a complex Lorentzian in order to extract the amplitude, width, phase and the center frequency.

Optical frequency of the LS beam is scanned across the optical transitions of ^{133}Cs. At each frequency, several data points with different optical LS powers are recorded (5 points for D_1 line data set and 4 points for D_2 line data set). In order to mitigate the contribution of slow leading field drifts in the apparatus, two forced-oscillation MR scans are taken, with the LS beam blocked and opened. For each optical frequency, the dependence of the fit parameters on the light power is fit to a line, providing shifts in phase, center frequency, amplitude and width per μW of the LS beam power. The same set of measurements is repeated twice for D_1 and D_2 lines of ^{133}Cs.

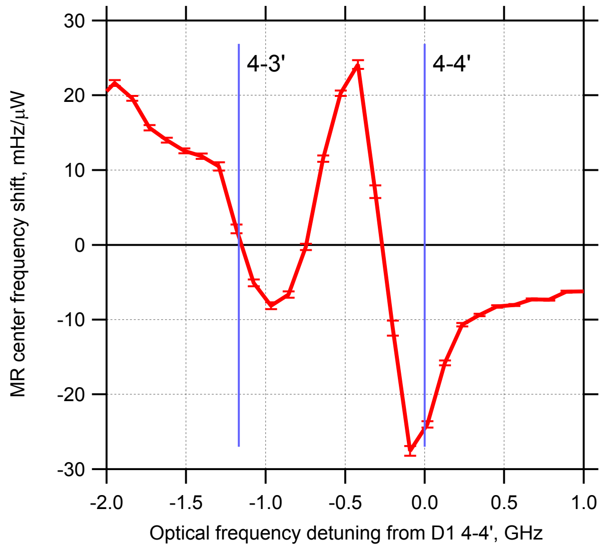

(a) Center frequency shift

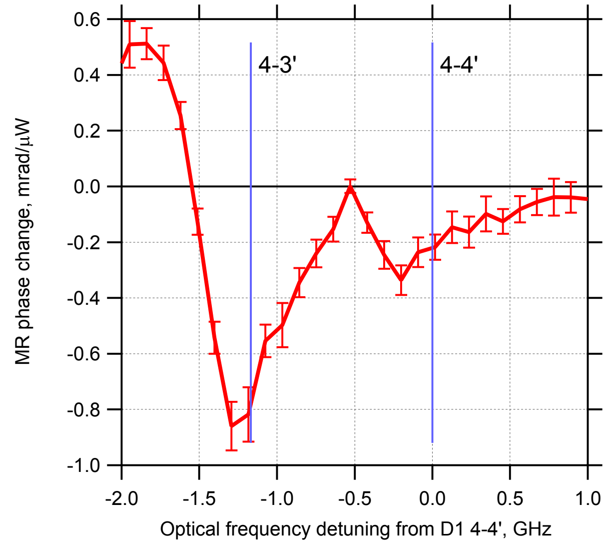

(b) Phase change

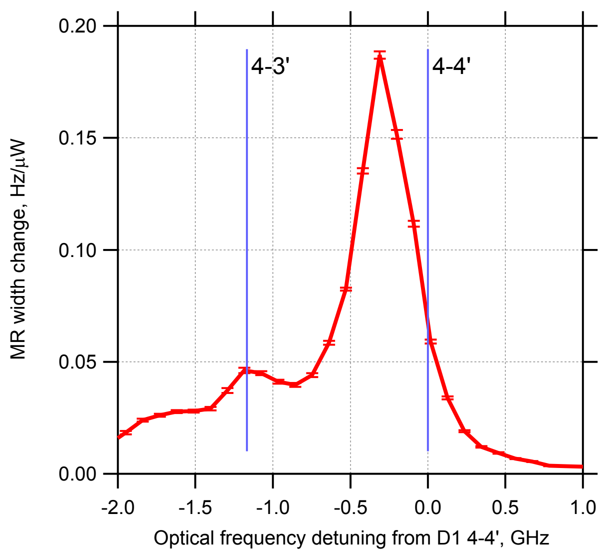

(c) Width change

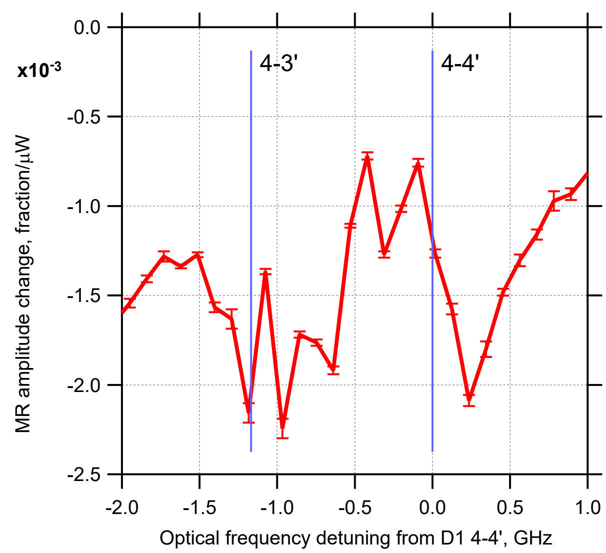

(d) Amplitude change

Figure 2.2: Power dependence of magnetic resonance fit parameters for different light shift optical frequencies (^{133}Cs D_1 line).

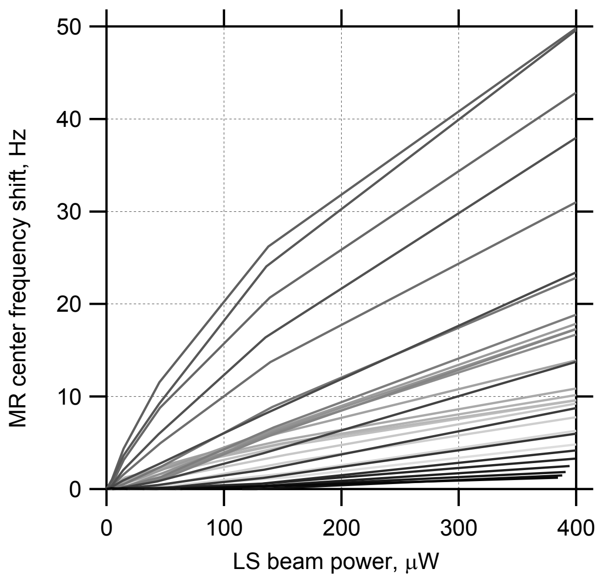

(a) Center frequency shift

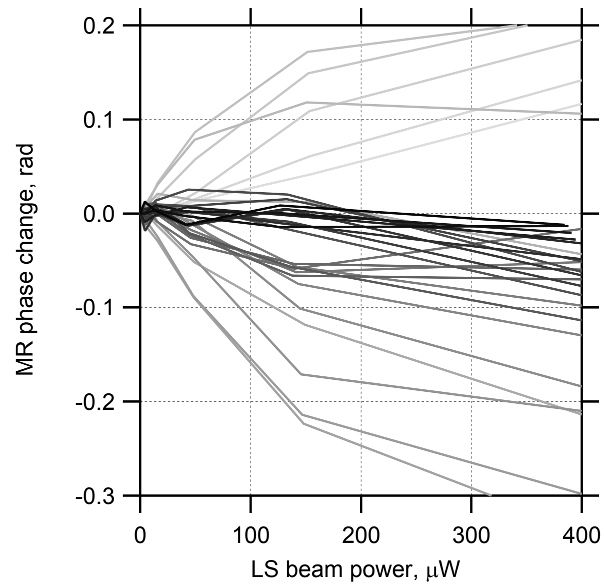

(b) Phase change

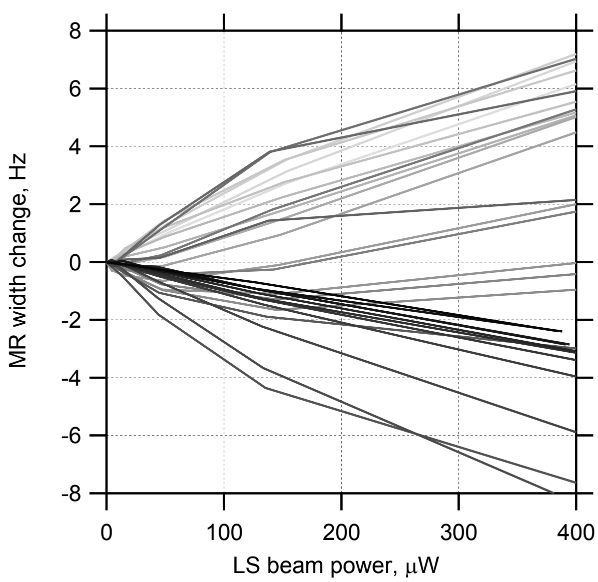

(c) Width change

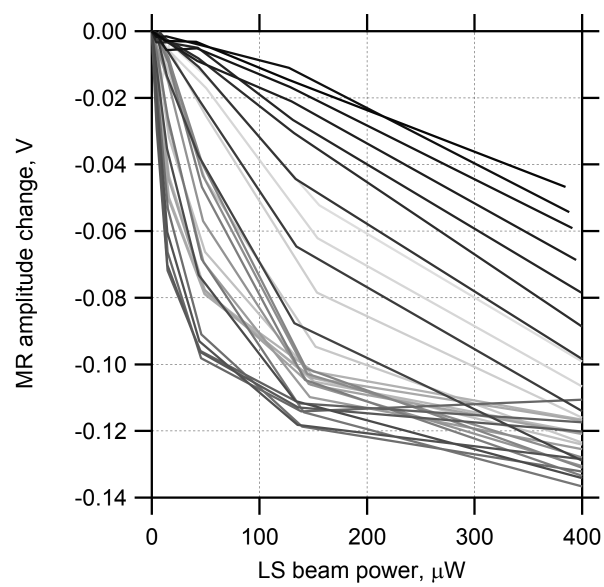

(d) Amplitude change

Figure 2.3: Non-linearity of the magnetic resonance fit parameters for different optical detunings with change of the optical power (^{133}Cs D_1 line). Different shades of gray represent distinct optical frequencies of the LS beam.

Results

D1 line

Figure 2.2 shows how the center frequency, phase, amplitude and width of the magnetic resonance depends on optical frequency tuning and power of the LS beam. The center frequency shift (Figure 2.2a) corresponds to the amplitude of the fictitious "magnetic field" induced by the vector light shift. As the frequency is tuned across the hyperfine structure of the excited hyperfine sublevels, the center frequency shift changes sign. Depending on the tuning, the measured center frequency shift was in the range of 10–20 mHz/ μW, equivalent to 3–6 pT/ μW. Optical pumping by the LS beam results in broadening of the MR (Figures 2.2d and decrease in the amplitude (Figure 2.2d). Since the broadening is induced by the real transitions, it is proportional to the absorption probability $1/\left(\omega^2+\omega_0^2\right)$. At the same time, the MR center shift is proportional to the media dispersion $\omega/\left(\omega^2+\omega_0^2\right)$, and for far detuned beam it falls of as $1/\omega$ as opposed to $1/\omega^2$ for the real transitions. For this reason, in order to attain large fictitious field while keeping the broadening minimal, it makes sense to work in far-detuned regime with large LS beam intensity. The figure of merit then would be the ratio of the vector light shift induced to the line broadening caused (Figure 2.6). The phase shift induced by the light shift beam is discussed in more detail in Section 2.3.

For large LS beam power, the resonance fit parameters stop growing linearly with power (Figures 2.3). This might be caused by saturation effects and by the LS beam depolarizing the atoms and optically pumping them out of the probed ground state $F_g = 4$. The original data used to produce the plots for ^{133}Cs D_1 line can be found in a data repository at http://budker.berkeley.edu/∼lena.

D2 line

The dependence of the MR line fit parameters on the optical frequency in case when the LS beam is scanned across ^{133}Cs D_2 line is presented on the Figure 2.4. Due to the unresolved ground state hyperfine structure, the frequency shift changes sign as the LS beam is tuned across $F_g = 4$ transitions (Figure 2.4a). The amplitude of the MR can both decrease or increase, depending on the LS beam optical frequency tuning. When the LS beam is tuned to $F_g = 4$, it pumps the atoms out of the state addressed by the probe, decreasing the signal amplitude. When it is tuned to $F_g = 3$ it has the opposite effect, repumping the atoms from the ground state back into $F_g = 4$ and increasing the number of atoms that form the magnetic resonance. Similarly to ^{133}Cs D_1 line results, the MR fit parameter changes saturate at some point and stop scaling linearly with the increase of the LS beam power (Figure 2.5).

The MR width can either increase or decrease after due to introduction of the LS beam. When the it addresses $F_g = 4$, it speeds up relaxation of the polarized atoms due to the optical pumping, broadening the magnetic resonance. On the contrary, when the LS beam addresses $F_g = 3$, the MR line width decreases due to the light narrowing effect [61]. The MR width in the experiment is limited by the spin-exchange collisions. The only collision

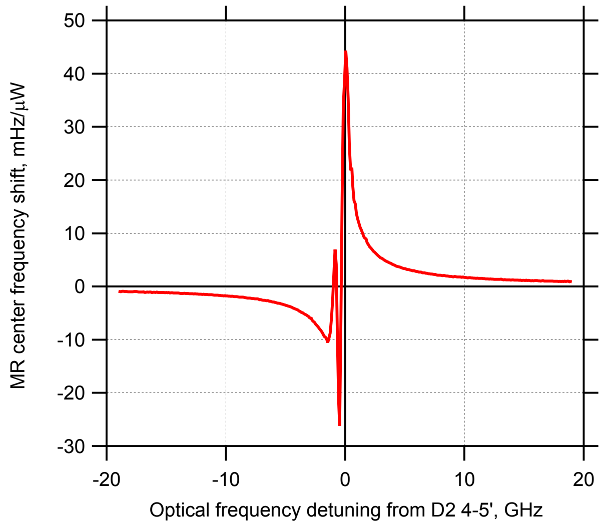

(a) Center frequency shift

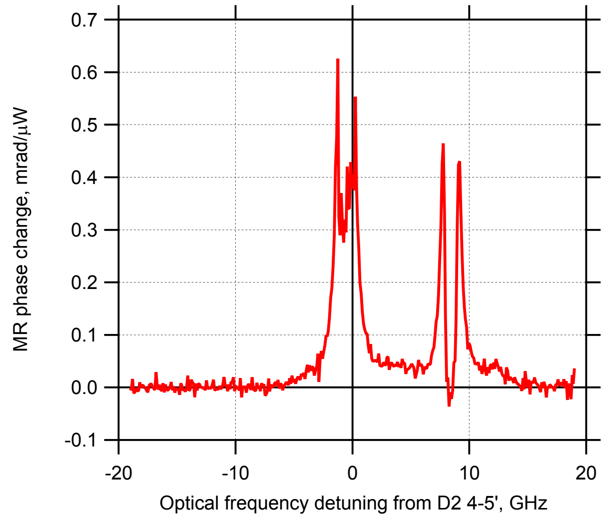

(b) Phase change

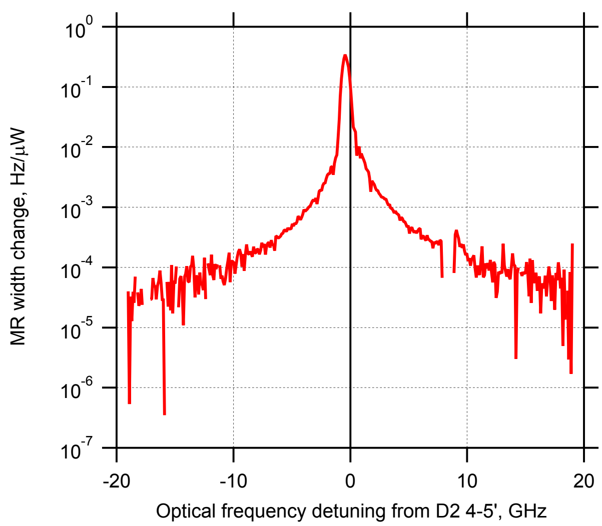

(c) Width change

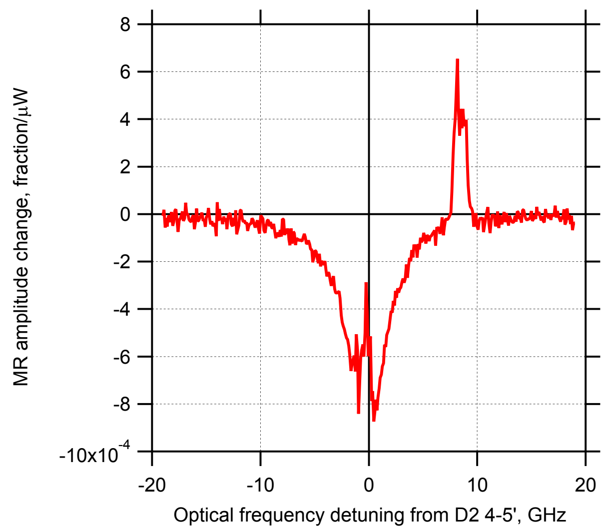

(d) Amplitude change

Figure 2.4: Power dependence of magnetic resonance fit parameters for different light shift optical frequencies (^{133}Cs D_2 line). Different shades of gray represent distinct optical frequencies of the LS beam.

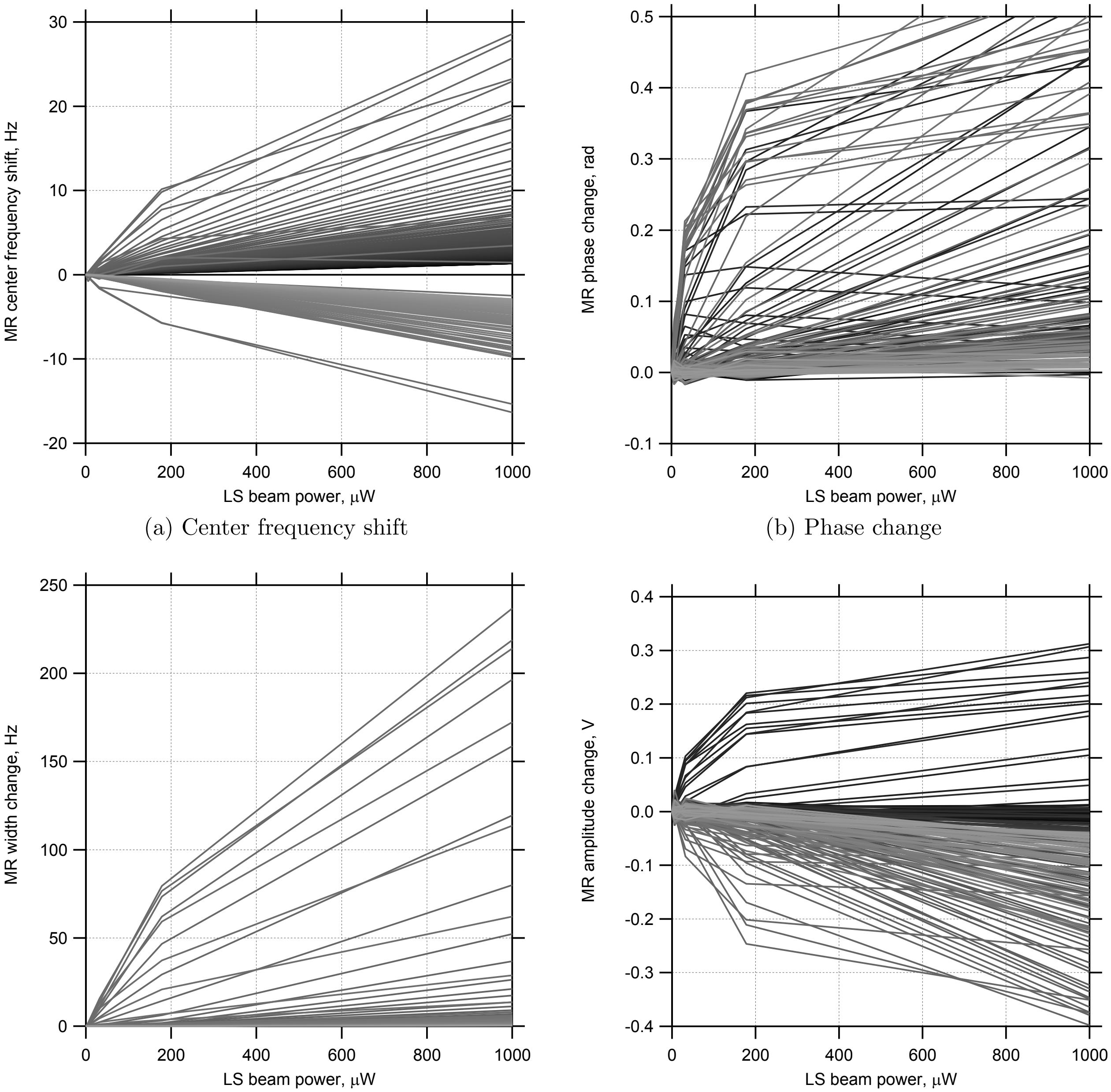

(a) Center frequency shift

(b) Phase change

(c) Width change

(d) Amplitude change

Figure 2.5: Non-linearity of the magnetic resonance fit parameters for different optical detunings with change of the optical power (^{133}Cs D_2 line). Different shades of gray represent distinct optical frequencies of the LS beam.

that cannot result in the atoms changing the angular momentum state is when two atoms in $F_g = 4$ $m = 4$ collide with each other. Spin-exchange relaxation together with the LS beam emptying $F_g = 3$ result in atoms accumulating in the state immune to spin-exchange relaxation, thus narrowing the magnetic resonance [62]. In particular, this effect causes the sign reversal of the MR frequency shift and line broadening ratio on Figure 2.6 at +9 GHz detuning.

The LS beam affects the phase of the magnetic resonance, even when it is tuned to the ground state the probe beam does not interact with. This effect is discussed in more detail Section 2.3. The original data used to produce the plots for ^{133}Cs D_2 line can be found in the linked file.

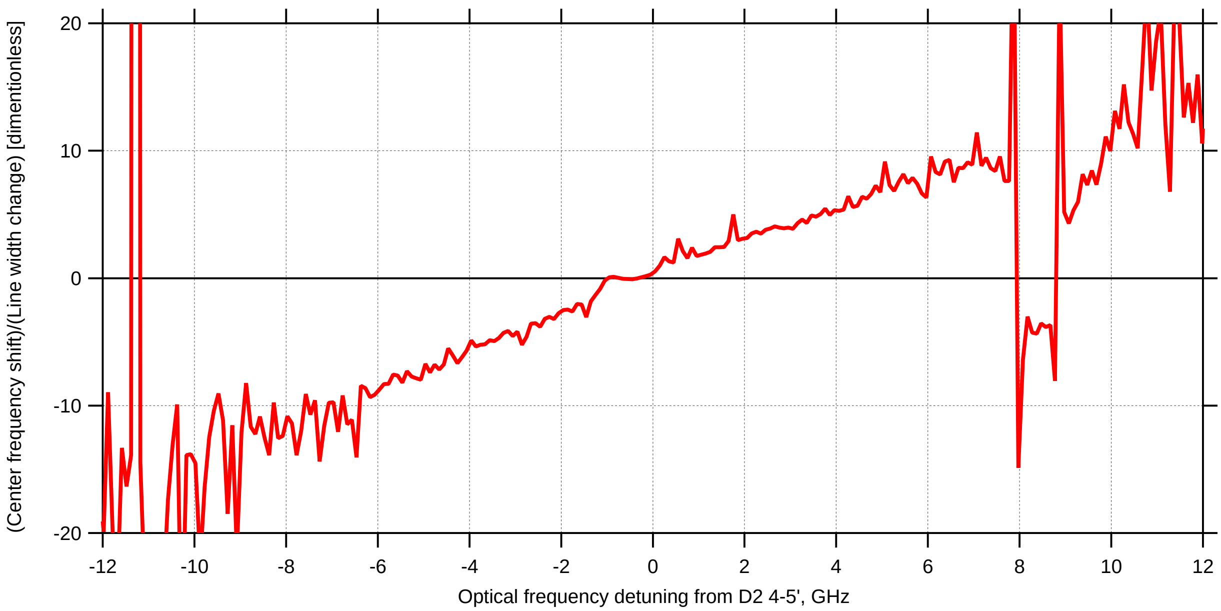

Figure 2.6: Ratio of the MR frequency shift to the line broadening induced by the LS beam. This indicates that one can attain bigger fictitious field magnitudes while retaining magnetometer sensitivity when using large optical detunings. The sign reversal at ~ 9 GHz detuning is an indication of the light narrowing due to the atoms accumulating in $F_g = 4$ $m = 4$ caused by the LS beam clearing $F_g = 3$ state.

2.3 Phase shift

We have encountered an unexpected phase shift effect while investigating how an atomic magnetometer with a paraffin-coated sensor cell behaves in a presence of a light-shift beam (Section 2.2). The phase of the magnetic resonance appeared to depend on power and optical frequency of the light-shift beam. In particular, the phase is affected when the LS beam is far-detuned from the optically probed ground state containing the precessing atoms, when

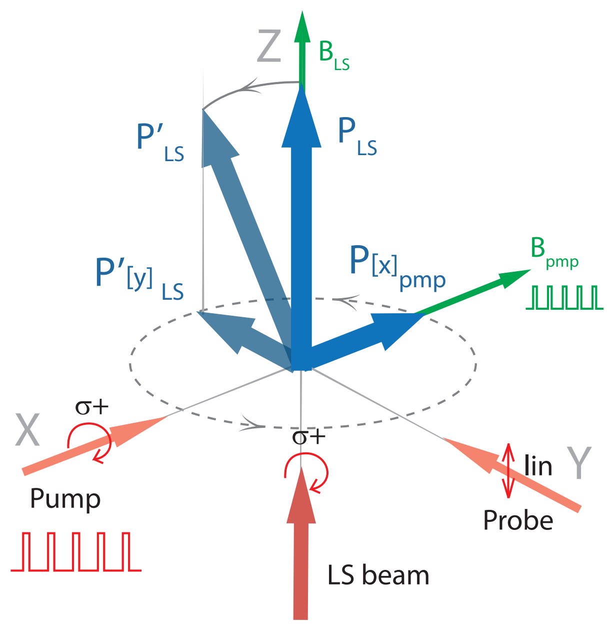

Figure 2.7: Scheme of a magnetometer with a light-shift beam. Red arrows represent laser beam $\vec{k}$ vectors, blue arrows indicate the induced polarization, while green arrows show the fictitious magnetic field directions. Atomic polarization P_{pmp} is produced by the pump beam, while P_{LS} is induced by the light shift beam. P_{LS} is "tipped" by B_{pmp} out of Z direction and becomes P'_{LS}. $P'_{[y]LS}$ is the projection of the P'_{LS} onto the X-Y plane. The 90° angle between $P'_{[y]LS}$ and P_{pmp} causes the perceived MR phase change when the superposition of the two precessing polarizations is detected by the probe.

one would not expect them to be significantly affected. We investigated the effect in detail to gain a deeper understanding of the processes happening in the setup before proceeding to any experiments involving the LS beams.

In essence, introduction of the LS beam creates another magnetometer within the setup that shares the same sensor cell. The signal of the new magnetometer has a 90° phase shift compared to the original magnetometer. Superposition of the two precession signals is detected by the polarimeter and appears as a phase shift after demodulation by a lock-in. Without the LS beam, the setup is a Bell-Bloom type synchronously pumped magnetometer [5]. Pump beam creates polarization P_{pmp} along X, which precesses around $\vec{B}_0 \parallel$ Z (Figure 2.7). When the LS beam is introduced and tuned close to an optical transition, it creates polarization P_{LS} along $\vec{k}_{LS} \parallel$ Z parallel with the leading field $\vec{B}_0$. In turn, the light shift induced by the pump acts as a fictitious magnetic field orthogonal to P_{LS} and modulated at the Larmor frequency. This produces an optically-pumped rf-driven magnetometer setup [1], except that the modulated radio-frequency magnetic field $\vec{B_{rf}}$ is replaced by a power-modulated light beam.

Section 3.1 describes an application of this effect, where we utilize a pulsed LS beam to build an LS-driven magnetometer [63]. In this work we demonstrate that both traditional rf-driven magnetometer and the LS-driven magnetometer can achieve comparable signal magnitudes, same shot noise sensitivity and similar measured sensitivity. We also show that the LS-driven magnetometer can take advantage of the light narrowing effect [61], similarly to the rf-driven magnetometer. This kind of magnetometer is advantageous in a situation where precise magnetic field monitoring is required, but introducing additional magnetic fields is highly undesirable, such as nEDM [10].

2.4 Diameter dependence

The text presented in this section is part of a publication that has been published as Ref. [64].

Introduction

Light shifts in alkali atoms have been researched since 1960s [50, 65], however the effect of laser-induced vector light shifts (VLS) in coated cells has been little explored in the literature. The works considering light-shift effects primarily focus either on transitions relevant for atomic clocks [65–72], magnetometers using buffer-gas cells [55–60], or light shifts induced by broad-spectrum alkali metal lamps [50, 51, 65, 73, 74].

In this paper, we discuss the role of VLS in an optical magnetometer exploiting a paraffin-coated alkali-metal vapor cell [75–82]. Unlike uncoated cells, paraffin-coated cells enable the atoms to undergo a number of wall collisions (up to 10^6 [83]) without depolarization. In this way, thermal atoms sample the entire cell volume during their spin relaxation time and hence become sensitive to average, rather than local magnetic field [84]. In this work we demonstrate that the same reasoning can be applied to the VLS in paraffin-coated cells, making it, under realistic assumptions, a function of the total light power averaged over the cell volume, rather than the local intensity.

The experiment consists of a series of VLS measurements as a function of beam diameter and optical frequency in a synchronously pumped (Bell-Bloom [1, 36]) orientation-based Cs magnetometer. The magnetometer utilizes the resonant response of the atoms to modulated light that occurs when the modulation frequency ω_m matches the atoms' Larmor frequency ω_L. The magnetic field can then be extracted by measuring the center frequency of the Lorentzian shaped magnetic resonance (MR). We investigate the dependence of the light shift, manifesting as a frequency change of the MR, on the beam diameter for a fixed optical power and show that with negligible optical pumping the shift is independent of the size of the laser beam (apart from small systematic contributions).

Model

To gain understanding of the processes involved in the light-shift averaging, we consider a concentric cylindrical cell and a laser beam with radii R and r, respectively. The optical frequency of the light-shift laser is far-detuned from the relevant atomic transitions compared to the Doppler width, and the beam-intensity profile is for simplicity assumed flat (top hat). In the presence of a magnetic field, the atomic spins precess with the Larmor frequency ω_L. Each individual atom interacting with the light-shift beam acquires a phase advance or retardation ϕ in its Larmor precession proportional to the change in the Larmor frequency due to the vector light shift in the beam $\delta\nu$ and the time t spent in it during the spin coherence time T_2 (T_2 is here the relaxation time for given experimental conditions that is equal to the inverse width of the MR line).

In the proximity of an optical transition, the change in the Larmor frequency by a sufficiently far detuned, circularly polarized laser beam is given by

$$\delta\nu \approx \beta \frac{I}{\Delta_{LS}}, \tag{2.1}$$

where Δ_{LS} is the frequency detuning of the light-shift (LS) beam with respect to the center of the optical transition (in our experimental setup, this is the center of the Doppler-broadened $F_g = 4 \rightarrow F_e = 3, 4$ transition group of the $^{133}\mathrm{Cs}\,\mathrm{D}_1$ line), I is the intensity of the LS beam, and β is a proportionality constant that can be calculated with second-order perturbation theory, taking all the relevant transitions and magnetic sub-levels into account (see, for example, [54]).

The scaling of the light-induced MR center frequency shift can be understood as follows: assuming that the probability to find an atom in any part of the cell volume is the same, t is proportional to r^2/R^2, while the beam intensity I scales as $1/r^2$. Since the average phase change acquired by an atom is $\phi \propto I \cdot t$, it does not depend on r. This average phase increment acquired during T_2 can be translated into the average frequency shift of the MR $\delta\nu_{LS}$ by dividing it by the coherence time T_2 of the Larmor precession. Since ϕ is independent of the beam area, $\delta\nu_{LS}$ stays constant for a given light power. Note also that $\delta\nu_{LS}$ is independent of T_2 under the present approximations.

In addition to shifting the MR center frequency, due to the stochastic nature of the interaction of atoms with the light beam, there is also a contribution to the MR linewidth. To estimate this contribution, we consider the different stochastic processes involved and their probability density functions. The number of an atom's transits across the LS beam during a relaxation time follows a Poissonian distribution with mean $n \propto r/R$. At the same time, the amount of phase advance or retardation the atom picks up per pass is normally distributed with mean ϕ_1 and variance $\delta\phi_1^2$. The total shift for the mean number of passes is given by $\phi = n\,\phi_1$ with a variance of $n\,\delta\phi_1^2$. For $\sqrt{n}\,\delta\phi_1 < n\,|\phi_1| \ll 1$ it can be shown (see, Ref. [48]) that this kind of Larmor precession phase diffusion leads to the previously discussed shift but also to a broadening of the MR. The width increase is due to the uncertainty in the number of interactions per atom as well as the variance $\delta\phi_1^2$ of the LS effect for a single interaction. If the width of the MR stems from a combination of different phase-diffusion processes the contributions add in quadrature.

Experimental setup

The foundation of the experimental setup (Fig. 2.8a) is a synchronously pumped Bell-Bloom type magnetometer with an additional laser beam (LS beam) that induces the light shift. The magnetic shielding, the sensor cell, and the leading field $\vec{B}_0$ source are described in Ref. [17]. Here, we only recapitulate the main experimental parameters. The paraffin-coated ^{133}Cs cell has a cylindrical shape and measures 50 mm in length and in diameter. Its longitudinal spin relaxation time is 0.7 s. The leading field $\vec{B}_0$ has a magnitude of 489 nT, ($\omega_L = 2\pi \cdot 1710.0\,\mathrm{Hz}$ for the Cs $F_g = 4$ manifold), and is parallel to ŷ. The probe light is emitted from a distributed feedback laser (DFB) and tuned to the caesium D_2 line (852 nm) with a power of 9.8 μW. The light is linearly polarized ($\vec{E} \| \hat{y}$) and propagates orthogonally to $\vec{B}_0 \parallel \hat{y}$ (wave vector $\vec{k}_{pr} \parallel \hat{x}$). Its optical frequency is stabilized using a dichroic atomic vapor laser lock (DAVLL, not shown in Fig. 2.8a) [85, 86] close to the $F_g = 4 \rightarrow F_e = 3, 4, 5$ transition manifold. The detuning and intensity of the probe beam are optimized for the largest signal with minimal power broadening. The circularly polarized pump light (852 nm DFB, 16.8 μW time averaged) is injected into the cell orthogonally to $\vec{B}_0$ ($\vec{k}_{pmp} \parallel \hat{z}$). Its power is pulsed by an AOM at the Larmor frequency with a 3.4% duty cycle. The beam is routed by a single-mode polarizing fiber (Fibercore HB830Z) with cleanup polarizers at the output. The pump frequency is locked on resonance with the $F_g = 3 \rightarrow F_e = 4$ transition by an additional DAVLL (not shown in Fig. 2.8a). This produces atomic polarization (orientation) in the $F = 4$ manifold by optically pumping while simultaneously depopulating the $F_g = 3$ manifold. The large detuning from the probed $F_g = 4$ manifold also minimizes power broadening and light shifts caused by the pump [62]. The LS beam is circularly polarized (895 nm DFB, 5.5 μW time averaged) and propagates parallel to $\vec{B}_0$ so that the vector light shift adds linearly to the Zeeman shift due to $\vec{B}_0$. The beam power is actively stabilized with an AOM in a feedback loop. To change the size of the beam and ensure a homogeneous intensity distribution, the initially Gaussian beam is expanded by a telescope to a large diameter and the central part is picked out by a computer controlled iris with variable aperture. The image of the iris is then formed by a lens system inside the cell and onto a beam profiler (Coherent LaserCam RS-170). For each beam size an image is taken and saved for later analysis. The pick-off for power stabilization and beam profiling is provided by an uncoated wedged beam splitter positioned after the imaging optics outside of the shields just followed by polarizing elements in front of the cell. The optical frequency of the LS beam is actively controlled by a wavemeter (Ångstrom/HighFinesse WS-7) in a feedback loop.

As the probe light propagates through the polarized atomic vapor, it experiences magneto-optical rotation [87] which causes a modulation of the probe's polarization direction at the Larmor frequency. The optical signal is detected with a balanced polarimeter connected to a transimpedance amplifier and demodulated with a lock-in amplifier (LIA) at the modulation frequency.

A signal generator (BNC 645) controls the pump pulsing frequency and serves as a local oscillator (LO) for the LIA (SR 830). The phase of the LIA is adjusted to produce absorptive and dispersive signals in the X and Y LIA channels respectively, when the pump-pulse repetition frequency is scanned across the MR. The X and Y signals are captured with a data acquisition system (NI DAQ 6353) and analyzed with a computer (PC) that controls the experiment. Slow drifts in the the MR center frequency and width pose a challenge for our measurement, as they cause all data points to have a slightly different scaling between the measured signal and the actual light shift. To mitigate this, we simultaneously harmonically modulate the LS beam power and the pump pulsing frequency (in the vicinity of the resonance) at different frequencies. Both signals cause a linear response in the dispersive channel of the lock-in. The latter modulation enables us to continuously monitor the dispersive slope of the MR throughout the experiment since the modulation amplitude is known. We effectively compare the modulation due to the LS beam with a modulation of known amplitude. This way the response of the cell is calibrated for each data point. The modulation frequencies of the LS beam power ($\omega_M = 2\pi{\cdot}0.8\,\mathrm{Hz}$) and the pump pulse frequency ($\omega_C = 2\pi{\cdot}0.5\,\mathrm{Hz}$) are chosen to be smaller than the MR linewidth (3.2 Hz corresponding to $T_2 \approx 100$ ms) to avoid low-pass filtering.

For each data point, we record a 40 s sample of X and Y channels of the LIA. An example can be seen in Fig. 2.8b. The signals are Fourier transformed (Fig. 2.8c) and processed to extract the MR linewidth, amplitude and RMS Larmor frequency deviation caused by the LS beam. Each sample has an integer number of periods of both LS and LO modulations to minimize spectral leakage.

Results

To see whether the VLS is averaged by the atoms in a paraffin-coated cell, we measure the dependence of the MR center shift as a function of the LS beam area for a given total power ($5.5\,\mu$W). The average LS intensity is adjusted to keep the total power constant as the beam diameter changes. The smallest beam diameter was given by the maximum available LS beam power and the biggest beam diameter by the minimum value the power could reliably stabilized to with the AOM. The measurement procedure is repeated for different optical frequencies of the LS beam, and each data set is fitted with a linear function. The data and the corresponding fits are displayed in Fig. 2.9.

The average light shifts were calculated as an average Larmor frequency change over the data points with different diameters for a given detuning. They are presented in Fig. 2.10. As shown in Eq. (2.1), the average light shift scales as $1/\Delta_{LS}$ for large frequency detunings. This dependence is clearly visible in Fig. 2.10.

The outlier point appearing at +9 GHz in Figs. 2.10 and 2.11 corresponds to the $F_g = 3 \to F_e = 3, 4$ transitions. This deviation from the theoretical scaling of the VLS (Fig. 2.10) and the stronger dependence on the beam size (Fig. 2.11) is a result of optical pumping by the LS beam.

At this frequency, the LS beam acts as an additional pump, producing orientation in the $F_g = 4$ manifold with effects on the MR width and amplitude. The effect can also be seen at the origin of Fig. 2.11 corresponding to optical pumping on the $F_g = 4 \to F_e = 3, 4$ transition manifold. Additionally, the absorption in the vapor causes an effective reduction of the LS beam intensity. However, since these are on-resonant effects, a detailed analysis is beyond the scope of this paper.

Throughout the experiment the maximum MR center frequency shift was below 100 mHz (30 pT), which is well within the MR resonance width. Signal-to-noise ratio for each data point in Fig. 2.10 was on average 140 and for large detunings the measurement error was below 1 fT.

The dependence of the VLS on the beam diameter for each optical frequency is presented in Fig. 2.11. The plot is the result of normalizing the light-shift change per unit area change by the average light shift at each optical frequency (see caption to Fig. 2.11) A change of the beam area (and therefore of the intensity) by a factor of eight results in an average light shift change on the order of 3%. A likely explanation of this small variation is a systematic effect related to the power stabilization of the LS beam; there seems to be a small diameter dependent difference in power between the cell and the stabilization photodiode. This can have multiple reasons, e.g., clipping of the beam or an angle dependent sensitivity of the photodiode.

In addition to the average change, a sinusoidal variation with the optical frequency detuning is visible. This oscillation pattern appears to be the result of an etaloning effect in the vapor-cell windows. The modulation period of 60 GHz corresponds to a glass-resonator length of 1.7 mm, which is consistent with the thickness of the cell windows. To further verify this, we measured the LS beam power transmission as a function of beam diameter for different LS beam frequencies, which revealed the same pattern.

In a separate set of similar experiments (not discussed here) we tried to observe the LS-beam-induced broadening of the MR width. Even with much longer averaging no broadening was detected. This is not surprising however, given that the values of $\delta\nu_{LS}$ are much smaller than the MR width. We expect the additional contribution due to $\delta\nu_{LS}$ to be on the order of $\delta\nu_{LS}/\sqrt{n}$, which should be added to the MR width in quadrature (Sec. II). The resulting maximum increase in MR width is less than 10 ppm, which was experimentally inaccessible.

Summary

In conclusion, we investigated how the vector light shift exerted by a circularly polarized laser beam on atoms in a paraffin-coated cell depends on the beam area. Theoretical estimates suggest that for a given beam power the overall light shift should be independent of the beam area, as long as the thermal atoms adequately sample the entire cell volume during the spin relaxation time. We experimentally verified that the vector light shift in a coated cell depends nearly exclusively on the total beam power and not on the beam area. With a factor of eight change in the beam area, the light shift changes by less than 3%. The residual dependence on the area can be explained by frequency and diameter dependent transmission of the LS beam in the optical elements between the atoms and the intensity-stabilization photodiode. The magnetic resonance broadening due to the variance in the number of passes through the light-shift beam or due to the variance in the time spent in the beam per pass was below the experimental sensitivity. These results are important for modern magnetic

sensors that make use of auxiliary fictitious fields [17] and can be extended to other spatially averaged quantities in cells with long coherence times.

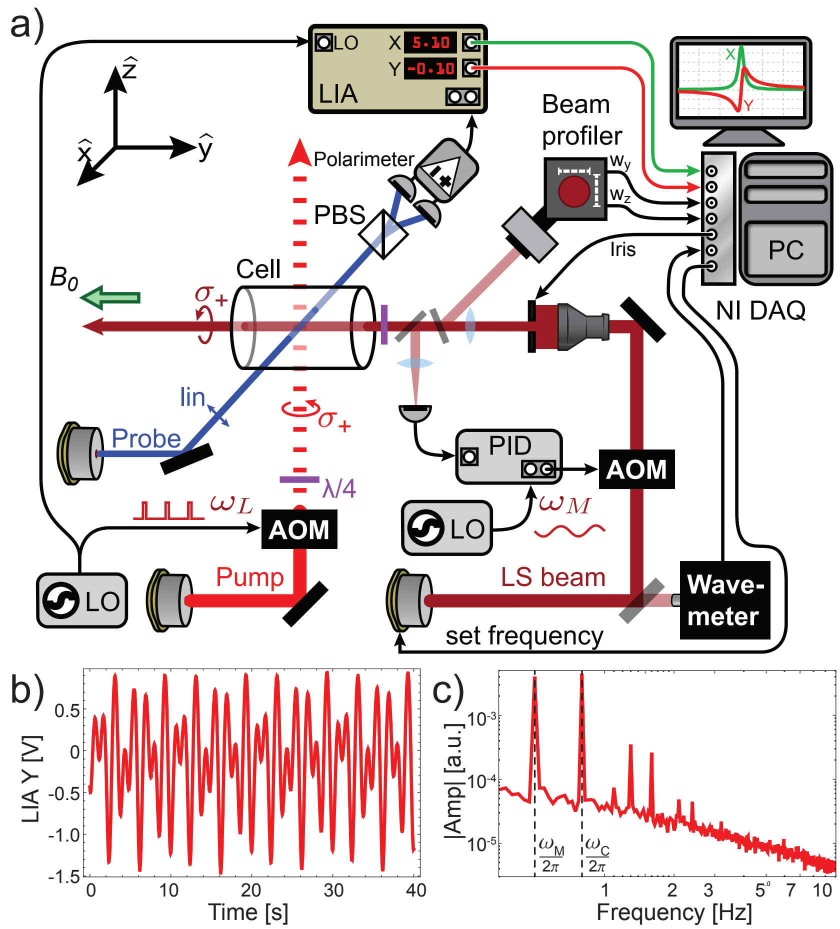

Figure 2.8: a) The experimental setup. The amplitude-modulated, circularly polarized pump beam propagates along $\hat{z}$ (orthogonally to $\vec{B}_0 \parallel \hat{y}$). A local oscillator (LO) pulses the pump intensity via an acousto-optical modulator (AOM) and serves as a reference for a lock-in amplifier (LIA), whose analog output is recorded with a data acquisition card (DAQ) and stored on a computer (PC). After transmitting through the cell, the linearly polarized probe beam is analyzed with a balanced polarimeter, consisting of a polarizing beam splitter (PBS) and two photodiodes. The circularly polarized light-shift beam (LS beam) propagates along $\vec{B}_0$. Its diameter is varied with a computer controlled, motorized iris while its time-averaged power is kept constant with an AOM in a feedback loop. An image of the iris is formed inside the cell and on the beam profiler using a lens system. The optical frequency of the LS beam is measured with a wavemeter and controlled by the PC. For noise reduction, we perform synchronous detection of the VLS signal while harmonically modulating the LS beam power at ω_M. b) shows the recorded time series for the LIA Y output for a single light shift measurement with the simultaneous modulation of the LO frequency and the LS power. c) The FFT of the signal in b) shows the calibration peak at $\omega_C/2\pi$ and the LS amplitude at $\omega_M/2\pi$.

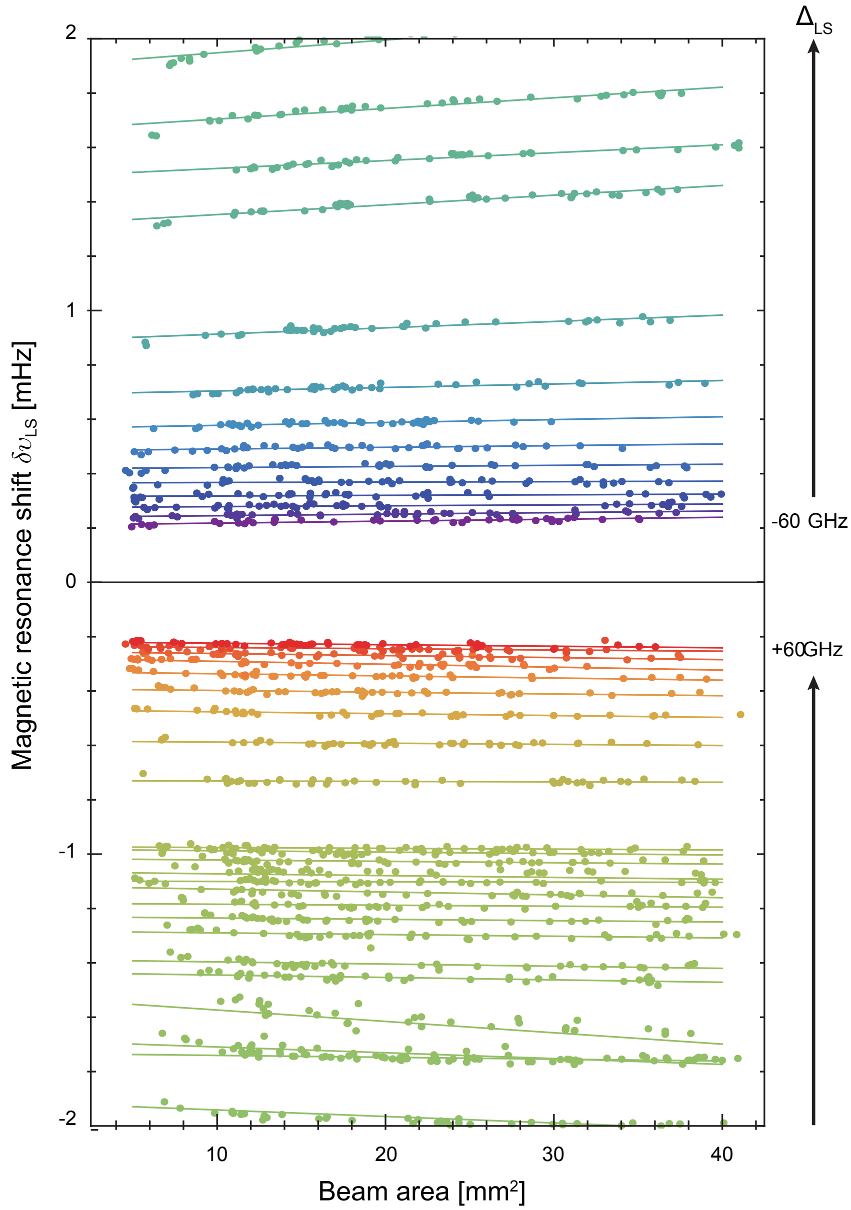

Figure 2.9: Change of the magnetic resonance center frequency as a function of the light-shift beam area for different LS beam detunings and a constant beam power. The complete data include detunings from -60 GHz to $+60$ GHz with respect to the ^{133}Cs D$_1$ $F_g = 4$ transitions. Just a fraction of the data is displayed here for better visibility of the individual sets. While the beam area x, and therefore the beam intensity, is modified by an order of magnitude, the MR center frequency changes are on average 3% and are of technical origin as explained in the text. Different colors represent distinct optical frequencies of the LS beam, the detuning is indicated by the arrows on the right. The data points are represented by circles, and the lines are linear fits $\delta\nu_{LS}(x) = a_{LS} + b_{LS}(x - \langle x \rangle)$ to the datasets. $\langle x \rangle$ is the mean area of the fitted set. The fit parameters are average light shift a_{LS} and light shift change per unit area change b_{LS}.

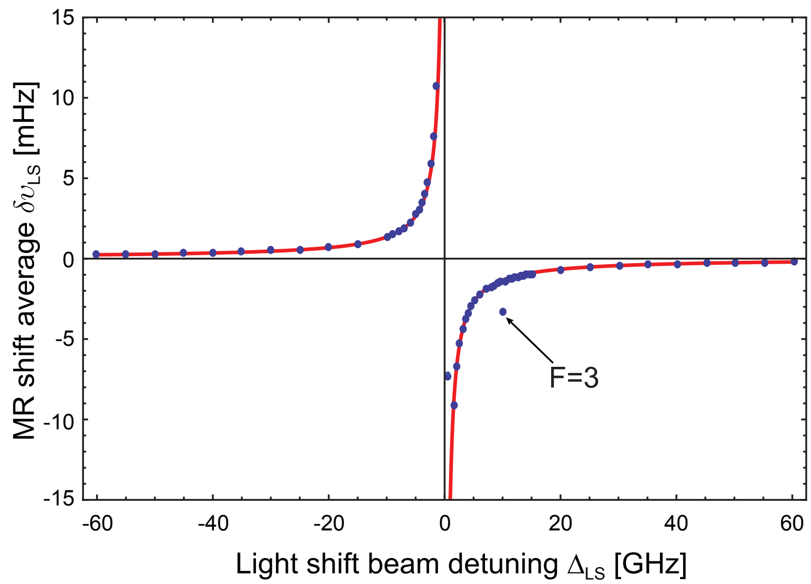

Figure 2.10: Average vector light shift a_{LS} dependence on the optical frequency as derived from the fits to the data displayed in Fig. 2.9. The error bars are hidden within the points since the average ratio between data value and error is 140. The red curve shows a fit to the data with $\propto 1/\Delta_{LS}$.

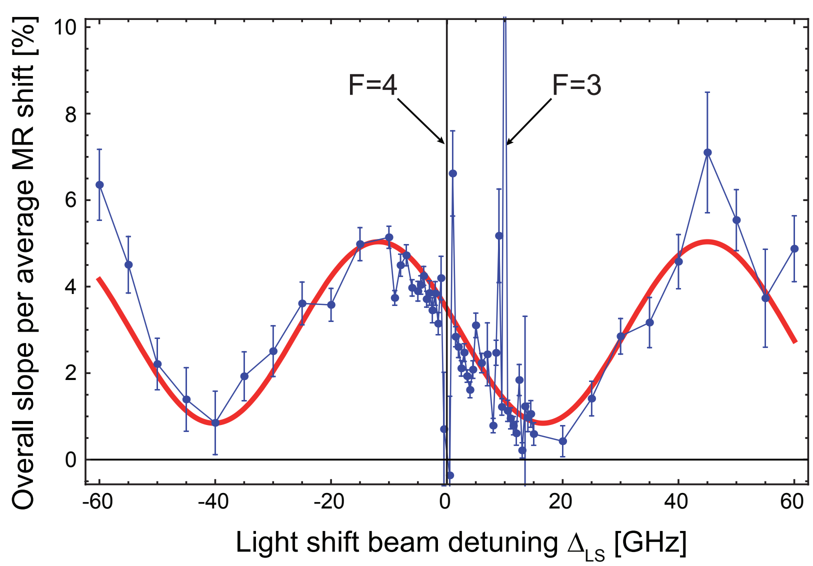

Figure 2.11: Light-shift change per unit area b_{LS} divided by the average light-shift a_{LS} (b_{LS}/a_{LS} from Fig. 2.9) as a function of the LS beam detuning. The data were rescaled to express the change of the measured light shift over each dataset to its mean value in percent. The red line is a sinusoidal fit revealing an etalon effect potentially in the cell wall.

Chapter 3

Vector light shift applications

3.1 Light-shift magnetometer

Most of the text presented in this section is part of a paper that has been published as Ref. [63].

Motivation

The general working principle of atomic magnetometers relies on optically polarizing the atoms along the leading magnetic field $\vec{B}_0$ and then driving transitions between magnetic sublevels via a resonant radiofrequency magnetic field $\vec{B}_{\mathrm{rf}}$. Arrays of rf-driven magnetometers are often employed when monitoring the magnetic field in an area or volume is needed. This includes medical applications such as human heart or brain activity mapping [88, 89], or in fundamental-physics experiments e.g., those searching for a permanent electric dipole moment of the neutron (nEDM) [90,91]. In these applications, the rf technique has important limitations. The oscillating magnetic field contaminates the monitored environment which is detrimental for precise measurements. Additionally, crosstalk between adjacent sensors places a limit on spatial resolution of a sensor array.

The goal of this experiment is to demonstrate a way to overcome these limitations by replacing the radio frequency coils with intensity-modulated laser beams. All-optical rf-driven magnetometry could also be useful in remote magnetometry applications, where real magnetic fields cannot be directly applied to the atomic sample [77, 92].

Experimental setup

The experimental setup is shown in Fig. 3.1. An evacuated, paraffin-coated ^{133}Cs cell is placed within a four-layer μ-metal magnetic shield with a total attenuation factor of $\sim 10^{-6}$ [36]. The cell is a 50 mm long cylinder with a diameter of 50 mm. Within the cell, the longitudinal spin relaxation time of the ^{133}Cs vapor is measured to be $T_1 = 0.7\,\mathrm{s}$. (here T_1 is the longer relaxation time in the bi-exponential decay as discussed in [93]).

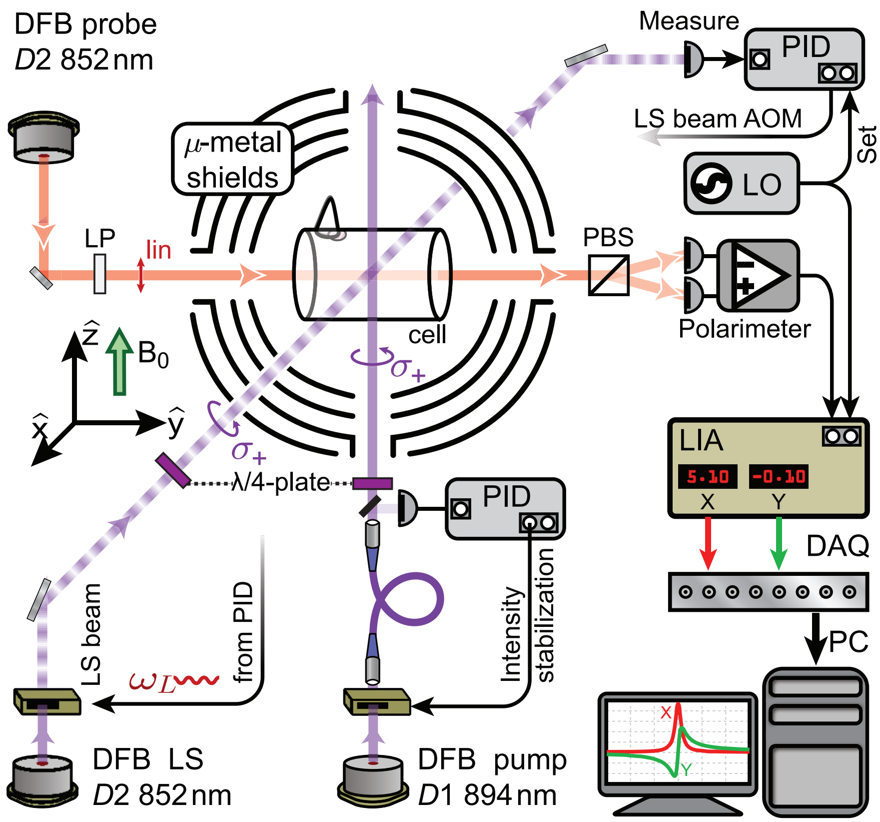

Figure 3.1: Experimental setup. The vapor cell is housed in a four-layer μ-metal shield. An unmodulated intensity-stabilized pump beam is circularly polarized and propagates along the leading field in the $\hat{z}$ direction. Spin precession is induced either by an oscillating magnetic field $\vec{B}_{\rm rf}\|\hat{x}$ or by the modulated light-shift (LS) beam with $\hat{k}_{\rm LS}\|\hat{x}$. A local oscillator (LO) provides the control signal for either the rf coil or the LS acousto-optic modulator (AOM), corresponding to the method used to induce the spin precession. A linear polarizer (LP) ensures a linearly polarized probe with $\hat{k}_{\rm pr}\|\hat{y}$. The beam experiences rotation of its polarization plane, which is detected by a polarimeter, consisting of a polarizing beam splitter (PBS) and two photodiodes. The precession signal is demodulated by a lock-in amplifier (LIA) with the LO as a reference, and digitized by the PC via a data acquisition board (DAQ). All light sources used are distributed feedback laser (DFB).

Coils inside the shields provide the leading field $\vec{B}_0$, gradient compensation along the $\hat{z}$ direction, and an oscillating $\vec{B}_{\rm rf}$ field in the conventional rf-driven magnetometer setup. The leading-field and gradient compensation coils are powered by separate channels of a custom current source (Magnicon GmbH) that exhibits a stability of $\sim 10^{-7}$ over 100 seconds. The current source is placed inside an insulated temperature stabilized container, which maintains a constant temperature within ± 10 mK and further increases $\vec{B}_0$ stability. The leading field $\vec{B}_0$ is kept constant at ~ 480 nT, which corresponds to Larmor frequency of 1690 Hz. Unused magnetic coils are terminated to exclude the possibility of them picking up rf noise and transferring it inside the magnetic shields. The sensor cell is cooled to 17.5 °C by a flow of cold air directed inside of the magnetic shields. The interior temperature is passively stabilized by equilibrating the heat flows from the cold air gun (Vortek 610) and the environment. Passively stabilized sensor exhibits temperature drifts of several degrees on a daytime scale, which is much longer than the measurement time. Although the interior of the shields is equipped with an AC heater, it was found to increase the magnetometer noise floor and disabled. To monitor the cell temperature, a non-magnetic T-type thermocouple (Omega TT-T-24S-SLE) is attached to the cell mount inside the shields.

The pump beam (894 nm DFB laser, 75.5 μW) is launched parallel to $\vec{B}_0$ ($\hat{\mathrm{k}}_{\mathrm{pu}} \| \hat{\mathrm{z}}$) by a polarizing fiber (Fibercore HB830Z). The light power at the fiber output is stabilized by an AOM in a feedback loop, thus minimizing the fluctuations of the light shift induced by the pump beam. A zero-order quarter-wave plate before the magnetic shield ensures circularly polarized light. The pump frequency is locked to the D_1 $F = 3 \to F' = 4$ transition by a dichroic atomic vapor laser lock (DAVLL) [85,86,94]. Since we observe a magnetic resonance (MR) within the $F = 4$ manifold, the probe is tuned to the D_2 $F = 4 \to F' = 5$ transition, stabilized by a separate DAVLL. This tuning provides an optimum between having the largest optical rotation and not too much broadening (less than T_2). The pump polarizes the $F = 4$ manifold by depopulating the $F = 3$ manifold. This detuning of the pump has the benefit that it causes a smaller light shift in the probed $F = 4$ manifold while producing minimal light shift and magnetic resonance broadening [62]. Moreover, we can see narrowing ($\sim 10\%$) of the spin-exchange-limited resonance line [95, 96] due to the high polarization in the vapor.

The light-shift beam (LS beam) is $\sigma+$ polarized and propagates orthogonally to $\vec{B}_0$ with $\hat{\mathrm{k}}_{\mathrm{LS}} \| \hat{\mathrm{x}}$ (852 nm DFB laser, 1.9 mW time-averaged power equivalent to a fictitious magnetic field with 0.19 nT amplitude). The laser power is modulated by an AOM in order to provide a time-varying light shift. In order to mitigate non-linearities in the AOM driver response and ensure the LS beam power is harmonically modulated, we stabilize the transmitted power with a PID controller (SRS SIM960) and feed a harmonic control signal to the set-point PID input. The optical frequency of LS beam is red-detuned from D_2 $F = 4 \to F' = 5$ by 50 GHz and locked via a wavemeter (Ångstrom/HighFinesse WS-7). Measured MR broadening caused by the LS beam was below 50 mHz at this optical frequency.

The probe beam (852 nm DFB laser, 16.4 μW) propagates along $\hat{\mathrm{y}}$ and is linearly polarized in a plane orthogonal to $\vec{B}_0$ to minimize the probe-induced static atomic alignment (quadrupole magnetic moment [87]). Optical frequency of the probe is locked at around 0.7 GHz red-detuned from D_2 $F = 4 \to F' = 5$ transition, minimizing the power broadening while still having appreciable (20 mrad) polarization rotation. The Larmor precession is detected by a differential photoamplifier (Appendix A) and demodulated by a lock-in amplifier (SR830) with the local oscillator as a reference (Berkeley Nucleonics Corp. BNC645). The polarimeter's electronic noise corresponds to shot noise of 0.45 μW of light (0.17 fT/$\sqrt{\mathrm{Hz}}$ equivalent magnetic field noise). The choice of the lock-in amplifier phase ensures the Y

(X) signal is a fully dispersive (absorptive) Lorentzian (Figure 3.2). Both quadratures are acquired either via GPIB in case of the driven-oscillation scan, or with a NI DAQ device (USB-6353), when the driving frequency is modulated. The laser beams do not overlap within the cell, and their waist sizes ($< 1\,\mathrm{mm}$) are small compared to the cell diameter (50 mm). Since the atoms traverse the cell in a time shorter than the precession period, they motionally average the magnetic fields (real and fictitious) within the cell, as well as the intensity of the pump and probe beams [84]. For this reason, the observed light shifts only depend upon the power of the beams and not their spatial intensity profiles.

Results

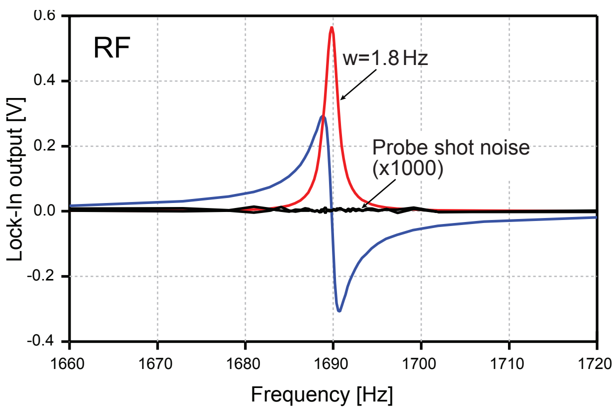

Figure 3.2: Driven-oscillation scans. Left: the quadrature outputs of the lock-in amplifier for rf-driven magnetometer. The blue and red curves are the dispersive (Y) and the absorptive (X) signals. In black, magnified by a factor of 1000, is the same scan with the pump beam blocked. Right: the same resonance for the LS mode. The curve exhibits the same width as the coil-driven magnetometer for the same amplitude. The small residual resonance seen in the lower plot is due to synchronous pumping by the far-detuned LS beam.

In this section we compare sensitivities of the setup operating in two distinct modes. First mode is an rf-driven magnetometer (RF), where the spin precession is induced by a real oscillating magnetic field $\vec{B}_{\mathrm{rf}} \| \hat{\mathrm{x}}$. Second mode is a light-shift-driven magnetometer (LS), where the spin precession is induced by a fictitious oscillating magnetic field created by an intensity-modulated laser beam. We compare the projected sensitivities of the two modes, as well as the linear spectral density (LSD) of the magnetometer signals (Figure 3.3), and the LO frequency step responses (Figure 3.4).

We obtain the MR signals (Fig. 3.2) by stepping the LO frequency around the MR while acquiring the X and Y lock-in outputs. The signals are fit to a Lorenzian in order to obtain the resonance amplitude and width. The shot noise is measured by repeating the procedure with the pump beam blocked. While in the RF setup the signal is dominated by the probe laser shot noise (Figure 3.2 left), in the LS setup the intensity-modulated light-shift beam induces a small amount of polarization (Figure 3.2 right). This establishes a Bell-Bloom type of synchronous pumping [5] resonance due to residual photon scattering of the intensity-modulated LS beam. The additional resonance introduces a constant distortion, rather than noise, to the magnetometer signal. Comparing the slope of the dispersive signal (blue) with the RMS photon shot noise yields a signal-to-noise of 1.2×10^5, equivalent to the projected sensitivity of $1.7\,\mathrm{fT}/\sqrt{\mathrm{Hz}}$ for both RF and LS setups.

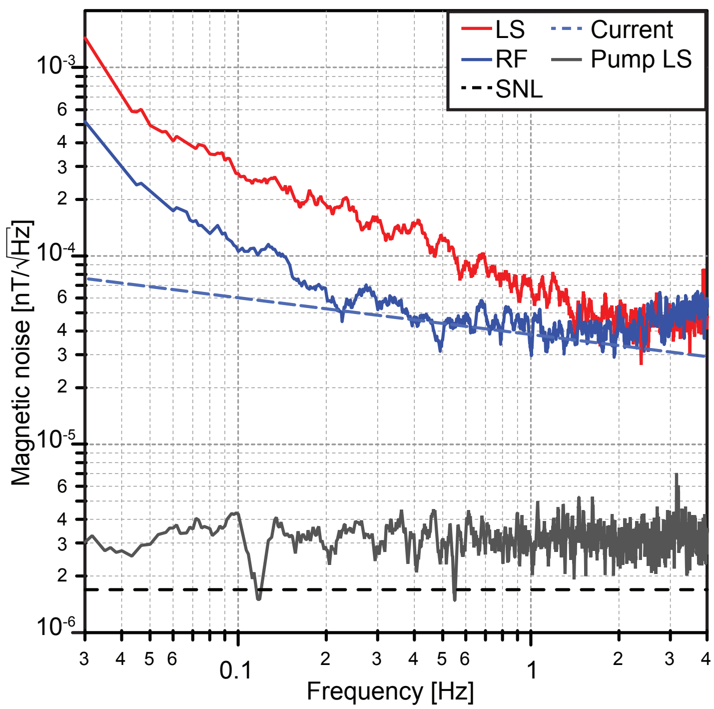

Figure 3.3: Linear spectral density plot for the RF (dark blue) and LS (red) modes. The black dashed line represents the shot noise limit ($1.7\,\mathrm{fT}/\sqrt{\mathrm{Hz}}$). The gray trace is the noise induced by the varying light shift caused by pump laser power fluctuations ($3.3\,\mathrm{fT}/\sqrt{\mathrm{Hz}}$). The blue dashed line is the magnetic field noise according to the specifications of the current source creating the leading field.

We note here that the synchronous pumping resonance observed in the LS configuration can also be used to measure the magnetic field. Optimization in this pumping mode results in projected sensitivity of $1.9\,\mathrm{fT}/\sqrt{\mathrm{Hz}}$ with $43\,\mu$W average pump power and a 3% duty cycle. For best performance in Bell-Bloom mode, the LS beam is tuned to address the D_2 $F = 3$ manifold. However, the presence of cycling transitions in the synchronous pumping scheme causes considerable MR line broadening (2.3 Hz) compared to the LS magnetometer scheme (1.8 Hz) which takes advantage of light narrowing. The difference could be even more drastic if an alkene cell with ∼77 s relaxation time is utilized [83]. For clarity, we focus in the analysis on the two (fictitious or real magnetic field) rf-driven magnetometers.

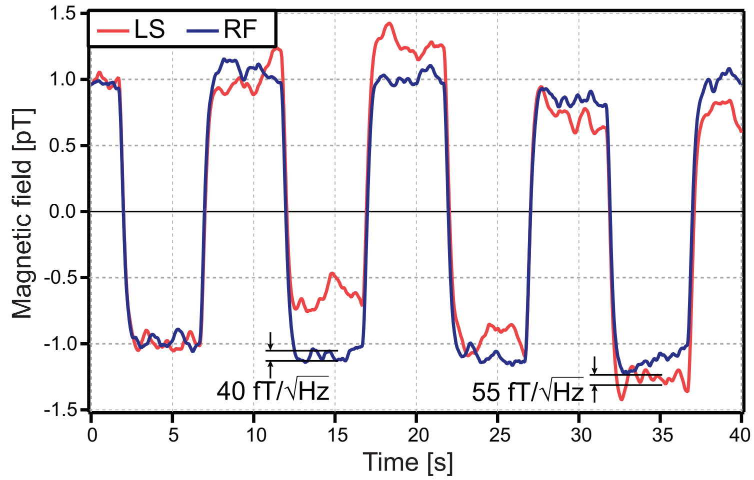

Figure 3.4: Response of both magnetometers to steps in the LO frequency. The frequency generator was stepped by $\pm 3.5\,\mathrm{mHz}$ around the center of the magnetic resonance every 10 s. The data were acquired with a noise bandwidth of 0.8 Hz due to the selected time constant of the lock-in amplifier.

To measure the signal spectrum density (Figure 3.3), we tune the frequency generator to the center of the MR and record the dispersive Y output of the lock-in. It depends linearly on the applied driving frequency, or equivalently deviation of the leading magnetic field. We record the signal over time, convert it to an equivalent field change and perform a Fourier transform of the result. Without implementing additional techniques to increase the bandwidth of a magnetometer, e.g. exploitation of spin damping [97] or quantum non-demolition measurements [98], the bandwidth is constrained by the the time constants of the relaxation processes within the sensor cell. To correct for this, we mapped the frequency response of the cell (Appendix B) and scaled the magnetic field noise accordingly. Both magnetometers exhibit a minimum noise floor of $40\,\mathrm{fT}/\sqrt{\mathrm{Hz}}$ at $\sim 2\,\mathrm{Hz}$, where the contribution of the laboratory magnetic noise is minimal.

For the field step response measurement, we modulated the LO frequency around the Larmor resonance by $\pm 3.5\,\mathrm{mHz}$, equivalent to a leading field modulation by $\pm 1\,\mathrm{pT}$. We observed the dispersive Y output of the lock-in and compared the step size to the RMS noise to estimate the S/N ratio. The average RMS noise on the step was $40\,\mathrm{fT}/\sqrt{\mathrm{Hz}}$ for the RF mode, in agreement with the LSD measurement. For the LS mode the RMS noise was slightly larger ($55\,\mathrm{fT}/\sqrt{\mathrm{Hz}}$) due to the increased noise level at frequencies around 0.2 Hz.

Noise sources

In this section we summarize the noise sources in three magnetometer configurations – LS mode, RF mode, and synchronously pumped. Any factor that changes the effective light shift of laser beams (such as frequency and power fluctuations) introduces an effective magnetic field noise. Technical fluctuations in the current lead to an instability of $\vec{B}_0$, to which another contribution is the environment noise leaking through the $\mu-$metal shields.

First, let us consider the noise contributed by the probe beam. A linearly polarized probe beam can be represented as a superposition of two circularly polarized components with equal intensity. Although the fictitious magnetic field produced by the probe is zero on average, the number of photons in each circularly polarized components fluctuates due to the photon shot noise. Experimentally measured photon shot noise of the probe beam (16.4 μW, 852 nm, $F_g = 4 \rightarrow F_e = 5$; + 200 MHz detuning) was 1.7 fT/$\sqrt{\mathrm{Hz}}$. In addition, probe power and frequency fluctuations affect the average light shift due to residual power imbalance between the circularly polarization components of the probe. Maximum imbalance due to the cell birefringence and finite polarizer extinction ratio is estimated to be $< 1.6 \times 10^{-4}\,\mu$W. The effective light shift for circularly polarized beam is ~ 8.6 pT/ μW (30 mHz/ μW) at the probe optical frequency, and the expected maximum light shift due to the polarization imbalance is 14 fT. With probe power fluctuations estimated to be $< 1\%$ of the total power, the noise due to the power fluctuations is negligible compared to the shot noise. Probe optical frequency fluctuations were within 1 MHz, as estimated from the DAVLL signal. The MR center frequency fluctuations due to the probe optical frequency changes is 0.1 mHz/MHz/ μW (Section 2.2), or 5×10^{-3} fT maximum equivalent magnetic field drift. Thus, the shot noise is the dominant noise contribution originating from the probe laser.

Magnetometer sensitivity to the pump power fluctuations for RF and LS modes was measured to be $\sim$ 500 fT/ μW (894 nm, $\sigma+$, 75.5 μW, D_1, $F_g = 3 \rightarrow F_e = 4$). With the measured power stability of $\sim 0.1\,\mu$W (0.1%) the noise induced by the pump power fluctuations is ~ 38 fT, which is lower than the technical noise of the magnetometer in both modes. The expected sensitivity to the optical frequency fluctuations is 3.7 fT/ μW/100 MHz, while the short-term optical frequency drift is estimated to be < 10 MHz from the wavemeter error signal. The noise due to the pump frequency fluctuations can be then estimated as ~ 28 fT, which is the same order of magnitude as the noise induced by the power fluctuations. The noise contribution from the pump light might be further attenuated due to most of the atoms in the sensor cell being in the stretched state and thus not interacting with the pump beam.

In synchronously pumped configuration the pump beam (43 μW, D_2, $F_g = 3$) induces a time averaged 0.5 pT/ μW MR center shift, with the total of 0.22 nT. When the pump beam is perfectly orthogonal to $\vec{B}_0$, this shift is attenuated by a geometric factor of $B/B_0 \sim 0.5 \times 10^{-3}$, resulting in the shift of 0.25 fT/ μW. When the pump power is not stabilized, the power noise density at $f < 1$ Hz is measured to be 0.6 μW/$\sqrt{\mathrm{Hz}}$, which leads to the noise contribution of 0.15 fT/$\sqrt{\mathrm{Hz}}$. If the pump and $\vec{B}_0$ are slightly non-orthogonal, the noise contribution would be proportional to the misalignment angle, and equal 6 fT/$\sqrt{\mathrm{Hz}}$ at $f < 1$ Hz per 1°.

The same analysis applies to the light-shift beam of the magnetometer operating in the LS mode. The average amplitude of the fictitious magnetic field due to the LS beam is 0.19 nT. Without the beam power stabilization the LS beam power noise was $1.5\%/\sqrt{Hz}$ at $f < 1$ Hz. Taking the geometric attenuation factor into account, the LS beam power fluctuations result in $\sim 1.1\,\mathrm{fT}/\sqrt{\mathrm{Hz}}$ magnetic field noise. If the LS beam and the leading field are not perfectly orthogonal, the additionally induced noise is $57\,\mathrm{fT}/\sqrt{\mathrm{Hz}}$ at $f < 1\,\mathrm{Hz}$ per each $1°$ of misalignment.

Both magnetometer configurations used the same polarimeter board and probe power. The equivalent magnetic field noise of the polarimeter in the dark was measured to be $0.17\,\mathrm{fT}/\sqrt{\mathrm{Hz}}$ (Appendix A). Another contribution into low-frequency magnetic field noise comes from the elevators moving in the proximity of the experimental setup. The measured change in the $\vec{B}_0$ magnitude due to the elevators movement was $\sim 5\,\mathrm{pT}$.

Contributions from all the noise sources are summarized in the Table 3.1.

Summary

We built an all-optical light shift magnetometer with projected sensitivity of $1.7\,\mathrm{fT}/\sqrt{\mathrm{Hz}}$ and demonstrated its performance in a laboratory setup with a noise floor of $40\,\mathrm{fT}/\sqrt{\mathrm{Hz}}$ at $2\,\mathrm{Hz}$. We compare it to the same magnetometer driven by a real oscillating magnetic field and demonstrate similar performance. We analyze what noise sources affect the magnetometer sensitivity and summarize them in Table 3.1. Analysis of the power spectrum of the magnetic-field changes shows that both magnetometers reach the same noise floor around 1.5 Hz and that the increased root mean square noise of the light-shift magnetometer is mostly due to low-frequency components. Overall, this demonstrates an improvement to current experiments where the sensors need to be placed in close proximity to each other and the use of actual magnetic fields is undesirable due to cross-talk issues and arrays of magnetometers are in use, e.g., in the search for an electric dipole moment of the neutron.

Source of noise	RF-driven mag.	LS magnetometer	Sync. pumped
Polarimeter technical noise	$0.17\,\mathrm{fT}/\sqrt{\mathrm{Hz}}$		
Polarimeter shot noise	$1.7\,\mathrm{fT}/\sqrt{\mathrm{Hz}}$		
Probe polarization	$0.5 - 1.2\,\mathrm{fT}/\sqrt{\mathrm{Hz}}$		
Probe optical frequency fluctuations	$< 0.01\,\mathrm{fT}/\sqrt{\mathrm{Hz}}$		
Pump power noise (perfectly aligned)	$10\,\mathrm{fT}/\sqrt{\mathrm{Hz}}$		$1.6\,\mathrm{fT}/\sqrt{\mathrm{Hz}}$ at f $< 1\,\mathrm{Hz}$
Pump power noise (per 1° of misalignment)	–		$\sim 66\,\mathrm{fT}/\sqrt{\mathrm{Hz}}$ at f $< 1\,\mathrm{Hz}$
Pump optical frequency fluctuations	$< 0.01\,\mathrm{fT}/\sqrt{\mathrm{Hz}}$		
LS beam power fluctuations (perfectly aligned)	–	$\sim 1.1\,\mathrm{fT}/\sqrt{\mathrm{Hz}}$ at f $< 1\,\mathrm{Hz}$	–
LS beam power fluctuations (per 1° of misalignment)	–	$\sim 57\,\mathrm{fT}/\sqrt{\mathrm{Hz}}$ at f $< 1\,\mathrm{Hz}$	–
LS beam optical frequency fluctuations	–	$< 0.01\,\mathrm{fT}/\sqrt{\mathrm{Hz}}$	–
$\vec{B}_0$ drifts	$< 100\,\mathrm{ppb}$ per $100\,\mathrm{s}$		
Magnetic noise in the room	$\sim 5\,\mathrm{pT}$ at f $< 0.1\,\mathrm{Hz}$		

Table 3.1: The noise contributions from various sources

3.2 All-optical vector magnetometer

The text presented in this section is part of a paper that has been published as Ref. [17].

Motivation

Spin-precession magnetometers [36,99] have found widespread application in disciplines ranging from geophysics [100] to medicine [101, 102] and fundamental physics [103, 104]. Alkali-vapor magnetometers in particular have experienced great advances in recent years, with sensitivities at or below the $\mathrm{fT}/\sqrt{\mathrm{Hz}}$ level demonstrated in the laboratory [100, 105–107]. Because these devices measure the Larmor precession frequency of atomic spins, they are intrinsically sensitive to the magnitude of an applied field rather than its projection along a particular direction. This can be advantageous in that precision of the scalar field measurement is not limited by physical alignment of the sensors, as it can be in the case of triaxial fluxgates or superconducting quantum interference devices (SQUIDs). Nevertheless, in many situations it is desirable to have full knowledge of a field's vector components.

There are several ways to derive vector field information from a scalar magnetometer. In bias-field nulling, calibrated magnetic fields are imposed upon the magnetometer in order to achieve a zero-field magnetic resonance condition [108–110]. With finite-field sensors using radiofrequency coils to drive the resonance (e.g., M_x magnetometers [111]), one may add secondary continuous light beams and measure their modulation to extract vector information [112, 113]. It is also possible to detect magnetically sensitive resonances in electromagnetically induced transparency (EIT) schemes; the amplitudes of different EIT resonances can yield information about the relative angle between the laser polarization and the field [114, 115]. Synchronously pumped magnetometers employing atomic alignment can also yield partial vector information when the magnetic field is not wholly perpendicular to the linear polarization of the pump beam [38].

Perhaps the simplest way to adapt a scalar magnetometer for vector measurements is to operate it in the finite-field regime (e.g., through synchronous optical pumping [5, 75, 116]) and apply time-varying fields to it. By applying orthogonal fields modulated at different frequencies, it is possible to demodulate the magnetic-resonance signal and determine which applied fields add linearly with the ambient field and which add in quadrature with it [117–119]. Although this is effective, there are some situations where this approach is infeasible or undesirable. One example would be the case of remote magnetometry [77,92], where it would be impractical to apply fields to a distant atomic sample. A different limitation appears in certain precision physics applications, such as the search for a neutron electric dipole moment (nEDM) [13, 104, 120, 121]. In such experiments alkali-vapor magnetometers can reduce systematic error by providing crucial magnetic-field information, but only if these sensors do not themselves produce field contamination. All-optical alkali-vapor magnetometers are particularly well suited for nEDM tests as they can be designed to produce no significant static or radiofrequency fields [122].

Here we demonstrate an all-optical vector magnetic sensor based upon nonlinear magneto-optical rotation in a cesium vapor. The effective magnetic field seen by the atoms is modulated by AC Stark shifts ("light shifts") induced by orthogonally propagating laser beams. Since the light shift of a circularly polarized beam is analogous [1] to an effective magnetic field oriented along its propagation direction [50, 51, 123], a comparison of the Larmor frequency shifts induced by these beams yields a measurement of the field angle. If technical noise were eliminated, this magnetometer would have 12 fT/$\sqrt{\text{Hz}}$ precision in measurement of the field magnitude and 5 μrad/$\sqrt{\text{Hz}}$ in the field direction.

Experiment

The experimental setup is shown in Fig. 3.5. The heart of the sensor is a cylindrical antirelaxation-coated [124] Cs vapor cell, approximately 5 cm diameter and 5 cm in length, with a longitudinal spin relaxation time of 0.7 seconds. This cell is enclosed within four layers of μ-metal magnetic shielding; measurements were performed at ambient temperature. Coils wound on a frame within the innermost shield allow magnetic fields and gradients to be applied to the cell. The field component oriented along $\hat{z}$ is produced by a current generated by a custom supply which can provide up to 150 mA (Magnicon GmbH). This supply is housed in a temperature-stabilized enclosure and exhibits a relative drift of $\sim 10^{-7}$ over 100 seconds. A second current supply (Krohn Hite 523) is connected to the coil in the $\hat{y}$ direction, allowing the net field $\mathbf{B}_0$ to be tilted in the $\hat{y}$–$\hat{z}$ plane. The pump beam which drives the magnetic resonance is generated by a distributed feedback (DFB) diode laser that is locked with a dichroic atomic vapor laser lock (DAVLL) [125] to the Cs $D1$ transition at 894 nm. The $\hat{x}$-directed pump is circularly polarized and amplitude modulated with an acousto-optic modulator (AOM) at the ^{133}Cs Larmor frequency ω_L to achieve synchronous optical pumping; the modulation waveform is a square wave with a duty cycle of 5%. A separate linearly polarized probe beam, generated by a DFB locked with a DAVLL to the Cs $D2$ transition, traverses the cell in the $\hat{y}$ direction. The probe experiences optical rotation [87] in the polarized Cs sample, modulating its polarization at ω_L. This is detected by a balanced polarimeter with a differential transimpedance amplifier; its output is fed into a digital lock-in amplifier (Stanford Research Systems SR830) whose reference frequency is provided by the local oscillator which drives the pump AOM. The phase of the lock-in amplifier is chosen such that the X(Y) output displays an absorptive (dispersive) Lorentzian as the driving frequency is scanned across the resonance. Directly on resonance, the X output is maximum and the Y output is nulled; small shifts in the magnetic-resonance frequency ω_L cause a linear change in the Y output about zero. With a time-averaged pump power of 2.5 μW and a probe power of 10 μW, the peak optical rotation signal is 5 mrad and the magnetic-resonance linewidth is 2.9 Hz. The dominant contributions to this linewidth are alkali–alkali spin-exchange broadening and slight power broadening due to the pump and

[1] See the Supplemental Information (Appendix C) for a discussion of the difference between the shifts induced by a light-shift beam and a magnetic field.

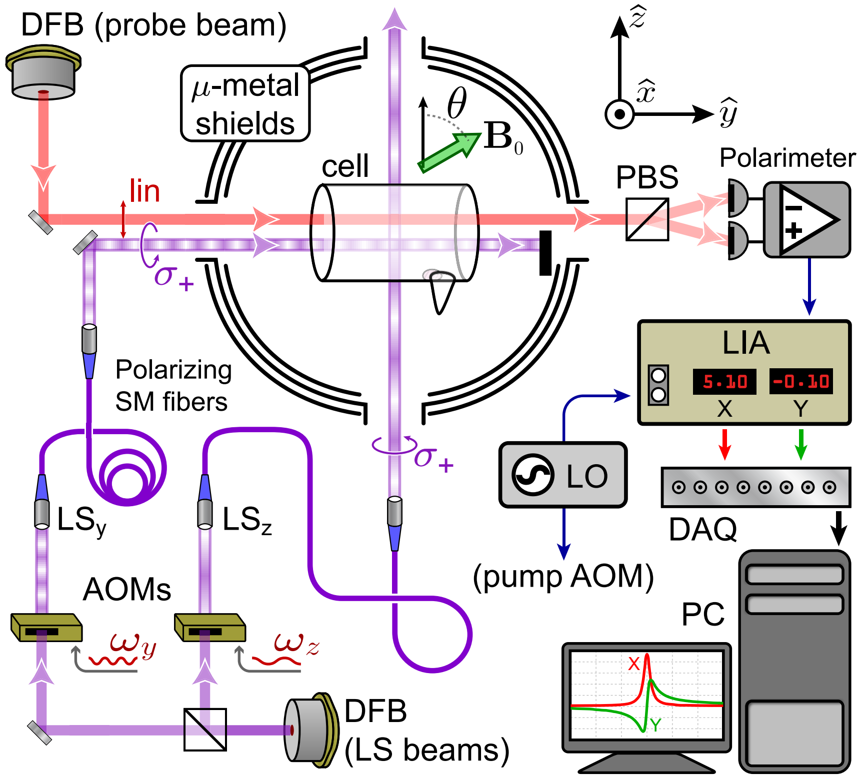

Figure 3.5: Experimental schematic. An amplitude-modulated, circularly polarized pump beam (not shown) propagates in the $\hat{x}$ direction. The local oscillator (LO) controls the pump AOM and serves as a reference to the lock-in amplifier (LIA), whose analog output is recorded by a data acquisition card (DAQ) and read into a computer (PC). A linearly polarized probe beam passes through the cell and is split by the polarizing beamsplitter (PBS) of a balanced polarimeter; the output of this polarimeter is demodulated by the lock-in. Two circularly polarized light-shift beams LS_y and LS_z are independently modulated and sent through the cell along $\hat{y}$ and $\hat{z}$. Coils allow the magnetic field $\mathbf{B}_0$ to be tilted in the $\hat{y}$–$\hat{z}$ plane.

probe beams. The beam powers and optical detunings were chosen to optimize the scalar sensitivity of the magnetometer.

In addition to the pump and probe, a third DFB laser tuned near the Cs $D2$ transition can be used to apply light-shift beams LS_y and LS_z in the $\hat{y}$ and $\hat{z}$ directions. The optical frequency of the light-shift laser is actively controlled using a wavelength meter (Ångstrom/HighFinesse WS-7) and computer control of the laser current. An optimal detuning of ∼5 GHz blue-shifted from the center of the $F = 4 \to F' = 5$ $D2$ transition was chosen to allow a large effective magnetic field (∼1 nT/mW) with minimal (≲0.5 Hz/mW) broadening of the magnetic-resonance line. This beam is split into two paths and sent through independent AOMs, then coupled into two polarizing[2] fiber patch cables (Fiber-

[2] Unlike conventional polarization-maintaining fiber, the HB830Z only transmits light which is linearly

core HB830Z). After the fibers, the light-shift beams are sent through quarter-wave plates to generate circularly polarized beams which pass through the cell along the $\hat{y}$ and $\hat{z}$ axes. Optical pickoffs (not shown in Fig. 3.5) and photodiodes directly before the shields allow the power of each light-shift beam to be measured. In an evacuated antirelaxation-coated cell, the alkali atoms rapidly sample the internal volume of the cell and experience a light shift equivalent to the volume-averaged intensity of the laser beam within the cell. Thus two beams of the same power will possess slightly different light-shift coefficients (measured in nT/mW) when propagating in different directions due to asymmetry of the cell dimensions. Nevertheless, their ratio will remain independent of the optical detuning of the light-shift laser.

To demonstrate the effective magnetic fields produced by LS_y and LS_z, we recorded the data shown in Fig. 3.6. For this measurement, the primary $\hat{z}$ field was held constant at 946.5 nT and an additional $\hat{y}$ field was varied between -1180.5 nT and +1177 nT. Thus the field's magnitude B_0 changed with its angle θ in the $\hat{y}$–$\hat{z}$ plane, requiring the local oscillator and the lock-in reference phase to be reset for each measurement. At each field, the respective light shifts produced by the LS_y and LS_z beams were measured by modulating the two beam intensities at different frequencies (12 and 20 Hz) and demodulating the lock-in Y output in software. The average intensity of each light-shift beam was 0.5 mW. Although it improves precision to measure the system response to both beams simultaneously, it is important to alternate the fast and slow modulation in each channel, as shown in Fig. 3.6. This is because the atomic system acts as a low-pass filter for fast field perturbations, since it is in effect a driven oscillator with a damping rate on the order of the magnetic-resonance linewidth.

Results

Assume that the magnetometer is operated in the finite-field regime, such that the magnetic resonance frequency is much higher than the resonance linewidth. The modulated LS_y beam produces an effective magnetic field of magnitude $B_y = P_y\alpha_y[{}^1\!/\!_2 + {}^1\!/\!_2 \sin(\omega_y t)]$, where P_y is the beam power, α_y is its effective light-shift coefficient, and ω_y the amplitude-modulation frequency. Similarly, LS_z produces $B_z = P_z\alpha_z[{}^1\!/\!_2 + {}^1\!/\!_2 \sin(\omega_z t)]$. To maintain the synchronous pumping condition, the fields B_y and B_z are assumed to be comparable to the resonance linewidth (in field units). Adding these fields to the vector components of $\mathbf{B}_0$, the total field magnitude becomes:

$$\begin{aligned} B_{\text{tot}} &= B_0\sqrt{1 + 2\frac{B_y\sin\theta + B_z\cos\theta}{B_0} + \frac{B_y^2 + B_z^2}{B_0^2}} \\ &\approx B_0 + B_y\sin\theta + B_z\cos\theta + \zeta, \end{aligned} \tag{3.1}$$

polarized along one of the axes of the anisotropic fiber core; the other polarization experiences large attenuation.

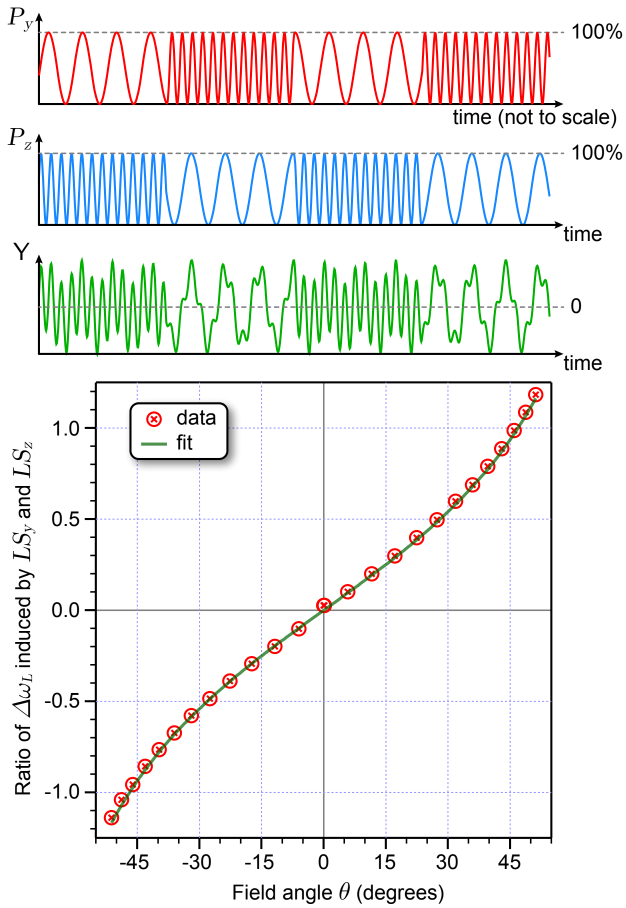

Figure 3.6: Above: Depiction of the LS_y and LS_z beam powers versus time and the resulting (simulated) change in the lock-in Y output about zero. Demodulation of the latter yields the contributions of LS_y and LS_z to the shift in the magnetic-resonance frequency. Below: The ratio of the Larmor frequency shift induced by the LS_y and LS_z beams, plotted as a function of field angle θ from the $\hat{z}$ axis. The curve shows a fit to Eq. (3.3). Each data point resulted from 20 seconds of averaging; uncertainties in the data points are uniformly below 10^{-2}.

where the approximation is valid for $B_y, B_z \ll B_0$ and the small quadratic correction ζ is given by:

$$\zeta = \frac{(B_y \cos\theta - B_z \sin\theta)^2}{2B_0}. \tag{3.2}$$

Since the lock-in Y output is proportional to the change in effective Larmor frequency induced by the light-shift fields, demodulation of the signal at frequencies ω_y and ω_z will extract the

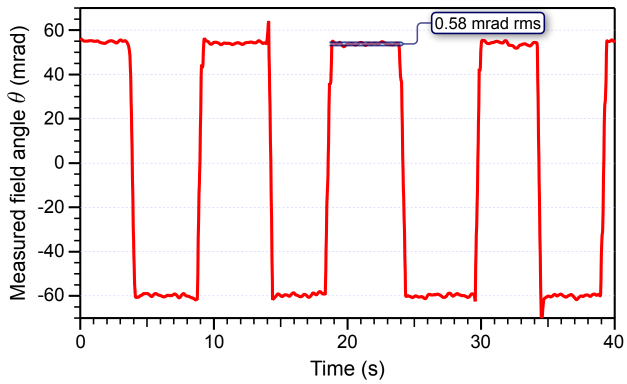

Figure 3.7: Measured field angle θ as a function of time while the applied $\hat{y}$ field is being switched. The average rms noise for a constant field angle translates to a precision of 0.47 mrad/$\sqrt{\text{Hz}}$ in measurement of the field direction. The steps in the plotted ratio are slightly low-pass filtered due to the time constants of the lock-in amplifier and the secondary demodulation at ω_y and ω_z.

terms in Eq. (3.1) proportional to B_y and B_z. Thus the ratio of the measured light shifts is:

$$\frac{(\Delta B_{\text{tot}})_{LSy}}{(\Delta B_{\text{tot}})_{LSz}} \approx \frac{P_y \alpha_y}{P_z \alpha_z} \tan\theta. \tag{3.3}$$

Here we have ignored the contribution from the terms in ζ and other terms of higher power in $(B_{y,z}/B_0)$, which cause modulation of B_{tot} at harmonics other than ω_y and ω_z or scale by powers of $|B_{y,z}/B_0|$ (here $\lesssim 10^{-3}$).

The data shown in Fig. 3.6 were fit to Eq. (3.3). The best-fit ratio $(P_y\alpha_y/P_z\alpha_z)$ was measured to be (0.94 ± 0.01) rather than unity, possibly due to slight asymmetry in the cell dimensions or systematic uncertainty of the beam powers within the cell. With no added light-shift beams, the synchronously pumped scalar sensor has sensitivity of 48 fT/$\sqrt{\text{Hz}}$ for integration times of 1 second, as calculated from the power spectral density (PSD) of the measured magnetic field, shown in Fig. 3.8. To confirm this sensitivity in the time domain, we stepped the local oscillator frequency by ± 0.875 mHz around ω_L and observed shifts in the lock-in Y output with a signal-to-noise ratio of 7.2. Given the lock-in's equivalent noise bandwidth (ENBW) of 1.25 Hz, this corresponds to a sensitivity of 62 fT/$\sqrt{\text{Hz}}$. To assess the uncertainty in the field angle, we recorded data with the $\hat{z}$ field held constant and the $\hat{y}$ field toggled between two small values. The lock-in Y signal was demodulated at ω_y and ω_z, and the ratio of these two responses converted to a measured magnetic-field angle according to the best-fit curve shown in Fig. 3.6. The resulting plot of θ vs. time is shown in Fig. 3.7. The modulation of the field angle is clearly visible, and the rms noise in the ratio corresponds to 0.47 mrad/$\sqrt{\text{Hz}}$ precision in the measured angle of the magnetic field. (This takes into account the measured ENBW of the software demodulation procedure.)

In the present setup, the precision of the measurement of θ is limited by apparent magnetic noise induced by fluctuations in the light-shift beam powers. With LS_z set to 1 mW

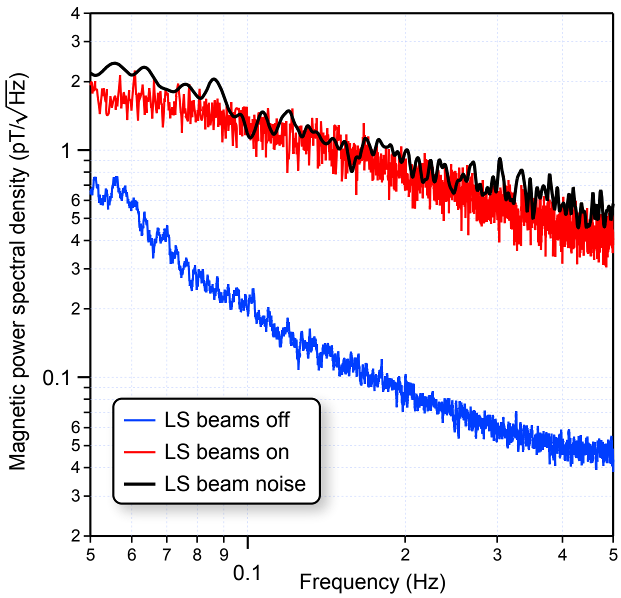

Figure 3.8: Power-spectral-density plot of the scalar field measurement with the LS_z beams turned off (blue) and turned on at a constant power of 1 mW (red). For these data, $\theta = 0$ and the light-shift beam power was not actively controlled. The black trace is the predicted noise floor the scalar field measurement taken from a (separate) recording of the light-shift beam power, from which a PSD was derived and the effective magnetic field calculated using the observed light-shift coefficients α_y and α_z.

without modulation and the field along $\hat{z}$, the smallest observable magnetic-field step with 1 Hz ENBW was 1.3 pT – a factor of 21 worse than the same data recorded without the light-shift beams. Power fluctuations in the LS_y and LS_z beams were recorded and converted into effective magnetic-field fluctuations according to the observed light-shift coefficients $\alpha_{y,z}$. As shown in Fig. 3.8, the predicted magnetic noise floor matches that observed in the magnetic-field PSD. Better control of intensity noise within the light-shift beams should allow dramatically improved scalar measurements and correspondingly better sensitivity to the field angle. The scalar sensitivity of the magnetometer would be 12 fT/$\sqrt{\text{Hz}}$ if the polarimeter and amplifiers operate at the photon shot-noise limit. By eliminating these sources of technical noise, it should be possible to reach a sensitivity of 5 μrad/$\sqrt{\text{Hz}}$ in the measurement of the magnetic-field direction.

Expanding the vector measurement to three dimensions will simply require adding another light-shift beam in the $\hat{x}$ direction. The bandwidth of the vector measurement is presently limited by the narrow magnetic-resonance line, but this can be expanded by power-broadening the resonance with the probe beam or heating the cell to increase the Cs density and spin-exchange-broadened linewidth. Either technique would allow more rapid measurement of the vector field components with little if any loss in sensitivity. As discussed in the Supplemental Material (Appendix C), the uncertainty in the measured angle θ has no intrinsic dependence on the magnitude of the ambient field B_0. Consequently, this technique should be applicable for vector magnetometry in geophysical fields with comparable precision, provided that a similar scalar sensitivity can be achieved.[3]

Summary

In conclusion, we have demonstrated a method for measuring the magnitude and direction of a magnetic field through all-optical interrogation of an atomic sample. This technique offers advantages over other methods (such as EIT vector magnetometry) because it relies on measuring changes in the magnetic-resonance frequency, rather than resonance amplitudes which can be affected by many experimental factors. Further optimization of the apparatus will allow for a compact, magnetically inert vector magnetometer well-suited for precision physics experiments or geophysical field measurement.

[3]This is true to the extent that the scalar sensitivity of the magnetometer is field-independent, an assumption which remains true for nonzero magnetic fields small enough that the nonlinear Zeeman structure is unresolved. For a $\sim$3 Hz resonance linewidth, that limit is on the order of 20 μT.

Chapter 4

Conclusion

Vector light shift effects in the ground state of ^{133}Cs atoms have been investigated using an optical atomic magnetometer setup. We measured the dependence of the effect on the optical power and frequency of the inducing beam in the D_1 and D_2 lines of ^{133}Cs. We established the optimal operating parameters for use in an atomic magnetometer by optimizing the figure of merit (the ratio of the shift and the magnetic resonance broadening). An unexpected phase shift in the magnetometer signal emerged during the experiments which was established to be another manifestation of the vector light shift effect, which produced a second magnetometer within the same sensor cell. In addition, we verified that the fictitious magnetic field produced by the vector light shift becomes averaged over the anti-relaxation coated cells, similarly to the real magnetic fields.

Two practical applications of the vector light shift have been demonstrated. They can be used to improve the atomic magnetometer as a device. By exploiting the fictitious magnetic fields, we converted a scalar atomic magnetometer into an all-optical magnetic field sensor which achieved 62 $\mathrm{fT}/\sqrt{\mathrm{Hz}}$ scalar and 0.47 $\mathrm{mrad}/\sqrt{\mathrm{Hz}}$ directional sensitivity. Prompted by the unexpected phase shift, we created an rf-like atomic magnetometer with the precession-inducing fictitious "rf-field" produced by a light shift beam. The sensitivity of this magnetometer measured 55 $\mathrm{fT}/\sqrt{\mathrm{Hz}}$, approximately the same as the magnetometer with a real rf-field (40 $\mathrm{fT}/\sqrt{\mathrm{Hz}}$) in the same setup.

The described modified atomic magnetometers can find applications where precise magnetic field monitoring and control are required, and where arrays of sensors in close proximity to each other are used, such as the search for the electric dipole moment of the neutron. We hope that the results presented in this thesis will prove to be useful for the design and construction of the "Supermag" project, which aims to achieve SERF sensitivity levels in geophysical field range.

Bibliography

[1] W. E. Bell and A. L. Bloom, "Optical detection of magnetic resonance in alkali metal vapor," *Phys. Rev.*, vol. 107, pp. 1559–1565, 1957.

[2] H. Dehmelt, "Modulation of a light beam by precessing absorbing atoms," *Physical Review*, vol. 105, no. 6, pp. 1924–1925, 1957.

[3] A. Kastler, "Optical methods of atomic orientation and of magnetic resonance," *J. Opt. Soc. Am.*, vol. 47, no. 6, pp. 460–465, 1957.

[4] H. B. Dang, A. C. Maloof, and M. V. Romalis, "Ultrahigh sensitivity magnetic field and magnetization measurements with an atomic magnetometer," *Applied Physics Letters*, vol. 97, no. 15, 2010.

[5] W. E. Bell and A. L. Bloom, "Optically driven spin precession," *Physical Review Letters*, vol. 6, pp. 280–281, 1961.

[6] J. Clarke and A. I. Braginski, *The SQUID Handbook*. Wiley-VCH, Weinheim, 2004.

[7] B. J. Venema, P. K. Majumder, S. K. Lamoreaux, B. R. Heckel, and E. N. Fortson, "Search for a coupling of the earth's gravitational field to nuclear spins in atomic mercury," *Phys. Rev. Lett.*, vol. 68, pp. 135–138, 1992.

[8] J. M. Brown, S. J. Smullin, T. W. Kornack, and M. V. Romalis, "New limit on Lorentz- and CPT-violating neutron spin interactions," *Physical Review Letters*, vol. 105, no. 15, 2010.

[9] S. Pustelny, D. F. J. Kimball, C. Pankow, M. P. Ledbetter, P. Wlodarczyk, P. Wcislo, M. Pospelov, J. R. Smith, J. Read, W. Gawlik, and D. Budker, "The Global Network of Optical Magnetometers for Exotic physics (GNOME): A novel scheme to search for physics beyond the Standard Model," *Annalen Der Physik*, vol. 525, no. 8-9, SI, pp. 659–670, 2013.

[10] I. Altarev, D. Beck, S. Chesnevskaya, T. Chupp, W. Feldmeier, P. Fierlinger, A. Frei, E. Gutsmiedl, F. Kuchler, P. Link, T. Lins, M. Marino, J. McAndrew, S. Paul, G. Petzoldt, A. Pichlmaier, R. Stoepler, S. Stuiber, and B. Tausenheim, "A next generation

measurement of the electric dipole moment of the neutron at the FRM II," *Nuovo Cimento C*, vol. 35C, pp. 122–7, 2012.

[11] C. Baker, Y. Chibane, M. Chouder, P. Geltenbort, K. Green, P. Harris, B. Heckel, P. Iaydjiev, S. Ivanov, I. Kilvington, S. Lamoreaux, D. May, J. Pendlebury, J. Richardson, D. Shiers, K. Smith, and M. van der Grinten, "Apparatus for measurement of the electric dipole moment of the neutron using a cohabiting atomic-mercury magnetometer," *Nuclear Instruments and Methods in Physics Research Section A: Accelerators, Spectrometers, Detectors and Associated Equipment*, vol. 736, no. 0, pp. 184 – 203, 2014.

[12] K. Green, P. Harris, P. Iaydjiev, D. May, J. Pendlebury, K. Smith, M. van der Grinten, P. Geltenbort, and S. Ivanov, "Performance of an atomic mercury magnetometer in the neutron EDM experiment," *Nuclear Instruments and Methods in Physics Research Section A: Accelerators, Spectrometers, Detectors and Associated Equipment*, vol. 404, no. 23, pp. 381 – 393, 1998.

[13] C. A. Baker, D. D. Doyle, P. Geltenbort, K. Green, M. G. D. van der Grinten, P. G. Harris, P. Iaydjiev, S. N. Ivanov, D. J. R. May, J. M. Pendlebury, J. D. Richardson, D. Shiers, and K. F. Smith, "Improved experimental limit on the electric dipole moment of the neutron," *Phys. Rev. Lett.*, vol. 97, p. 131801, 2006.

[14] J. J. Hudson, D. M. Kara, I. J. Smallman, B. E. Sauer, M. R. Tarbutt, and E. A. Hinds, "Improved measurement of the shape of the electron," *Nature*, vol. 473, no. 7348, pp. 493–496, 2011.

[15] D. Cho, K. Sangster, and E. A. Hinds, "Search for time-reversal-symmetry violation in thallium fluoride using a jet source," *Phys. Rev. A*, vol. 44, pp. 2783–2799, 1991.

[16] A. C. Vutha, W. C. Campbell, Y. V. Gurevich, N. R. Hutzler, M. Parsons, D. Patterson, E. Petrik, B. Spaun, J. M. Doyle, G. Gabrielse, and D. DeMille, "Search for the electric dipole moment of the electron with thorium monoxide," *J. Phys. B: At. Mol. Opt. Phys.*, vol. 43, no. 7, p. 074007, 2010.

[17] B. Patton, E. Zhivun, D. C. Hovde, and D. Budker, "All-optical vector atomic magnetometer," *Phys. Rev. Lett.*, vol. 113, p. 013001, 2014.

[18] G. Bison, R. Wynands, and A. Weis., "A laser-pumped magnetometer for the mapping of human cardio-magnetic fields," vol. 76, pp. 325–328, 2003.

[19] J. P. Wikswo, "Noninvasive magnetic detection of cardiac mechanical activity: Theory," *Medical Physics*, vol. 7, no. 4, 1980.

[20] J. F. Strasburger, B. Cheulkar, and R. T. Wakai, "Magnetocardiography for fetal arrhythmias," *Heart Rhythm*, vol. 5, no. 7, pp. 1073–1076, 2008.

[21] J. P. Wikswo, J. E. Opfer, and W. M. Fairbank, "Observation of human cardiac bloodflow by noninvasive measurement of magnetic susceptibility changes," *AIP Conference Proceedings*, vol. 18, no. 1, 1974.

[22] K. Tsukada, Y. Haruta, A. Adachi, H. Ogata, T. Komuro, T. Ito, Y. Takada, A. Kandori, Y. Noda, Y. Terada, and T. Mitsui, "Multichannel squid system detecting tangential components of the cardiac magnetic field," *Review of Scientific Instruments*, vol. 66, no. 10, 1995.

[23] J. Dammers, H. Chocholacs, E. Eich, F. Boers, M. Faley, R. E. Dunin-Borkowski, and N. Jon Shah, "Source localization of brain activity using helium-free interferometer," *Applied Physics Letters*, vol. 104, no. 21, 2014.

[24] R. Stolz, N. Bondarenko, V. Zakosarenko, M. Schulz, and H.-G. Meyer, "Integrated gradiometer-squid system for fetal magneto-cardiography without magnetic shielding," *Superconductor Science and Technology*, vol. 16, no. 12, p. 1523, 2003.

[25] R. Wyllie, M. Kauer, G. Smetana, R. Wakai, and T. Walker, "Magnetocardiography with a modular spin-exchange relaxation-free atomic magnetometer array," *Physics in medicine and biology*, vol. 57, no. 9, p. 2619, 2012.

[26] H. Xia, A. Ben-Amar Baranga, D. Hoffman, and M. V. Romalis, "Magnetoencephalography with an atomic magnetometer," *Applied Physics Letters*, vol. 89, no. 21, pp. –, 2006.

[27] C. N. Johnson, P. D. D. Schwindt, and M. Weisend, "Multi-sensor magnetoencephalography with atomic magnetometers," *Physics in Medicine and Biology*, vol. 58, no. 17, p. 6065, 2013.

[28] R. Wyllie, M. Kauer, R. T. Wakai, and T. G. Walker, "Optical magnetometer array for fetal magnetocardiography," *Optics letters*, vol. 37, no. 12, pp. 2247–2249, 2012.

[29] C. Gaffney, "Detecting trends in the prediction of the buried past: A review of geophysical techniques in archaeology," *Archaeometry*, vol. 50, no. 2, pp. 313–336, 2008.

[30] M. B. Rogers, J. E. Baham, and M. I. Dragila, "Soil iron content effects on the ability of magnetometer surveying to locate buried agricultural drainage pipes," *Applied Engineering in Agriculture*, vol. 22, no. 5, pp. 701–704, 2006.

[31] S. P. McKenna, K. B. Parkman, L. J. Perren, and J. R. McKenna, "Response of an electromagnetic gradiometer to a subsurface wire," *IEEE Transactions on Geoscience and Remote Sensing*, vol. 49, pp. 4944–4953, Dec 2011.

[32] J. McDonald, "UXO Detection and Characterization in the Marine Environment," tech. rep., Science Applications International Corp (saic) Cary Nc, Jul 2009.

[33] W. Chase, "Magnetometer," Feb. 23 1993. US Patent 5,189,368.

[34] R. Blakely, R. E. Wells, C. Weaver, and Johnson, "Location, structure, and seismicity of the seattle fault zone, washington: Evidence from aeromagnetic anomalies, geologic mapping, and seismic-reflection data," *Geological Society of America Bulletin*, vol. 114, pp. 169–177, 2002.

[35] H. E. Ross, R. J. Blakely, and M. D. Zoback, "Testing the use of aeromagnetic data for the determination of Curie depth in California," *Geophysics*, vol. 71, pp. L51–L59, 2006.

[36] edited by Dmitry Budker and D. F. J. Kimball, *Optical Magnetometry*. New York: Cambridge University Press, 2013.

[37] W. Happer, "Optical pumping," *Reviews of Modern Physics*, vol. 44, no. 2, p. 169, 1972.

[38] S. Pustelny, D. F. Jackson Kimball, S. M. Rochester, V. V. Yashchuk, W. Gawlik, and D. Budker, "Pump-probe nonlinear magneto-optical rotation with frequency-modulated light," *Phys. Rev. A*, vol. 73, p. 023817, 2006.

[39] E. B. Alexandrov, M. Auzinsh, D. Budker, D. F. Kimball, S. M. Rochester, and V. V. Yashchuk, "Dynamic effects in nonlinear magneto-optics of atoms and molecules: review," *J. Opt. Soc. Am. B*, vol. 22, no. 1, p. 7, 2005.

[40] Okunevic.AI, "Parametric relaxation resonance of optically oriented metastable He-4 atoms in an effective magnetic-field," *Zhurnal Eksperimentalnoi I Teoreticheskoi Fiziki*, vol. 67, pp. 881–889, 1974.

[41] D. Budker, W. Gawlik, D. F. Kimball, S. M. Rochester, V. V. Yashchuk, and A. Weis, "Resonant nonlinear magneto-optical effects in atoms," *Rev. Mod. Phys.*, vol. 74, pp. 1153–1201, 2002.

[42] P. C. D. Hobbs, *Building Electro-Optical Systems: Making It all Work*. Wiley, 2nd ed., 2009.

[43] M. Auzinsh, D. Budker, and S. Rochester, *Optically Polarized Atoms: Understanding Light-Atom Interactions*. OUP Oxford, 2010.

[44] A. Weis, G. Bison, and A. S. Pazgalev, "Theory of double resonance magnetometers based on atomic alignment," *Phys. Rev. A*, vol. 74, p. 033401, 2006.

[45] D. J. Griffiths, *Introduction To Electrodynamics*. Pearson, 4th ed., 2013.

[46] W. Happer and A. C. Tam, "Effect of rapid spin exchange on the magnetic-resonance spectrum of alkali vapors," *Phys. Rev. A*, vol. 16, pp. 1877–1891, 1977.

[47] D. A. Steck, "Cesium D Line Data." available online at http://steck.us/alkalidata. (revision 2.1.4, 23 December 2010).

[48] D. Budker, D. Kimball, and D. DeMille, *Atomic physics: An exploration through problems and solutions*. OUP Oxford, 2008.

[49] I. Mateos, B. Patton, E. Zhivun, D. Budker, D. Wurm, and J. Ramos-Castro, "Noise characterization of an atomic magnetometer at sub-millihertz frequencies," *Sensors and Actuators A: Physical*, vol. 224, no. 0, pp. 147 – 155, 2015.

[50] B. S. Mathur, H. Tang, and W. Happer, "Light shifts in the alkali atoms," *Phys. Rev.*, vol. 171, pp. 11–19, 1968.

[51] C. Cohen-Tannoudji and J. Dupont-Roc, "Experimental study of Zeeman light shifts in weak magnetic fields," *Phys. Rev. A*, vol. 5, pp. 968–984, 1972.

[52] K. Jensen, V. M. Acosta, J. M. Higbie, M. P. Ledbetter, S. M. Rochester, and D. Budker, "Cancellation of nonlinear Zeeman shifts with light shifts," *Phys. Rev. A*, vol. 79, p. 023406, 2009.

[53] W. Chalupczak, A. Wojciechowski, S. Pustelny, and W. Gawlik, "Competition between the tensor light shift and nonlinear Zeeman effect," *Phys. Rev. A*, vol. 82, p. 023417, 2010.

[54] F. Le Kien, P. Schneeweiss, and A. Rauschenbeutel, "Dynamical polarizability of atoms in arbitrary light fields: general theory and application to cesium," *The European Physical Journal D*, vol. 67, no. 5, 2013.

[55] I. A. Sulai, R. Wyllie, M. Kauer, G. S. Smetana, R. T. Wakai, and T. G. Walker, "Diffusive suppression of ac-stark shifts in atomic magnetometers," *Opt. Lett.*, vol. 38, no. 6, pp. 974–976, 2013.

[56] A. Podvyaznyi, A. Sakantsev, and V. Semenov, "About the Zeeman light-induced frequency shift of the radio-optical resonance in optically oriented isotopes of alkali metals," *Russian Physics Journal*, vol. 46, pp. 933–5, 2003.

[57] D. Budker, L. Hollberg, D. F. Kimball, J. Kitching, S. Pustelny, and V. V. Yashchuk, "Microwave transitions and nonlinear magneto-optical rotation in anti-relaxation-coated cells," *Phys. Rev. A*, vol. 71, p. 012903, 2005.

[58] J. C. Camparo, R. P. Frueholz, and C. H. Volk, "Inhomogeneous light shift in alkali-metal atoms," *Phys. Rev. A*, vol. 27, pp. 1914–1924, 1983.

[59] J. Skalla, S. Lang, and G. Wackerle, "Magnetic-resonance line-shapes in optical-pumping and light-shift experiments in alkali atomic vapors," *Journal Of The Optical Society Of America B-optical Physics*, vol. 12, no. 5, pp. 772–781, 1995.

[60] T. McClelland, L. K. Lam, and T. M. Kwon, "Anomalous narrowing of magnetic-resonance linewidths in optically pumped alkali-metal vapors," *Phys. Rev. A*, vol. 33, pp. 1697–1707, 1986.

[61] W. Chalupczak, P. Josephs-Franks, B. Patton, and S. Pustelny, "Spin-exchange narrowing of the atomic ground-state resonances," *Phys. Rev. A*, vol. 90, no. 4, 2014.

[62] W. Chalupczak, R. M. Godun, P. Anielski, A. Wojciechowski, S. Pustelny, and W. Gawlik, "Enhancement of optically pumped spin orientation via spin-exchange collisions at low vapor density," *Phys. Rev. A*, vol. 85, p. 043402, 2012.

[63] E. Zhivun, A. Wickenbrock, B. Patton, and D. Budker, "Alkali-vapor magnetic resonance driven by fictitious radiofrequency fields," *Applied Physics Letters*, vol. 105, no. 19, pp. –, 2014.

[64] E. Zhivun, A. Wickenbrock, J. Sudyka, S. Pustelny, B. Patton, and D. Budker, "Light shift averaging in paraffin-coated alkali vapor cells," *CoRR*, vol. arXiv:abs/1511.05345, 2015.

[65] M. Arditi and T. R. Carver, "Pressure, light, and temperature shifts in optical detection of 0-0 hyperfine resonance of alkali metals," *Phys. Rev.*, vol. 124, pp. 800–809, 1961.

[66] M. Arditi and J. L. Picque, "Precision measurements of light shifts induced by a narrow-band GaAs laser in the 0-0 ^{133}Cs hyperfine transition," *Journal of Physics B: Atomic and Molecular Physics*, vol. 8, no. 14, p. L331, 1975.

[67] Y. Yano, W. Gao, S. Goka, and M. Kajita, "Theoretical and experimental investigation of the light shift in ramsey coherent population trapping," *Phys. Rev. A*, vol. 90, p. 013826, 2014.

[68] J. Camparo, "Does the light shift drive frequency aging in the rubidium atomic clock?," *IEEE Transactions On Ultrasonics Ferroelectrics And Frequency Control*, vol. 52, no. 7, pp. 1075–1078, 2005.

[69] E. Breschi, G. Kazakov, C. Schori, G. Di Domenico, G. Mileti, A. Litvinov, and B. Matisov, "Light effects in the atomic-motion-induced ramsey narrowing of dark resonances in wall-coated cells," *Phys. Rev. A*, vol. 82, p. 063810, 2010.

[70] C. Affolderbach, F. Droz, and G. Mileti, "Experimental demonstration of a compact and high-performance laser-pumped rubidium gas cell atomic frequency standard," *IEEE T. Instrumentation and Measurement*, vol. 55, no. 2, pp. 429–435, 2006.

[71] A. Brillet, "Evaluation of the light shifts in an optically pumped cesium beam frequency standard," *Metrologia*, vol. 17, no. 4, pp. 147–150, 1981.

[72] S. Ohshima, Y. Nakadan, T. Ikegami, and Y. Koga, "Light shifts in an optically pumped cs beam frequency standard," *IEEE Transactions On Instrumentation And Measurement*, vol. 40, no. 6, pp. 1003–1007, 1991.

[73] B. Bulos, A. Marshall, and W. Happer, "Light shifts due to real transitions in optically pumped alkali atoms," *Physical Review A*, vol. 4, no. 1, pp. 51–&, 1971.

[74] C. W. White, W. M. Hughes, G. S. Hayne, and H. G. Robinson, "Determination of g-Factor Ratios for Free Rb^{85} and Rb^{87} Atoms," *Phys. Rev.*, vol. 174, pp. 23–32, 1968.

[75] J. M. Higbie, E. Corsini, and D. Budker, "Robust, high-speed, all-optical atomic magnetometer," *Review of Scientific Instruments*, vol. 77, no. 11, pp. –, 2006.

[76] V. Acosta, M. P. Ledbetter, S. M. Rochester, D. Budker, D. F. Jackson Kimball, D. C. Hovde, W. Gawlik, S. Pustelny, J. Zachorowski, and V. V. Yashchuk, "Nonlinear magneto-optical rotation with frequency-modulated light in the geophysical field range," *Phys. Rev. A*, vol. 73, p. 053404, 2006.

[77] B. Patton, O. O. Versolato, D. C. Hovde, E. Corsini, J. M. Higbie, and D. Budker, "A remotely interrogated all-optical ^{87}Rb magnetometer," *Applied Physics Letters*, vol. 101, no. 8, pp. –, 2012.

[78] S. Groeger, G. Bison, J.-L. Schenker, R. Wynands, and A. Weis, "A high-sensitivity laser-pumped mx magnetometer," *The European Physical Journal D - Atomic, Molecular, Optical and Plasma Physics*, vol. 38, no. 2, pp. 239–247, 2006.

[79] Z. Gruji, P. Koss, G. Bison, and A. Weis, "A sensitive and accurate atomic magnetometer based on free spin precession," *The European Physical Journal D*, vol. 69, no. 5, 2015.

[80] S. J. Seltzer, P. J. Meares, and M. V. Romalis, "Synchronous optical pumping of quantum revival beats for atomic magnetometry," *Phys. Rev. A*, vol. 75, p. 051407, 2007.

[81] V. G. Lucivero, P. Anielski, W. Gawlik, and M. W. Mitchell, "Shot-noise-limited magnetometer with sub-picotesla sensitivity at room temperature," *Review of Scientific Instruments*, vol. 85, no. 11, pp. –, 2014.

[82] S. Pustelny, A. Wojciechowski, M. Gring, M. Kotyrba, J. Zachorowski, and W. Gawlik, "Magnetometry based on nonlinear magneto-optical rotation with amplitude-modulated light," *Journal of Applied Physics*, vol. 103, no. 6, pp. –, 2008.

[83] M. V. Balabas, T. Karaulanov, M. P. Ledbetter, and D. Budker, "Polarized alkali-metal vapor with minute-long transverse spin-relaxation time," *Physical Review Letters*, vol. 105, no. 7, 2010.

[84] S. Pustelny, D. F. Jackson Kimball, S. M. Rochester, V. V. Yashchuk, and D. Budker, "Influence of magnetic-field inhomogeneity on nonlinear magneto-optical resonances," *Phys. Rev. A*, vol. 74, p. 063406, 2006.

[85] K. L. Corwin, Z.-T. Lu, C. F. Hand, R. J. Epstein, and C. E. Wieman, "Frequency-stabilized diode laser with the Zeeman shift in an atomic vapor," *Appl. Opt.*, vol. 37, no. 15, pp. 3295–3298, 1998.

[86] C. Lee, G. Z. Iwata, E. Corsini, J. M. Higbie, S. Knappe, M. P. Ledbetter, and D. Budker, "Small-sized dichroic atomic vapor laser lock," *Review of Scientific Instruments*, vol. 82, no. 4, pp. –, 2011.

[87] D. Budker, W. Gawlik, D. Kimball, S. Rochester, V. Yashchuk, and A. Weis, "Resonant nonlinear magneto-optical effects in atoms," *Reviews Of Modern Physics*, vol. 74, no. 4, pp. 1153–1201, 2002.

[88] G. Bison, N. Castagna, A. Hofer, P. Knowles, J.-L. Schenker, M. Kasprzak, H. Saudan, and A. Weis, "A room temperature 19-channel magnetic field mapping device for cardiac signals," *Applied Physics Letters*, vol. 95, no. 17, pp. –, 2009.

[89] G. Lembke, S. N. Erne, H. Nowak, B. Menhorn, and A. Pasquarelli, "Optical multichannel room temperature magnetic field imaging system for clinical application," *Biomedical Optics Express*, vol. 5, no. 3, pp. 876–881, 2014.

[90] S. Groeger, G. Bison, and A. Weis, "Design and performance of laser-pumped Cs-magnetometers for the planned UCN EDM experiment at PSI," *Journal Of Research Of The National Institute Of Standards And Technology*, vol. 110, no. 3, pp. 179–183, 2005. International Conference on Precision Measurements with Slow Neutrons, Natl Inst Stand & Technol, Gaithersburg, MD, APR 05-07, 2004.

[91] E. B. Aleksandrov, M. V. Balabas, S. P. Dmitriev, N. A. Dovator, A. I. Ivanov, M. I. Karuzin, V. N. Kulyasov, A. S. Pazgalev, and A. P. Serebrov, "Quantum magnetometer for stabilization of the neutron magnetic resonance," *Technical Physics Letters*, vol. 32, no. 7, pp. 627–629, 2006.

[92] J. M. Higbie, S. M. Rochester, B. Patton, R. Holzlhner, D. Bonaccini Calia, and D. Budker, "Magnetometry with mesospheric sodium," *Proceedings of the National Academy of Sciences*, vol. 108, no. 9, pp. 3522–3525, 2011.

[93] M. T. Graf, D. F. Kimball, S. M. Rochester, K. Kerner, C. Wong, D. Budker, E. B. Alexandrov, M. V. Balabas, and V. V. Yashchuk, "Relaxation of atomic polarization in paraffin-coated cesium vapor cells," *Phys. Rev. A*, vol. 72, p. 023401, 2005.

[94] Y. Yoshikawa, T. Umeki, T. Mukae, Y. Torii, and T. Kuga, "Frequency stabilization of a laser diode with use of light-induced birefringence in an atomic vapor," *Appl. Opt.*, vol. 42, no. 33, pp. 6645–6649, 2003.

[95] S. Appelt, A. Ben-Amar Baranga, A. R. Young, and W. Happer, "Light narrowing of rubidium magnetic-resonance lines in high-pressure optical-pumping cells," *Phys. Rev. A*, vol. 59, pp. 2078–2084, 1999.

[96] T. Scholtes, V. Schultze, R. IJsselsteijn, S. Woetzel, and H.-G. Meyer, "Light-narrowed optically pumped M_x magnetometer with a miniaturized Cs cell," *Phys. Rev. A*, vol. 84, p. 043416, 2011.

[97] V. Shah, G. Vasilakis, and M. V. Romalis, "High bandwidth atomic magnetometery with continuous quantum nondemolition measurements," *Phys. Rev. Lett.*, vol. 104, p. 013601, 2010.

[98] O. Alem, K. L. Sauer, and M. V. Romalis, "Spin damping in an rf atomic magnetometer," *Phys. Rev. A*, vol. 87, p. 013413, 2013.

[99] D. Budker and M. Romalis, "Optical magnetometry," *Nature Physics*, vol. 3, no. 4, pp. 227–234, 2007.

[100] H. B. Dang, A. C. Maloof, and M. V. Romalis, "Ultrahigh sensitivity magnetic field and magnetization measurements with an atomic magnetometer," *Appl. Phys. Lett.*, vol. 97, no. 15, p. 151110, 2010.

[101] G. Bison, N. Castagna, A. Hofer, P. Knowles, J.-L. Schenker, M. Kasprzak, H. Saudan, and A. Weis, "A room temperature 19-channel magnetic field mapping device for cardiac signals," *Appl. Phys. Lett.*, vol. 95, no. 17, p. 173701, 2009.

[102] C. N. Johnson, P. D. D. Schwindt, and M. Weisend, "Multi-sensor magnetoencephalography with atomic magnetometers," *Physics in Medicine and Biology*, vol. 58, no. 17, pp. 6065–6077, 2013.

[103] G. Vasilakis, J. M. Brown, T. W. Kornack, and M. V. Romalis, "Limits on new long range nuclear spin-dependent forces set with a K-He3 comagnetometer," *Phys. Rev. Lett.*, vol. 103, no. 26, 2009.

[104] I. Altarev, C. A. Baker, G. Ban, G. Bison, K. Bodek, M. Daum, P. Fierlinger, P. Geltenbort, K. Green, M. G. D. van der Grinten, E. Gutsmiedl, P. G. Harris, W. Heil, R. Henneck, M. Horras, P. Iaydjiev, S. N. Ivanov, N. Khomutov, K. Kirch, S. Kistryn, A. Knecht, P. Knowles, A. Kozela, F. Kuchler, M. Kuźniak, T. Lauer, B. Lauss, T. Lefort, A. Mtchedlishvili, O. Naviliat-Cuncic, A. Pazgalev, J. M. Pendlebury, G. Petzoldt, E. Pierre, G. Pignol, G. Quéméner, M. Rebetez, D. Rebreyend, S. Roccia, G. Rogel, N. Severijns, D. Shiers, Y. Sobolev, A. Weis, J. Zejma, and G. Zsigmond, "Test of Lorentz invariance with spin precession of ultracold neutrons," *Phys. Rev. Lett.*, vol. 103, no. 8, 2009.

[105] M. P. Ledbetter, I. M. Savukov, V. M. Acosta, D. Budker, and M. V. Romalis, "Spin-exchange-relaxation-free magnetometry with Cs vapor," *Phys. Rev. A*, vol. 77, no. 3, 2008.

[106] W. C. Griffith, S. Knappe, and J. Kitching, "Femtotesla atomic magnetometry in a microfabricated vapor cell," *Opt. Express*, vol. 18, no. 26, p. 27167, 2010.

[107] S. J. Smullin, I. M. Savukov, G. Vasilakis, R. K. Ghosh, and M. V. Romalis, "Low-noise high-density alkali-metal scalar magnetometer," *Phys. Rev. A*, vol. 80, no. 3, 2009.

[108] R. E. Slocum and F. N. Reilly, "Low field helium magnetometer for space applications," *IEEE Transactions on Nuclear Science*, vol. 10, no. 1, pp. 165 – 171, 1963.

[109] S. Seltzer and M. Romalis, "Unshielded three-axis vector operation of a spin-exchange-relaxation-free atomic magnetometer," *Applied Physics Letters*, vol. 85, no. 20, p. 4804, 2004.

[110] H. Dong, H. Lin, and X. Tang, "Atomic-signal-based zero-field finding technique for unshielded atomic vector magnetometer," *IEEE Sensors J.*, vol. 13, no. 1, pp. 186–189, 2013.

[111] A. L. Bloom, "Principles of operation of the rubidium vapormagnetometer," *Appl. Opt.*, vol. 1, no. 1, pp. 61–68, 1962.

[112] A. J. Fairweather and M. J. Usher, "A vector rubidium magnetometer," *Journal of Physics E: Scientific Instruments*, vol. 5, no. 10, p. 986, 1972.

[113] A. K. Vershovskii, "Project of laser-pumped quantum M_x magnetometer," *Technical Physics Letters*, vol. 37, no. 2, pp. 140–143, 2011.

[114] H. Lee, M. Fleischhauer, and M. O. Scully, "Sensitive detection of magnetic fields including their orientation with a magnetometer based on atomic phase coherence," *Phys. Rev. A*, vol. 58, pp. 2587–2595, 1998.

[115] K. Cox, V. I. Yudin, A. V. Taichenachev, I. Novikova, and E. E. Mikhailov, "Measurements of the magnetic field vector using multiple electromagnetically induced transparency resonances in Rb vapor," *Phys. Rev. A*, vol. 83, p. 015801, 2011.

[116] W. Gawlik, L. Krzemie, S. Pustelny, D. Sangla, J. Zachorowski, M. Graf, A. O. Sushkov, and D. Budker, "Nonlinear magneto-optical rotation with amplitude modulated light," *Applied Physics Letters*, vol. 88, no. 13, pp. –, 2006.

[117] J. Rasson, "Rubidium vapour vector magnetometer," *Geophysical Transactions – Eötvös Loránd Geophysical*, vol. 36, no. 187, p. 187, 1991.

[118] O. Gravrand, A. Khokhlov, J. Le Mouel, and J. Leger, "On the calibration of a vectorial He-4 pumped magnetometer," *Earth Planets And Space*, vol. 53, no. 10, pp. 949–958, 2001.

[119] A. Vershovskii, M. Balabas, A. Ivanov, V. Kulyasov, A. Pazgalev, and E. Aleksandrov, "Fast three-component magnetometer-variometer based on a cesium sensor," *Technical Physics*, vol. 51, no. 1, pp. 112–117, 2006.

[120] P. Knowles, G. Bison, N. Castagna, A. Hofer, A. Mtchedlishvili, A. Pazgalev, and A. Weis, "Laser-driven Cs magnetometer arrays for magnetic field measurement and control," *Nuclear Instruments and Methods in Physics Research Section A: Accelerators, Spectrometers, Detectors and Associated Equipment*, vol. 611, no. 23, pp. 306 – 309, 2009. Particle Physics with Slow Neutrons.

[121] I. Altarev, D. H. Beck, S. Chesnevskaya, T. Chupp, W. Feldmeier, P. Fierlinger, A. Frei, E. Gutsmiedl, F. Kuchler, P. Link, T. Lins, M. Marino, J. McAndrew, S. Paul, G. Petzoldt, A. Pichlmaier, R. Stoepler, S. Stuiber, and B. Taubenheim, "A next generation measurement of the electric dipole moment of the neutron at the FRM II2012," *Il Nuovo Cimento C*, vol. 35, no. 4, p. 122127, 2012.

[122] B. Patton, D. C. Hovde, J. McAndrew, M. Sturm, P. Fierlinger, S. A. Schnabel, Sharma, D. Beck, M. Balabas, and D. Budker. (manuscript in preparation).

[123] T. Moriyasu, D. Nomoto, Y. Koyama, Y. Fukuda, and T. Kohmoto, "Spin manipulation using the light-shift effect in rubidium atoms," *Phys. Rev. Lett.*, vol. 103, p. 213602, 2009.

[124] S. J. Seltzer, D. J. Michalak, M. H. Donaldson, M. V. Balabas, S. K. Barber, S. L. Bernasek, M.-A. Bouchiat, A. Hexemer, A. M. Hibberd, D. F. J. Kimball, C. Jaye, T. Karaulanov, F. A. Narducci, S. A. Rangwala, H. G. Robinson, A. K. Shmakov, D. L. Voronov, V. V. Yashchuk, A. Pines, and D. Budker, "Investigation of antirelaxation coatings for alkali-metal vapor cells using surface science techniques," *The Journal of Chemical Physics*, vol. 133, no. 14, p. 144703, 2010.

[125] V. V. Yashchuk, D. Budker, and J. R. Davis, "Laser frequency stabilization using linear magneto-optics," *Review of Scientific Instruments*, vol. 71, no. 2, pp. 341–346, 2000.

[126] W. Happer, "Light propagation and light shifts in optical pumping experiments," *Progress in Quantum Electronics*, vol. 1, Part 2, pp. 51 – 103, 1970.

[127] C. Y. Park, H. Noh, C. M. Lee, and D. Cho, "Measurement of the Zeeman-like ac Stark shift," *Phys. Rev. A*, vol. 63, p. 032512, 2001.

[128] W. Happer and S. Svanberg, "Power-series analysis of light shifts in optical pumping experiments," *Phys. Rev. A*, vol. 9, pp. 508–519, Jan 1974.

[129] J. Skalla, S. Lang, and G. Wackerle, "Magnetic-resonance line-shapes in optical-pumping and light-shift experiments in alkali atomic vapors," *Journal of the Optical Society of America B-Optical Physics*, vol. 12, no. 5, pp. 772–781, 1995.

[130] C. Cohen-Tannoudji *Annales de Physique*, vol. 7, p. 423, 1962.

[131] C. Cohen-Tannoudji *Annales de Physique*, vol. 7, p. 469, 1962.

[132] A. Ben-Kish and M. V. Romalis, "Dead-zone-free atomic magnetometry with simultaneous excitation of orientation and alignment resonances," *Phys. Rev. Lett.*, vol. 105, p. 193601, Nov 2010.

Appendix A

Differential photoamplifier

Measuring polarization rotation

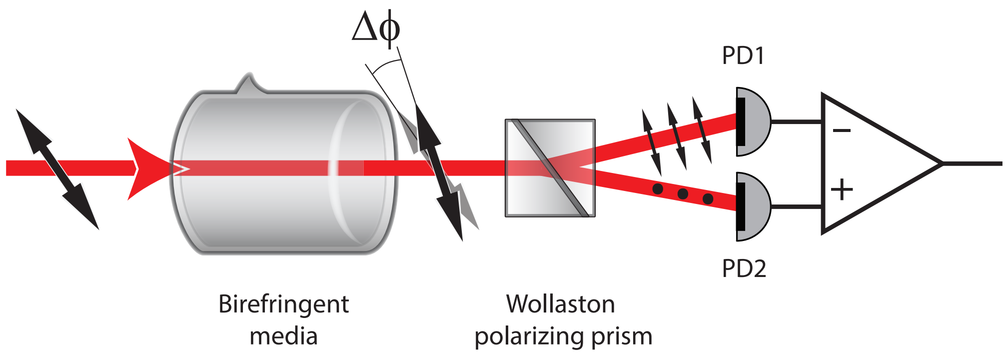

Figure A.1: Optical scheme of the polarization rotation measurement.

A setup for polarization rotation measurement used in this thesis is presented in Figure A.1. Linearly polarized beam propagates through a birefringent media, which results in the rotation of its polarization plane [87]. To determine the rotation angle $\Delta\phi$, the beam is split by a Wollaston[1] polarizer installed at 45° to the original beam polarization. Intensities of the two resulting beams are measured with two photodiodes PD1 and PD2. The angle ϕ that the polarization plane makes with the polarizer can be inferred from the signal amplitudes in corresponding polarimeter channels V_1 and V_2:

$$\phi = \arcsin\sqrt{\frac{1}{2}\left(1 - \frac{\Delta}{\Sigma}\right)}, \tag{A.1}$$

[1] The Wollaston polarizer was chosen to make the geometry of the setup symmetric and therefore easier to build and align.

where $\Delta = V_1 - V_2$ and $\Sigma = V_1 + V_2$. When the deviation from the original polarization angle is small ($\ll 1\,\mathrm{rad}$), it can be approximated as

$$\Delta\phi = \frac{\Delta}{2\Sigma}. \tag{A.2}$$

An inherent noise source in this measurement is the uncertainty in number of photons arriving into each polarimeter channel (photon shot noise) [48]:

$$\delta\phi = \frac{1}{2\sqrt{N_{ph}}}, \tag{A.3}$$

where N_{ph} is the total number of photons received by the polarimeter during the measurement. It is important to ensure that at the frequency of interest the technical noise of the polarimeter electronics stays below the photon shot noise. Designing a high-speed high-sensitivity photo amplifier is considered in detail in [42].

DAVLL polarimeter v0.1

Performance

DAVLL polarimeter is a low-speed version of the High-Speed polarimeter designed by Brian Patton that was originally based on a cascode amplifier design [42]. All the experiments described in this thesis employ this board for measuring spin precession.

The photoamplifier is designed for use with DAVLL [86] with the goal of minimizing low-frequency output drifts while having a high gain. The board has $10\,\mathrm{V}/\mu\mathrm{A}$ trans-impedance gain and is shot noise limited at $0.5\,\mu\mathrm{W}$. The noise limit is due to the Johnson noise of R6, which is $130\,\mathrm{fA}/\sqrt{\mathrm{Hz}}$ when R6 = R12 = R13 = $1\,\mathrm{M}\Omega$. Bandwidth of the polarimeter board is $30\,\mathrm{kHz}$.

The polarimeter's Bode plots are presented on the Figure A.3. Figures A.2a and A.2b show dependence of the photocurrent noise on the light intensity that was used to determine the noise limit of the board.

Part list and schematic

The polarimeter is a compact PCB mounted on a CRM1 30 mm Thorlabs rotating stage along with the Wollaston prism. The board dimensions are $1.6'' \times 1.6''$ (Figure A.4)

Figure A.5 shows the schematic of the photoamplifier. Table A.1 lists the part names and values. More detailed assembly instructions can be found at this link.

Furhter development

The polarimeter underwent several iterations that improved the performance of the board. One of the newer versions of the board developed for Laser Interferometer Space Antenna (LISA) mission is described in [49].

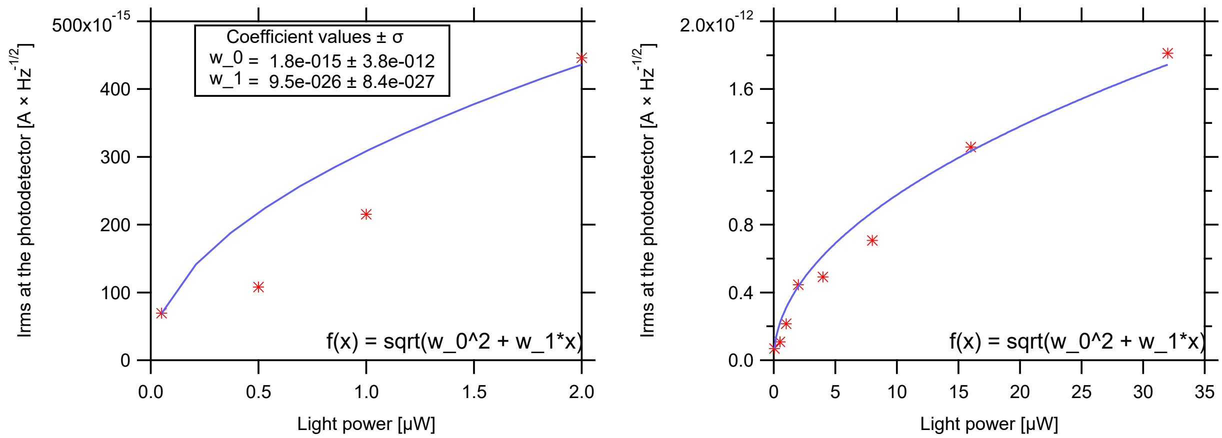

(a) RMS current noise (0–2μW) (b) RMS current noise (0–32μW)

Figure A.2: Current noise of the DIFF output of the polarimeter depending on the total optical power reaching the photodiodes

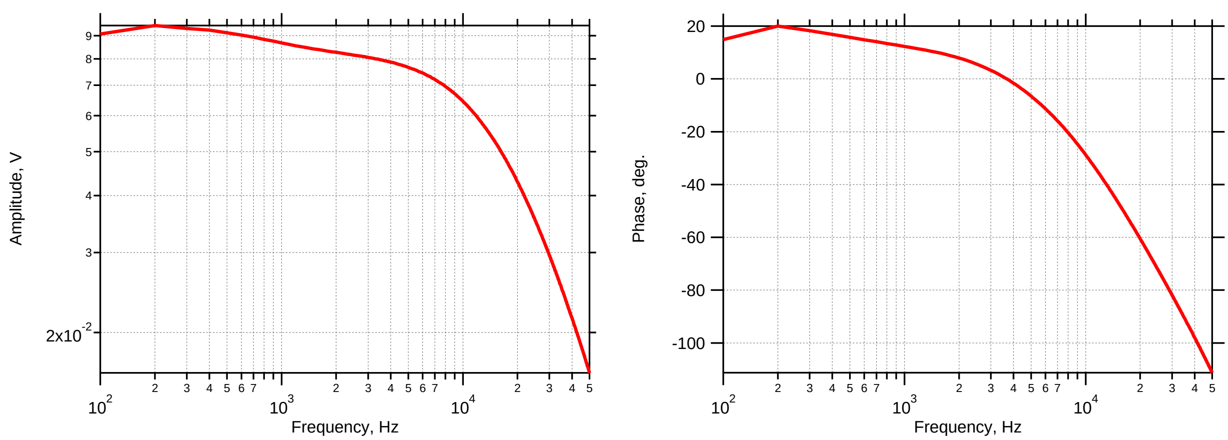

(a) Output amplidude vs signal frequency (b) Output phase vs signal frequency

Figure A.3: Polarimeter Bode plots

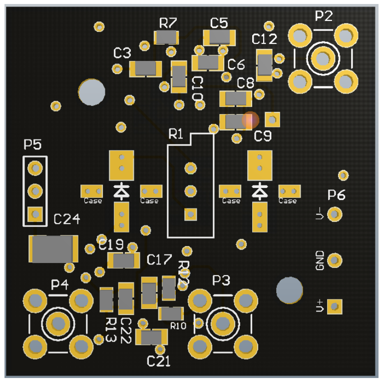

(a) Front

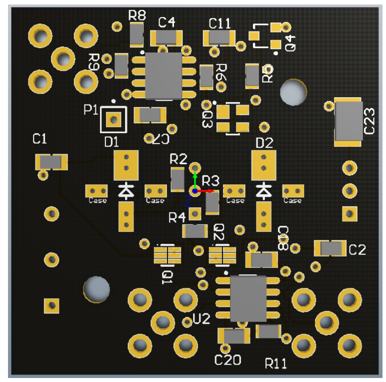

(b) Back

Figure A.4: Polatimeter PCB

Reference	Part	Reference	Part
Q1	BC846S	R14, R10, R11	$0\,\Omega$
Q2	BC856S	R2, R3, R4	$11\,\Omega$
C3, C4	Tantalum $12\,\mathrm{V}$ $22\,\mu\mathrm{F}$	R5, R8	$1\,\mathrm{k}\Omega$
C10	$10\,\mathrm{pF}$	R9	$11\,\mathrm{k}\Omega$
C17, C22	$33\,\mathrm{pF}$	R12, R13	$100\,\mathrm{k}\Omega$
C1, C2, C21, C18	$100\,\mathrm{pF}$	R6, R7	$500\,\mathrm{k}\Omega$
U1[a], U2, U3[b], U4	OP-07	D1, D2	S1337-33BR
DIFF OUT	SMA straight connector	PWR	3-pin Molex header
PD1DC, PD2DC	SMA straight connector	R1	(not mounted)

Table A.1: Parts of DAVLL Polarimeter 0.1

[a]Needs to be connected to Vcc

[b]Noise improvement can be achieved if AD825 is used for U3

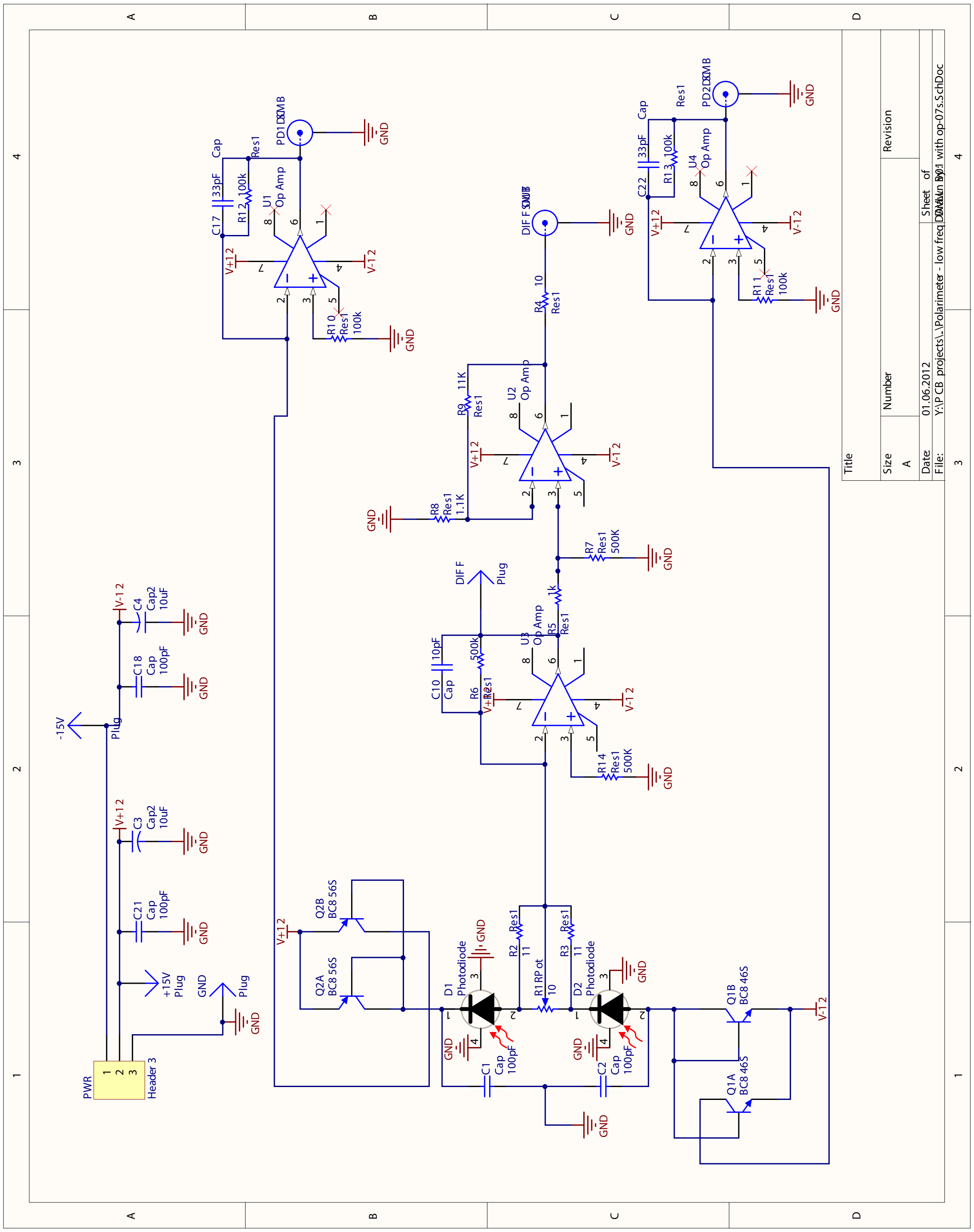

Figure A.5: Schematic of DAVLL Polarimeter 0.1 electric circuit.

Appendix B

Low-pass filtering by a paraffin-coated cell

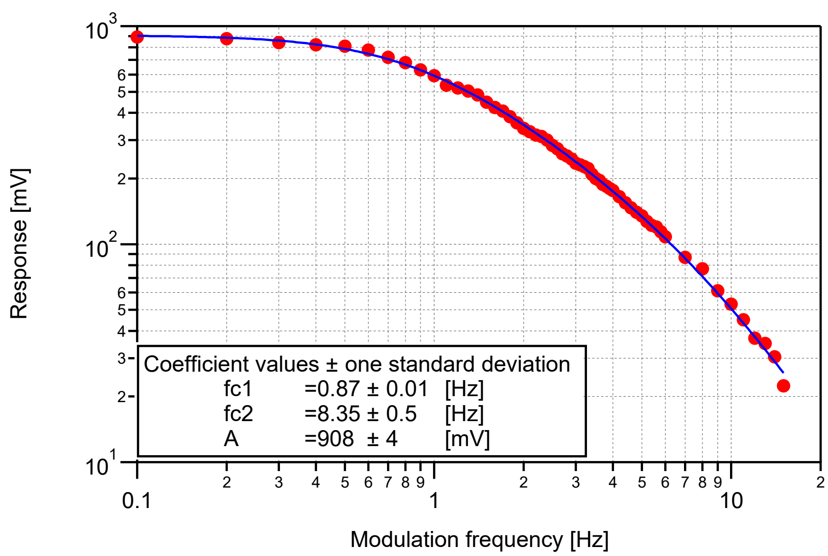

Figure B.1: Amplitude of the FFT peak in the demodulated magnetometer response depending on modulation frequency of the pump pulse rate.

When the amplitude or the frequency of the pump light is changed, the precessing polarization in the cell does not respond to the change instantly. This delay is related to the atoms depolarization rate, and the transfer of the atoms between the ground-state manifolds (only one of which is addressed by the pump) due to the spin-exchange collisions.

In a synchronously-pumped magnetometer we modulated the pump pulse frequency in the vicinity of the magnetic resonance with the frequency deviation of 10 mHz and modulation frequency in the range of $0.1-15$ Hz. The polarimeter signal was demodulated with a lock-in amplifier at the center frequency of the magnetic resonance. For each modulation frequency the FFT of the lock-in Y channel was taken and the signal at the modulation frequency recorded.

Figure B.1 is the plot of how the cell used in the experiments responded to the change of the pump optical frequency. The response fit function represents two cascaded first-order low-pass filters:

$$R(x) = \frac{A}{\sqrt{1+(f/f_{c1})^2}\sqrt{1+(f/f_{c2})^2}}. \tag{B.1}$$

The best fit coefficients for the fit frequencies were $f_{c1} = 0.87\,\mathrm{Hz}$ and $f_{c2} = 8.4\,\mathrm{Hz}$. The fit corner frequencies are close to the inverted measured T_1 (0.7 s) and T_2 (140 ms) times of the cell. The fit coefficients were likely affected by the lock-in amplifier filtering ($f_c = 16\,\mathrm{Hz}$, 12 db/oct).

Throughout the experiments we used this measured cell response to correct the linear spectrum density data of the sensor.

Appendix C

All-Optical Vector Atomic Magnetometer – Supplemental Material

Experimental Details

Prior to each long-term measurement, the scalar sensitivity of the magnetometer was optimized through adjustment of the pump and probe beam powers and optical detunings. This optimum was found by measuring the signal-to-noise ratio of the magnetic-resonance curve and, independently, by stepping the local oscillator frequency by small amounts around ω_L and maximizing the resulting shift in the lock-in output. (In sensitivity measurements, this is functionally equivalent to applying small shifts in the magnetic-field magnitude.) The optimal parameters for the pump and probe beams are relatively forgiving, and over a range of $\sim$1 GHz in optical frequency it is possible to achieve the same sensitivity by choosing appropriate beam powers (higher powers requiring greater detuning from the optical absorption line).

For the measurements shown in Figs. 2 and 4 of the main text, active feedback was used to control the LS_y and LS_z beam powers. Each light-shift beam has an optical pickoff outside the shields which directs a small fraction of the beam's power onto a photodiode. The resulting photocurrent is sent through a current preamplifier (Stanford Research Systems SR570) whose output voltage is measured by a PID controller (Stanford Research Systems SIM960) and compared to a set voltage given by an analog output of the data acquisition board. The output of the PID controller is sent to the AOM analog input, so that the observed optical power can be controlled by computer and modulated at frequencies in excess of 1 kHz. Prior to the experiment we measured the power of the LS_y and LS_z beams within the μ-metal shields in order to convert these voltages into real beam powers. For added precision, the measured beam powers are recorded during data acquisition. When processing the data, we take the Fourier transform of these recorded voltages in order to calculate each beam's power spectral density at its modulation frequency. The response of the lock-in output to each light-shift beam is normalized according to this measurement.

The long coherence time of atoms within the antirelaxation-coated cell allows measurement of narrow magnetic-resonance spectra, but also results in a low-pass-filtering effect for measurement of changing magnetic fields. In the present experiment, this low-pass filter has a corner frequency approximately equal to the resonance linewidth of 2–3 Hz. This is true whether the applied magnetic field is changed via a step in the current supply output or whether the effective magnetic field is changed by an alteration of the applied light shifts. Because of the magnetometer's slow response, it is necessary to take into account the low-pass filter when comparing data wherein LS_y and LS_z are modulated at different frequencies. (Both would be unattenuated if $\omega_y, \omega_z \ll 2$ Hz, but this would require such low modulation frequencies as to be experimentally inconvenient and cause the magnetometer to suffer from a high $1/f$ noise floor.) To mitigate the differential low-pass filtering of the two light-shift modulations, we switch the high and low modulation frequencies between the two LS beams several times during each measurement, as depicted in Fig. C.1. For visual clarity, here we have chosen a data set which does not appear in the main text, wherein the two LS modulation frequencies were chosen to be 6 Hz and 10 Hz and the field angle θ was 11.25°. Figure C.1 also shows the predicted Y output of the lock-in amplifier (green) in response to the interlaced LS_y and LS_z frequencies. At would be expected for a magnetic field nearly aligned with the $\hat{z}$ axis, the Y output primarily follows the LS_z beam modulation, with small additional contribution due to LS_y. The low-pass-filter effect has also been taken into account when calculating the Y trace. This prediction can be compared to the recorded data (purple), which show clear qualitative and quantitative agreement.

Light Shifts

As thoroughly described in the literature [50,51,126], the AC Stark shift δE of a ground-state alkali atom can be decomposed as:

$$\delta E = (\delta E)_0 + \delta\mathcal{A}\,\mathbf{I}\cdot\mathbf{S} + \boldsymbol{\mu}\cdot\mathbf{B}_{\mathrm{LS}} + (\delta E)_t, \tag{C.1}$$

where the first two terms represent, respectively, the scalar shift of all ground-state sublevels and the modification of the ground-state hyperfine coupling coefficient $\mathcal{A}$ between the nuclear and electron spins $\mathbf{I}$ and $\mathbf{S}$. As these terms do not affect Zeeman coherences within a single hyperfine manifold, we shall ignore them in the present discussion. The third term in Eq. (C.1) represents the vector light shift, often described as a fictitious magnetic field $\mathbf{B}_{\mathrm{LS}}$ oriented along the propagation direction of a circularly polarized laser beam and coupling with the atomic spin $\boldsymbol{\mu}$. The tensor light shift $(\delta E)_t$ is caused by the quasiuniform electric field of the light producing second-order Stark shifts in the alkali sublevels, producing energy-level corrections akin to an added nonlinear Zeeman shift [52].

Here we briefly remind the reader of the effect of a circularly polarized near-resonant beam incident upon an alkali vapor. Although it is sometimes claimed that only the vector

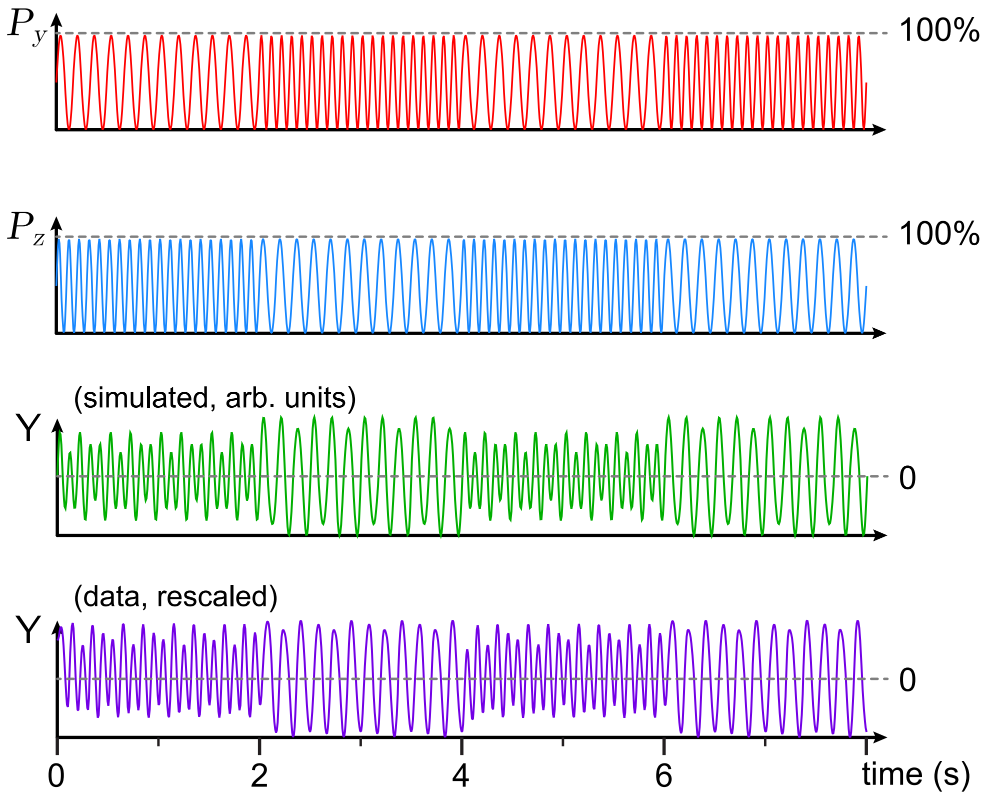

Figure C.1: The interlaced modulation scheme used to remove low-pass-filter effects from the vector field measurement. The powers P_y and P_z of the light-shift beams were modulated at 6 and 10 Hz, with the frequencies alternated at regular time intervals. The red and blue curves depict the calculated beam powers of the LS_y and LS_z beams. The green trace shows the Y output (arbitrary units) simulated for a field angle $\theta = 11.25°$. The purple trace below shows the actual Y output (rescaled) recorded in the experiment under these conditions.

light shift acts upon the alkali sublevels in this case, the effects of such a beam are distinct from those of an applied static magnetic field. We illustrate this with an atomic system with total angular momentum $F = 1$ in the lower state and $F' = 0$ in the upper state (Fig. C.2). The left diagram in Fig. C.2 shows the Zeeman effect of the $F = 1$ sublevels in a magnetic field applied along the quantization axis. The energy-level shift is proportional to the magnetic quantum number m_F. The right diagram in Fig. C.2 shows the effect of a σ_+ circularly polarized beam red-detuned from the optical resonance. According to the selection rules for optical transitions, only the $m_F = -1$ sublevel is shifted in the lower-state manifold, resulting in a different splitting pattern from that caused by the Zeeman effect. The overall light shift can be described as a combination of the vector and tensor terms in Eq. (C.1), even for the present case of circularly polarized light. More generally, one can understand the difference in the Zeeman and the AC Stark effect from the perspective of an

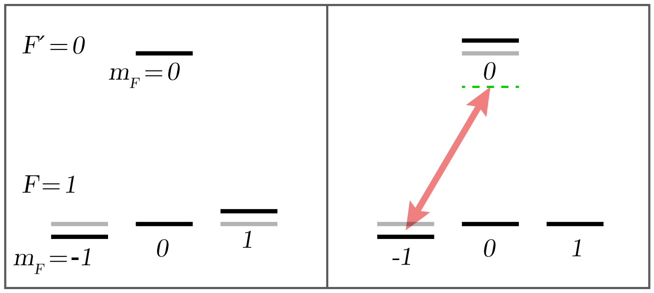

Figure C.2: Comparison between the Zeeman shift induced by a static magnetic field along the axis of quantization (left) and the AC Stark shift induced on the same system by a circularly polarized beam propagating along the same axis (right). The beam is red-detuned from the $F = 1 \rightarrow F' = 0$ transition. Energy levels are not to scale. Light grey bars represent unperturbed energy levels.

irreducible tensor basis. A detailed discussion may be found in Ref. [43].

Many prior studies of the vector light shift have downplayed the tensor contribution to the AC Stark shift [50, 51, 127], an approximation which can be justified when the excited-state hyperfine structure of the alkali atom (total angular momentum $F > 1/2$) is unresolved [1]. Other studies [128, 129] have restricted treatment of the AC Stark shift to highly symmetric conditions (e.g., wherein the pump beam, mean alkali spin projection, and magnetic field are all nearly collinear). Furthermore, nearly all discussions of the light shift ignore the light shift due to real transitions [73], a justifiable assumption when the optical pumping rate of the light-shift beam is vanishingly small. Our experiment is a distinct violation of many of the above simplifying assumptions, since our magnetometer is based upon synchronous transverse pumping of alkali atoms within an evacuated vapor cell and a near-resonant transverse light-shift beam. Nevertheless, the good agreement between the data shown in Fig. 2 and the curve predicted by Eq. (3) validates the interpretation of the vector light shift as a fictitious magnetic field in the present context. We observed no measurable splitting of the magnetic resonance due to the LS_y and LS_z beams, so any corrections due to the tensor light shift are small enough to be neglected here. We also estimate the light shift due to real transitions to be extremely small, since the observed broadening of the magnetic-resonance line by the light-shift beams LS_y and LS_z is less than 1 Hz. The light shift due to real transitions is proportional to this decoherence rate, but smaller by a factor of $|\omega_e - \omega_g| / \Gamma$, where ω_g and ω_e are the ground-state and excited-state spin-precession frequencies and Γ is the natural linewidth of the optical transition [130, 131]. Because this factor is $\lesssim 10^{-3}$ for the magnetic fields used in this experiment, we can ignore this effect in the present experiment.

Future measurements are planned to quantify the small corrections to the magnetometer response caused by the tensor light shift, the light shift due to real transitions, and the quadratic correction ζ given by Eq. (2).

[1]Experimentally, this is generally the case when buffer gases are included in the alkali-vapor cell, or when a broad-spectrum discharge lamp acts as the source of the light-shift beam.

Uncertainty in measurement of θ

In the course of our measurement, we observe the shift in observed magnetic field due to the LS_y light-shift beam and that due to the LS_z light-shift beam. Denote these two shifts as Δ_y and Δ_z, respectively. Once again taking only the lowest-order terms in the expansion of Eq. (1), we have:

$$f = \frac{\Delta_y}{\Delta_z} = \frac{1}{\beta} \tan\theta, \tag{C.2}$$

where $\beta \equiv P_z\alpha_z/P_y\alpha_y$ is the ratio of effective fields of the LS_z and LS_y beams, ostensibly a constant on the order of unity. The precision of our measurement of Δ_y and Δ_z is the same as the precision of our scalar magnetometer, which we define as δB_0. This scalar sensitivity has no dependence on the primary field magnitude B_0, since the synchronous transverse pumping scheme operates equivalently over a wide range of magnetic fields [2]. In the present analysis we also ignore any directional dependence of δB_0, which in general arises from the orientation of the pump and probe beams (not the LS_y and LS_z beams) with respect to the ambient field. For the sake of argument, one could reorient the pump and probe beams to optimize the scalar sensitivity of the magnetometer, or use a more advanced method of eliminating so-called "dead zones" in the magnetometer's sensitivity [132].

Here we wish to calculate the uncertainty in the measurement of the magnetic-field angle θ. Since $\theta = \arctan(\beta f)$, the uncertainty in θ, denoted σ_θ, is given by:

$$\sigma_\theta = \beta\sigma_f \frac{1}{1+\beta^2 f^2}, \tag{C.3}$$

where σ_f is the corresponding uncertainty in the measurement of f:

$$\begin{aligned} \sigma_f &= f\left[\frac{(\delta B_0)^2}{\Delta_y^2} + \frac{(\delta B_0)^2}{\Delta_z^2}\right]^{1/2} \\ &= \frac{\delta B_0}{\Delta_z^2}\sqrt{\Delta_y^2 + \Delta_z^2}. \end{aligned} \tag{C.4}$$

Combining this with Eq. (C.3), we arrive at the expression for the uncertainty in the field angle:

$$\sigma_\theta = \delta B_0 \frac{\beta}{\Delta_z^2 + \beta^2\Delta_y^2}\sqrt{\Delta_y^2 + \Delta_z^2}. \tag{C.5}$$

For the nominal case of $\beta = 1$, Eq. (C.5) reduces to a particularly simple form:

$$\sigma_\theta = \delta B_0 \sqrt{\frac{1}{\Delta_y^2 + \Delta_z^2}} = \frac{\delta B_0}{B_{\mathrm{LS}}}, \tag{C.6}$$

[2]This approximation begins to break down at geophysical fields (e. g. , 100 μT and above), where the nonlinear Zeeman splitting begins to change the structure of the magnetic resonance.

where B_{LS} is the magnitude of the magnetic field produced by each light-shift beam. In this case the uncertainty in the field angle depends neither on the magnitude B_0 of the ambient field nor on its angle θ with respect to the light-shift beams. Even if $\beta \neq 1$, this only introduces a directional dependence in the uncertainty σ_θ, which still remains independent of the field magnitude. This remains true for a three-dimensional vector measurement, and can be understood intuitively as a consequence of the fact that some linear combination of the light-shift fields will always add in parallel with the primary field.

For the experimental technique used to measure the data shown in Figs. 2 and 4 of the main text, the light-shift beams must shift the magnetic resonance only by a small amount, such that the lock-in Y output remains linearly proportional to the shift in Larmor frequency. This places a constraint on B_{LS}, which must be smaller than the magnetic-resonance linewidth (in field units). Assuming that the light-shift beams had a maximum effective field of 0.286 nT (equivalent to a 1 Hz shift in spin-precession frequency), a magnetometer with scalar sensitivity of 50 fT/$\sqrt{\mathrm{Hz}}$ would have an angular precision of $\sim$175 μrad/$\sqrt{\mathrm{Hz}}$.